Helmholtz-Zentrum Potsdam - Deutsches GeoForschungsZentrum
Sektion 2.5: Geodynamische Modellierung

Modelling Surface Evolution Coupled with Tectonics: A Case Study for the Pamir

Dissertation

zur Erlangung des akademischen Grades

doctor rerum naturalium
(Dr. rer. nat.)

in der Wissenschaftsdisziplin

Geophysik

eingereicht an der
Mathematisch-Naturwissenschaftlichen Fakultaet
der Universitaet Potsdam

vorgelegt von

Sarah Schröder

02. September 2015

Published online at the
Institutional Repository of the University of Potsdam:
URN urn:nbn:de:kobv:517-opus4-90385
http://nbn-resolving.de/urn:nbn:de:kobv:517-opus4-90385

$\pi\alpha\nu\tau\alpha\ \rho\epsilon\iota$

Heraklit von Ephesos

Abstract

This study presents the development of 1D and 2D Surface Evolution Codes (SECs) and their coupling to any lithospheric-scale (thermo-)mechanical code with a quadrilateral structured surface mesh.

Both SECs involve diffusion as approach for hillslope processes and the stream power law to reflect riverbed incision. The 1D SEC settles sediment that was produced by fluvial incision in the appropriate minimum, while the supply-limited 2D SEC DANSER uses a fast filling algorithm to model sedimantation. It is based on a cellular automaton. A slope-dependent factor in the sediment flux extends the diffusion equation to nonlinear diffusion. The discharge accumulation is achieved with the D8-algorithm and an improved drainage accumulation routine. Lateral incision enhances the incision's modelling. Following empirical laws, it incises channels of several cells width.

The coupling method enables different temporal and spatial resolutions of the SEC and the thermo-mechanical code. It transfers vertical as well as horizontal displacements to the surface model. A weighted smoothing of the 3D surface displacements is implemented. The smoothed displacement vectors transmit the deformation by bilinear interpolation to the surface model. These interpolation methods ensure mass conservation in both directions and prevent the two surfaces from drifting apart.

The presented applications refer to the evolution of the Pamir orogen. A calibration of DANSER's parameters with geomorphological data and a DEM as initial topography highlights the advantage of lateral incision. Preserving the channel width and reflecting incision peaks in narrow channels, this closes the huge gap between current orogen-scale incision models and observed topographies.

River capturing models in a system of fault-bounded block rotations reaffirm the importance of the lateral incision routine for capturing events with channel initiation. The models show a low probability of river capturings with large deflection angles. While the probability of river capturing is directly depending on the uplift rate, the erodibility inside of a dip-slip fault speeds up headward erosion along the fault: The model's capturing speed increases within a fault.

Coupling DANSER with the thermo-mechanical code SLIM 3D emphasizes the versatility of the SEC. While DANSER has minor influence on the lithospheric evolution of an indenter model, the brittle surface deformation is strongly affected by its sedimentation, widening a basin in between two forming orogens and also the southern part of the southern orogen to south, east and west.

Contents

Abbreviations

SEC	surface evolution code
SEM	surface evolution model
DEM	digital elevation model
SPL	stream power law
1D	one dimensional
2D	two dimensional
3D	three dimensional
SLIM	code for lithospheric scale modelling
TIPAGE	Tian Shan - Pamir Geodynamic Programme
a.s.l.	above sea level
w.l.o.g.	without loss of generality

Symbols

symbol	unit	explanation
i	1	node of 1D/2D numerical grid
x_i	m	1D horizontal coordinate of node i
$\underline{x_i}$	m	2D horizontal coordinates of cell i, $\underline{x_i} := (x_i, y_i)$
Δx	m	surface node spacing
h	m	altitude above sea level
h_i	m	altitude in node i
ϵ	m	elevation offset for filling algorithm
t	y	time
Δt	y	time step length
$\Delta_t h_i$	m	elevation change in node i
S	1	slope in water flow direction (tangent)
S_i	1	slope in water flow direction in node i
S_c	1	critical value for slope (nonlinear diffusion)

symbol	unit	explanation
A	m^2	drainage area
L	m	channel length from spring
L_i	m	channel length from spring to node i
P	m/y	precipitation rate
P_i	m/y	precipitation rate in node i
P_{max}	m/y	maximum of precipitation rate
Q	m^3/y	surface water discharge
Q_i	m^3/y	surface water discharge in node i
Q_{min}	m^2	water discharge threshold for incision
Q_s	m^3/y	sediment discharge
$\underline{q_s}$	m^3/my	sediment flux
κ_{hs}	1	hillslope diffusion coefficient (diffusivity)
κ_{rb}	1	river bed incision coefficient (stream power coefficient)
m	1	exponent of drainage area (SPL)
n	1	exponent of slope (SPL)
p	1	exponent of channel length (Hack's Law)
I_{min}	m/y	incision threshold
r_i^{lat}	$cells$	radius for lateral incision (spreading/incision radius)
Δh_i^{lat}	m	elevation difference for lateral incision (lateral incision height)
S^{lat}	1	slope difference for lateral incision (lateral incision slope)
Q_i^{lat}	m^3/y	water discharge around node i for lateral incision
c_{rad}	$y/m^3 \cdot cells$	incision radius coefficient
$c_{\Delta h}$	y/m^2	lateral incision height coefficient
e_{rad}	$y/m^3 \cdot cells$	incision radius exponent
$e_{\Delta h}$	y/m^2	lateral incision height exponent
w_c	m	channel width of a stream
U	m/y	rock uplift rate
n_{smooth}	1	window size for displacement smoothing
$\frac{\delta h}{\delta t}$	1	derivative of h with respect to t
$\#M$	1	cardinality (no. of elements) in the set M
$\lvert\underline{x}\rvert$	m	Euclidean norm, $\lvert\underline{x}\rvert = \lvert(x,y)\rvert = \sqrt{x^2+y^2}$
e_i	1	unit vector
∇h	1	gradient of h, $\nabla h = \frac{\delta h}{\delta x_1} \cdot e_1 + ... + \frac{\delta h}{\delta x_d} \cdot e_d$ (d: dimension of ∇)
$\nabla \cdot \underline{q}$	1	divergence of $\underline{q}$, $\nabla \cdot \underline{q} = \frac{\delta \underline{q}}{\delta x_1} + ... + \frac{\delta \underline{q}}{\delta x_d}$ (d: dimension of ∇)

Chapter 1

Introduction

Geological background

In 1912 Alfred Wegener proposed the theory of the continental drift. This initiated a discussion that 50 years later lead to the established model of plate tectonics: The lithosphere build a rigid crust on top of highly viscous mantle material. The fragments of the lithosphere are defined as tectonic plates, separated from each other by high frequency earthquake zones. Similar to ice-sheets on the sea, tectonic plates drift on the slowly convecting mantle material in different directions. Collision of tectonic plates cause deformation of lithospheric material. This material is partly forced to expand in vertical direction. It does not only lift up to an orogen at the earth's surface, but forms also a mountain root. The crustal material sinks into the more dense mantle material until the isostatic equilibrium is reached, where gravity equals the uplifting force.

An important mechanism in active orogens are surface processes. Surface processes include weathering and mass wasting. Weathering breaks down rocks, soils and minerals physically and chemically to sediments. Mass wasting is the movement of these sediments downslope by gravity. This set of processes is commonly referred to as erosion (Gilbert, 1877, p.93-94). Weathering as well as mass wasting are parts of both riverbed incision and hillslope processes. Weathering on hillslopes is driven by freezing water, rainsplash, change in temperature, organic content in the soil layer and chemical reactions. In the riverbed, physical weathering is mainly caused by saltating and abrasing sediments (Sklar and Dietrich, 2001): Water carried sediments induce shear stress at the riverbed, it gets incised. Riverbed incision is the main driving force of erosion. Due to incision, hillslope angles and therefore mass wasting get increased. While sediments on hillslopes are transported over short distances into a river, rivers serve for long-range transport down the channel to the base level (e. g. the sea).

In the eighties, geologists developed the idea that erosion may play an important role in orogen evolution (Adams, 1980; Suppe, 1981; Koons, 1989). Beaumont et al. (1992) and Willett (1999) were among the first who numerically studied the interplay between tectonics and surface processes. Surface processes decrease the loading on the lithosphere, by transporting sediments out of the system and thereby may lead to isostatic uplift and higher collision velocities. On the other hand, uplift increases the elevation difference between mountain tops and the river base level. This leads to steeper hillslopes and may also cause a change in local temperature and precipitation. As a consequence erosion increases. In short, an increasing uplift leads to higher erosion rates, while an increase in erosion might lead to higher uplift rates. However, up to now such a two-way coupling has not been observed in the field (Whipple, 2014; Wang et al., 2014).

For the reason of this interaction, a rearranging river network may indicate a change of tectonic uplift rates. Recent river capturing events are observations of these rearrangements (e. g. Cook et al., 2014). River capturing (also called stream piracy) is a phenomenon when a river is deviated from its old bed to the bed of a neighbouring river. Often, the capturing process begins at a tributary that captures the tributary of another river. The captured tributary reverses almost spontaneously its flow direction.

The Pamir

This PhD work is a part of the DFG TIen Shan - PAmir GEodynamic program (TIPAGE). One aim of this project is to study the evolution of the Pamir - Tien Shan orogen, including surface evolution.

Locals state that *Pamir* means "Roof of the World", since it is one of the worlds highest orogens. It lies between the Tien Shan mountains in the North and the Hindu Kush in the South. Peaks reach up to $7500\,m$, and 1% of the whole region is covered by glaciers. The Pamir orogen encloses one of the most powerful river systems on the planet. This network transports millions of tons of sediments out of the orogen and redistributes the lithosphere's loading in this way. Sec. 4.3 studies whether that redistribution may affect the upper mantle's evolution.

One of the most pronounced geomorphological features is the sudden turn of the Panj river from EW to SN in the south of Khorog (see Fig. 1.1). In the North of the turn, Belousov (1976) found early- to mid-pleistocene river terraces, that dip against today's river flow direction. He interprets the gradient as a result of tectonic uplift. However, the north-southward dipping could be effected by a recent change of the river flow direction. A plausible explanation for that change is a drop of the river base level, that lead to a spontaneous upstream river capturing

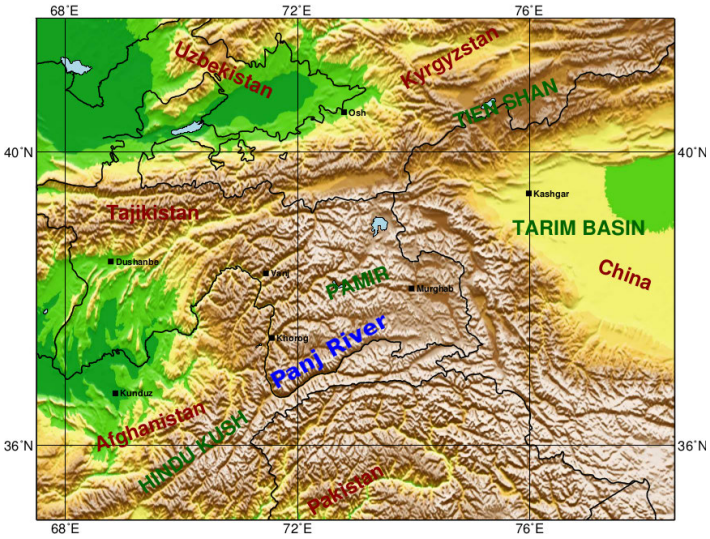

Figure 1.1: *Topographic map of the Pamir orogen*

event (Gloaguen et al., 2014; Fuchs et al., 2013). In Sec. 4.2, I try to validate or reject this theory.

Numerical studies

The understanding of the complex evolution of the earth's crust and mantle has been strongly boosted by numerical studies (e. g. Beaumont et al., 1994; Willett, 1999; Burov et al., 2006). Numerical modelling is also extensively used in geomorphology to explain and predict surface evolution on different scales (e. g. Chase, 1992; Kooi and Beaumont, 1996; Goren et al., 2014; Simpson and Schlunegger, 2003). The question whether an interaction between tectonics and surface processes is observable in the field motivates coupled numerical models. While largest scale whole-mantle convection models may ignore the negligible influence of surface processes, this is generally not true for lithospheric-scale (thermo-)mechanical models (Beaumont et al., 1992; Willett, 1999).

Since surface evolution models and lithospheric-scale models base on different temporal and spatial resolutions, a fully coupled code should include appropriate interpolation methods. This was firstly described by Collignon et al. (2014). Nevertheless, their code does not distinguish between the disparate processes in channels and on hillslopes. Thus, Collignon et al. recommend to not model geomorphological features with their code.

Up to now, most numerical river capturing models neglect the importance of non-fluvial water divides for capture events (Garcia-Castellanos, 2002). If a channel

network is defined, outside which no fluvial incision occurs, the channel network gets much more stable. One approach to destabilise river networks is made by the multiple flow direction algorithm (Freeman, 1991; Pelletier, 2004). Unfortunately, this algorithm works just in low slope regions. Goren et al. (2014) present a computationally expensive surface evolution code that couples grid-based and analytical solutions and is able to take drainage divides into account. A simple and therefore fast surface evolution code, which is able to model hillslope processes at drainage divides and river capturing events at orogenic scale is still missing.

Aim: A SEC for versatile applications

This study is dedicated to the development, implementation and application of numerical codes for surface processes. These codes are suited for coupling to 2D and 3D lithospheric-scale models with surface nodes arranged as a quadrilateral, structured mesh. The surface evolution codes should contain all needed smoothing and interpolation routines to transfer tectonic low resolution surface displacements to a high resolution surface, evolve it in multiple time steps, and hand the evolved topography back to the lithospheric-scale code.

The numerical models of surface processes are not meant to fully reflect the highly complicated interaction between riverbed incision and hillslope processes, but should satisfy known physical and empirical equations. Hillslope processes were modelled using linear and nonlinear diffusion. Incision satisfies the stream power law. Even though sedimentation may be neglected in a model in the inner of the Pamir orogen, a model of larger study area has to take deposition into account. In addition, the 3D surface evolution code should be able to simulate important geomorphological features as headward erosion and river capturing events.

Beside all these requirements, the models have to be kept as simple as possible in terms of the number of variables. This major problem (not just in numerical modelling) is today known as Boninis paradox named after Charles Bonini. It was already stated in 1937 by Paul Valéry: "Everything simple is false. Everything which is complex is unusable" (Notre destin et les lettres, 1937).

Up to now numerical studies have mainly been made for synthetic landscapes, either imposed (e. g. Tucker and Bras, 1998; Simpson and Schlunegger, 2003; Goren et al., 2014) or resulting from coupled large scale geodynamic models (Beaumont et al., 1992; Willett, 1999; Kooi and Beaumont, 1996). DeLong et al. (2007) suggest a calibration method for a SEC that includes threshold landsliding and bedrock incision. They vary the uplift rate, the incision efficiency, and the threshold slope in their models. The resulting steady state relief, mean elevation, drainage density and other characteristics are compared to the study region and the best fit

topography is chosen. Pelletier (2010) suggests a technique to calibrate his model to the Grand Canyon from field observations. However, none of these studies applied a calibrated surface evolution code to a digital elevation model.

I use a digital elevation model (Tachikawa et al., 2011) and geomorphological data, such as incision rates and sediment discharges in rivers, to adapt the 2D Surface Evolution Code (SEC) to the Pamir orogen. Is the new SEC able to reproduce in situ erosion rates? I calibrate the new SEC to the Pamir region and discuss challenges and limits for this calibration.

In chapter 2, I review prior modelling. This motivates the 1D and 2D SECs (chapter 3) and their application (chapter 4) to the Pamir orogen. Finally, summary and outlook are presented in chapter 5.

Chapter 2

State of the art

In this chapter, I review prior studies that influenced the development of my surface evolution codes (SECs) and further analysing tools. Sec. 2.1 summarizes the most important methods for lithospheric-scale modelling, especially the mesh types that are of importance for a coupling with a SEC. Prior SECs and the geomorphological background are described in Sec. 2.2. Sec. 2.3 presents the state of the art of the coupling techniques between lithospheric-scale mechanical codes and SECs. Finally, Sec. 2.3.2 gives an overview of the most important applications of coupled codes.

2.1 Methods for lithospheric-scale modelling

The earth's lithosphere behaves as viscous, plastic or elastic material. The response of the earth's lithosphere to applied stresses is determined by its rheology. This behaviour is a combination of viscous, plastic and elastic deformation. Which mechanism is dominant depends on the temperature, the pressure, the strain rate, the time scale and the chemical composition of the material. Since all these properties influence the evolution of the lithosphere, they have to be taken into account in a numerical code for modelling lithospheric deformation.

A common approach in modelling the mechanical evolution of the lithosphere is to describe its motion with the Stokes equations. These equations state the conservation of mass and momentum in the model, and relate forces to stresses within the material. To derive the velocities, additional constitutive laws are required that link stress and strain. These laws describe under which conditions occurs viscous, plastic or elastic deformation (e. g. Popov and Sobolev, 2008).

As the temperature plays a key role in these constitutive laws, many models also

include an equation that describes the thermal evolution of the lithosphere (e. g. Braun et al., 2008; Popov and Sobolev, 2008; Godard et al., 2006). The temperature field is advected with the velocities derived from the Stokes equations, and evolves due to several other mechanisms such as diffusion, radiogenic heat production, shear heating and latent heat. This means that thermal and mechanical evolution are coupled, and have to be solved as part of a scheme that allows the exchange of information between them.

The following paragraphs explain different mesh types and other important features of lithospheric-scale models. The understanding is important for the coupling with a surface evolution code.

Currently developed (thermo-)mechanical models utilize an Eulerian finite difference approach (Gerya and Yuen, 2003; Popov and Kaus, 2013), an Eulerian finite element method (Moresi et al., 2003; Braun et al., 2008), a fully Lagrangian finite element approach (Godard et al., 2006), or an arbitrary Lagrangian-Eulerian formulation (Fullsack, 1995; Poliakov et al., 1993; Kurfess and Heidbach, 2009; Popov and Sobolev, 2008; Burov et al., 2006) with *remeshing* after multiple time steps. This remeshing substitutes the deformed mesh with a less deformed one and interpolates the associated material properties to the new mesh.

Most (thermo-)mechanical codes base on a structured mesh, while only a few a based on an unstructured one (Dabrowski et al., 2008). In meshless modelling techniques (Hansen, 2003), discrete particles are mutually attached via shape functions. In a structured mesh, every node has a similar number of neighbours and whether two nodes are neighbours or not is determined by the mesh positions. In an unstructured mesh, the number of neighbours may be different for different nodes. Hence, an additional connectivity list stores the connections among them. While an unstructured mesh is more flexible, a structured mesh has the advantage of faster computation and consumes less storage. Often, an additional Lagrangian particle cloud (*markers*) tracks the material properties (e. g. Braun et al., 2008; Beaumont et al., 1994; Popov and Sobolev, 2008) for sake of a finer resolution.

Braun et al. (2008) show a model with an octree division of space, Moresi et al. (2003) and Poliakov et al. (1993) choose a quadrilateral mesh, Babeyko and Sobolev (2008) and Godard et al. (2006) choose a triangular one. Independent of the discretization, *adaptive remeshing* allows to modify the mesh during the model evolution to increase the resolution in areas where it is needed, e. g. faults (Braun et al., 2008).

In order to model the surface movements in (thermo-)mechanical models two approaches are common: A sticky air layer with low viscosity and zero-density (Schmeling et al., 2008) or a freely evolving surface (Popov and Sobolev, 2008; Beaumont et al., 1994). Both approaches for a free surface will suffer from numer-

ical instabilities, if the time step (for the freely evolving surface) or the resolution (for the sticky air layer) is not significantly reduced. To avoid time steps of a few thousand years, most free surface models include a smoothing routine (Popov and Sobolev, 2008; Huismans, 2014; Braun et al., 2008) that might be interpreted as a simple approach for erosion (Koons, 1989). Recently, Kaus et al. (2010) developed a free surface stabilization approach that faces this challenge in another way. They include a time dependency in the momentum equations. The appearing surface traction terms correct the change of the forces by advection or distortion of every element. Most (thermo-)mechanical codes with free surface hold the first-mentioned smoothing routine. This has to be taken into account for the transfer of lithospheric surface movements to a SEC (compare to Sec. 2.3).

2.2 Surface evolution

The main driving force for erosion in mountainous regions is fluvial incision. Incising rivers transport sediments out of the system and dissect the orogen. This triggers hillslope processes to supply sediments of the whole orogen to the river network. Accordingly, most of the Surface Evolution Codes (SECs) include both hillslope processes and riverbed incision.

The time scale of the desired models ranges from thousands to tens of millions of years. Since this time scale is much longer than the frequency of mass wasting events such as landslides or flooding so that the variability is averaged out, I concentrate on deterministic models and neglect stochastic approaches (e. g. Tucker and Bras, 2000).

In the following, a SEC that evolves on a topographic line is termed *1D* SEC and a SEC evolving as an earth-like topography is defined as *2D*. While Sec. 2.2.1 specifies important physical and empirical equations, the numerical details of available SECs are outlined in Sec. 2.2.2.

2.2.1 Physical, empirical and mathematical models

Hillslope processes

Mass wasting events on hillslopes are influenced by many factors. Hillslope material, moisture of the material, steepness of the slopes, climate, vegetation and fauna all effect transport processes. They may be triggered by earthquakes, storms, snowmelt or freezing water. The quantitative effect of all mentioned parameters is too complex to put them in a mathematical model. Here, I briefly introduce a well working first order approach, the diffusion equation.

Assuming mass conservation for hillslope processes establishes the evident *continuity equation*

$$\frac{\delta h}{\delta t} = -\nabla \cdot \underline{q_s} \tag{2.1}$$

with the altitude above sea level h, time t and sediment flux $\underline{q_s}$.

Assuming a linear approach for sediment flux

$$\underline{q_s} = -\kappa_{hs} \cdot \nabla h, \tag{2.2}$$

gives the known *diffusion equation* (Kirkby, 1971)

$$\frac{\delta h}{\delta t} = \kappa_{hs} \cdot \nabla^2 h \tag{2.3}$$

with the hillslope diffusivity κ_{hs}.

The linear diffusion equation reflects hilltop processes (e. g. creeping) on low slopes sufficiently (Tucker and Bras, 1998; Hurst et al., 2012). Nevertheless, it is an common understanding that sediment flux is highly nonlinear on steep slopes (Howard, 1994; Roering et al., 1999; Larsen and Montgomery, 2012). Multiple resembling equations are suggested.

Roering et al. (1999) propose a transport law that approximates linear sediment flux at low gradients and rapidly increasing flux as the gradient approaches a critical value S_c. They demonstrate, on the example of the Oregon Coast Range, that the *nonlinear diffusion* equation better describes the sediment flux:

$$\underline{q_s} = \kappa_{hs} \cdot \nabla h \cdot \left[1 - \left(\frac{|\nabla h|}{S_c}\right)^2\right]^{-1} \quad for \;\; \nabla h < S_c. \tag{2.4}$$

The graphs in Fig. 2.1 compare linear and nonlinear sediment flux and illustrate how the nonlinear diffusion handles slopes close to the critical value. If $|\nabla h|$ is small compared to the critical value S_c, the weight will be slightly above 1 and the sediment flux $\underline{q_s}$ will be close to the linear flux. If the gradient approaches S_c, the weight and the sediment flux $\underline{q_s}$ will go towards infinity. Note that S_c is not the critical angle of repose known from slope stability, S_c has to be chosen larger.

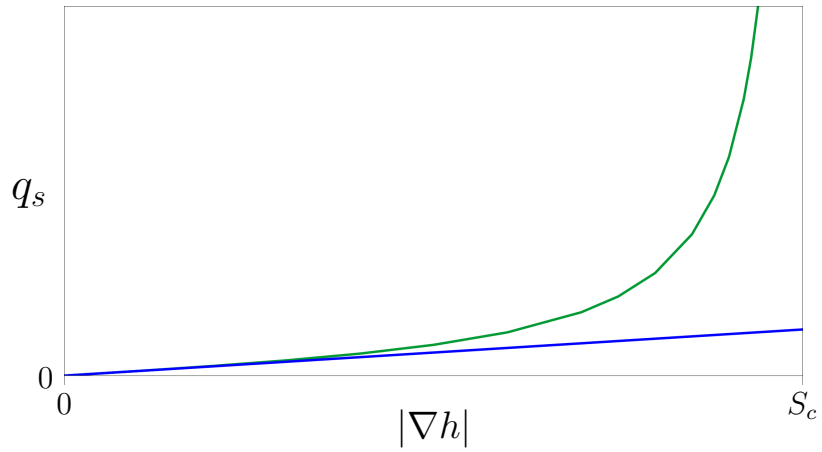

Figure 2.1: *Linear* (3.21) *(blue) versus nonlinear* (2.4) *(green) diffusive sediment fluxes* q_s *between two nodes against the slope* $|\nabla h|$ *between them.*

Fluvial processes

Streams may incise directly into the bedrock, wash a covering sediment layer from the riverbed or deposit fluvial sediments on the ground. If the sediment supply is smaller than the river transport capacity, this phenomenon is referred to as *supply-limited*. If the amount of supplied sediment is more than the stream is able to transport, the stream is *transport-limited*. Thus, the stream power is of major importance for fluvial processes.

In 1966, Bagnold suggested that the stream power depends on water discharge and its velocity. These heuristic studies lead to the *Stream Power Law (SPL)* (Howard and Kerby, 1983), which physically expresses that the incision rate is proportional to the shear stress of the water discharge on the riverbed. More recent studies lead to the knowledge that the incision rate is also dependent from the river sediment discharge (Sklar and Dietrich, 2001). Based on a lack of detailed knowledge concerning the highly complex processes, the stream power law is still the commonly used model for riverbed incision (Lague, 2014).

With the incision constant κ_{rb}, water discharge Q, slope in water flow direction S and the scaling exponents m and n the *stream power law* is noted as

$$\frac{\delta h}{\delta t} = \kappa_{rb} \cdot Q^m S^n. \tag{2.5}$$

The upstream drainage area A weighted by the effective precipitation rate P will approximate the water discharge Q, if subsurface water flow and evaporation is negligible:

$$Q = \int_A P. \tag{2.6}$$

One approach for the drainage area is *Hack's Law* (Hack, 1957), that suggests a dependence of drainage area from channel length L:

$$L = c_{Hack} \cdot A^h \tag{2.7}$$

For a 1D surface evolution code, Willett (2010) suggests nearly rectangular river basins with the width of a partial drainage basin y_d:

$$A = L \cdot y_d. \tag{2.8}$$

Combined with the inverse of Hack's Law, he obtains, with a constant $\kappa_a := \frac{1}{{c_{Hack}}^p}$ and the inverse of Hack's exponent $p := \frac{1}{h}$,

$$y_d = \kappa_a \cdot L^{p-1}. \tag{2.9}$$

Due to a lack of data orthogonal to the model, he has to assume a precipitation rate that is constant in sections orthogonal to the channel. With stated assumptions and fixed channel length L, Eq. 2.6 leads to

$$Q = y_d \int_0^L P(x)dx = k_a \cdot L^{p-1} \int_0^L P(x)dx. \tag{2.10}$$

Stream profile analysis Many studies about the stream power law exponents in particular regions have been made (Roberts and White, 2010; DeLong et al., 2007; Pelletier, 2010; Whipple and Tucker, 1999; Seidl and Dietrich, 1992; Stock and Montgomery, 1999). Stream profile analysis (Hack, 1957) is one method to derive the exponents. It is based on the assumption that the river reached its steady state (sometimes mentioned as erosional equilibrium, e. g. Yang et al., 2015). In the following, I explain the theory.

Assuming a channel reached erosional equilibrium, the tectonic uplift U compensates the fluvial incision. With the stream power law (2.5), the drainage area A and the steepest descent slope $S := \frac{\delta h}{\delta x}$ follows:

$$U = \kappa_{rb} \cdot A^m S^n. \tag{2.11}$$

Adapted this gives

$$S = \left(\frac{U}{\kappa_{rb}}\right)^{\frac{1}{n}} \cdot A^{-\frac{m}{n}}. \tag{2.12}$$

Substituting the steepness index $k_s := \left(\frac{U}{\kappa_{rb}}\right)^{\frac{1}{n}}$ and the concavity index $\theta := \frac{m}{n}$, according to Hack (1957) the equation can be written as

$$S = k_s A^{-\theta} \tag{2.13}$$

or

$$log(S) = log(k_s) - \theta \cdot log(A). \tag{2.14}$$

For constant U, κ_{rb} and θ, this equation gives a linear dependency of logarithmic slope on logarithmic drainage area. A log-log plot of slope against drainage area along a channel reveals the ratio θ of the required exponents.

If the uplift rate varies spatially:

$$U(L) = U_0 L^{\alpha} \tag{2.15}$$

and Hack's Law (2.7) is valid, a steady state longitudinal stream profile will fulfil (2.13) with

$$\tilde{k_s} := \left(\frac{U_0}{\kappa_{rb}}\right)^{\frac{1}{n}} {c_{Hack}}^{-\frac{\alpha}{hn}} \tag{2.16}$$

and

$$\tilde{\theta} := \frac{m}{n} - \frac{\alpha}{hn} \tag{2.17}$$

(Kirby and Whipple, 2001). Here, U_0 is the rock-uplift rate at the channel head, L is the channel length starting from the channel head, α is a constant, c_{Hack} is the constant of Hack's Law (2.7) and h is Hack's exponent.

Please note that $\tilde{k_s}$ and $\tilde{\theta}$ are constants for constant κ_{rb}. Hence, increasing uplift rate of the shape (2.15) leads to a linear log-log plot as well. The gradient of this plot is $\tilde{\theta}$.

Stream power exponents Seidl and Dietrich (1992) measure $\theta = 1$ in the coastal basin of Oregon. Willgoose (1989) chooses $\theta = 0.86$ for alluvial channels. Other studies suggest θ within the interval $[0.3, 0.6]$ (DeLong et al., 2007; Whipple and Tucker, 1999; Snyder et al., 2000). Whipple and Tucker (1999) suppose that values outside of the interval $[0.35, 0.6]$ reflect disequilibrium conditions, systematic downstream variations in rock uplift rate or erodibility or regression of data that cross the bedrock alluvial transition. Finally, Kirby and Whipple (2001) give an analytical solution for locally variable uplift rates and conclude that the concavity index θ is small or negative where rock-uplift rate is increasing downstream and high where rivers flow towards regions of decreasing uplift rate.

Stock and Montgomery's (1999) measurements for Australian rivers of $m = 0.3$ to 0.5 and $n = 1$ agree with these observations. Howard and Kerby (1983) observe $m = 0.45$ and $n = 0.7$ in badland channels. This gives $\theta = 0.64$, which is also close to the stated interval.

Channel width and depth The width w and depth d of a natural channel depend on its water discharge. Leopold and Maddock (1953) first stated the empirical equations

$$w = a \cdot Q^b$$

and

$$d = c \cdot Q^f$$

with constants a and c. They evaluate average exponents $b = 0.5$ and $f = 0.4$. Finnegan et al. (2005) found other exponents and a dependency from roughness. Up to now, the parameters governing the channel width are still discussed.

2.2.2 Numerical approaches

When first modellers (Koons, 1989; Willgoose, 1989) developed numerical mountain range-scale, long term evolution surface evolution codes (SECs), it became clear that diffusion alone (2.3) is not able to simulate the erosion processes satisfyingly at finer resolutions (Koons, 1989). Since then, most SECs simulate both fluvial and hillslope processes (Willgoose et al., 1991; Chase, 1992; Howard, 1994). These processes are usually coupled, using the same time step size and the same spatial resolution.

The analytical equations may be solved by finite differences on a 1D regular grid (e. g. Willett, 2010) or on a 2D regular square grid, the so-called *cellular automaton* (Coulthard and Van De Wiel, 2006; Beaumont et al., 1992; Chase, 1992; Howard, 1994; Willgoose et al., 1991). Few SECs are irregularly, triangulary discretised, because this is much more time consuming (Simpson and Schlunegger, 2003; Braun and Sambridge, 1997; Goren et al., 2014). One advantage of an irregular discretization is explained in Sec. 2.3.

The following sections describe how scholars implemented hillslope and fluvial processes. A channel initiation function gives the possibility to decide in every cell between both processes. In order to compute fluvial processes, the water discharge has to be accumulated. Hence, a water flow direction in every cell is obligatory. A direction cannot be evaluated, if unfilled depressions exist.

Hillslope processes

Sediment transport on hillslopes is mostly modelled as slope-dependent *linear diffusion* (2.3) (Beaumont et al., 1992; Kooi and Beaumont, 1996; Braun and Sambridge, 1997). In addition to that, Densmore et al. (1998) explicitly model the sediment production proportional to soil thickness.

Slope-dependent *threshold landsliding* was implemented as a statistic model (Pratson and Coakley, 1996; Densmore et al., 1998). Tucker and Bras (1998) state the model results to be similar to *nonlinear diffusion* (2.4). An analytical approach for nonlinear diffusion is implemented by Howard (1994) and Roering et al. (2001).

For all these models, it is assumed that runoff production is uniform across the basin. This is reasonable for arid catchments (Tucker and Bras, 1998). For humid catchments, Montgomery and Dietrich (1994) take the soil saturation into account.

In comparison to the other approaches, linear diffusion, as approach for gathered hillslope transport, has the advantage of fast computation. For models with steep slopes nonlinear diffusion provides the most efficient computation method. Models that take soil saturation into account can be neglected for the sudy region.

Glacial processes

The most popular zeroth order shallow ice approximation is not valid for glaciers in high relief areas (Egholm et al., 2011) as the Pamir orogen is. More physical glacial erosion approximations are 3D and much more complex than approximations for fluvial incision (e. g. Pedersen et al., 2014; Egholm et al., 2011). All glacial erosion models require a temperature in every surface cell for every time step.

A fluvial incision model has the advantage of less parameters and therefore less geomorphological data to validate the model.

Fluvial processes

Most SECs simulate riverbed incision with the aid of the empirical *stream power law* (2.5). It has been implemented in a supply-limited way (Howard and Kerby, 1983; Whipple and Tucker, 1999) and in a combination with transport-limitations (Davy and Lague, 2009). Beaumont et al. (1992), Braun and Sambridge (1997) and Garcia-Castellanos (2002) develop pure transport-limited models that assume a sediment carrying capacity proportional to channel slope and water discharge. Modern transport-limited models need time consuming computations to evaluate and store sediment layers (e. g. Tucker, 2010). Fully supply-limited models have the advantage of faster computation and are sufficient for regions with negligible sedimentation in chosen time steps.

Willett (2010) reduces the 2D fluvial processes to one dimension in order to couple it to a 2D tectonic code. He combines Eq. 2.10 with the stream power law to an analytical solution for the trunk stream profile and implicitly implements it. In addition, he establishes an equation for the *interfluvial ridge profile*, which is the total relief of a tributary. Assuming an erosion rate proportional to the local relief,

Willett is able to compute the interfluvial ridge elevation. He uses the average of the interfluvial ridge elevation and the trunk stream elevation as effective elevation in his 1D model. A simple version of this algorithm was implemented by Fuller et al. (2006).

Channel initiation function

The physical processes in rivers are different from those acting on hillslopes. However, some modellers do not distinguish between channels and hillslopes. E. g. Simpson and Schlunegger (2003) analytically couple diffusive flux and fluvial transport and apply this equation in all nodes. It has to be emphasized that this model contradicts observations.

A model that applies incision just in well defined channel cells is closer to observations. Accordingly, a SEC needs to identify channel heads. Montgomery and Foufoula-Georgiou (1993) conclude from Digital Elevation Models (DEMs) that both constant and slope-dependent catchment area for channel initiation agree with geomorphological data.

O'Callaghan and Mark (1984) define a cell as part of a channel if the drainage accumulation exceeds a certain threshold. Their model applies the stream power equation in cells that are defined as channel and hillslope processes in cells that are not defined as channel. The threshold is usually chosen $1 km^2$ (Braun and Sambridge, 1997). Willgoose et al. (1991) propose a channel initiation function that depends on discharge and slope. Davy and Lague (2009) as well as Tucker and Bras (1998) simplify their approach. They suggest an incision threshold I_{min}, below which no incision is supposed to occur. Contradictorily, they choose $I_{min} = 0$, due to poorly constrained parameters. Since the channel initiation seems to be much more complex than all developed numerical methods (Tucker, 2010), the approach of O'Callaghan and Mark (1984) is still implemented.

However, a channel initiation function limits the modelling of river capturing events (shown in Sec. 4.2.2). Headward erosion in interaction with a channel initiation function can only be modelled with grids of highest resolution (resolving finer than approx. $10\,m$, Jean Braun, personal communication, May 18, 2015). Garcia-Castellanos (2002) neglects channel initiation in his river capturing model. His approach assumes channels in all model cells and misses the influence of hillslopes, which form the last barrier before observed river capturing events.

Goren et al. (2014) model river capturing, taking into account hillslope processes. The presented code DAC (Divide And Capture) couples a 3D grid-based stream power model with an analytical model of the profile through every water divide. At all node connections without fluvial channel the location of the water divide,

the hillslope profiles, the fluvial profiles, and the junctions from hillslope to fluvial profiles are analytically determined. Nevertheless, a simple (and therefore fast) algorithm that enables river capturing events and that can be attached to one of the commonly used surface evolution models is still missing.

Drainage accumulation

The incision routine needs the water discharge and the topographic slope as input parameter for every grid cell. For stability reasons, the slope is usually computed with the aid of forward differences (Willett, 2010; Beaumont et al., 1992, see Sec. 3.1.3 for more details). The discharge gets approximated by the drainage area (Martz and Garbrecht, 1992; O'Callaghan and Mark, 1984), which can be weighted by a locally variable precipitation rate (Chase, 1992; Beaumont et al., 1992; Willett, 1999; Lague et al., 2005).

Currently used algorithms for 2D drainage accumulation need multiple iterations through most cells. These algorithms follow the flow direction either from each cell, incrementing every passed cell by one (Martz and Garbrecht, 1992), or from each spring, adding the discharge of the cell to the downstream cell (O'Callaghan and Mark, 1984).

In 1D SECs, one has to make an assumption for the second dimension of the water discharge. Thus, Fuller et al. (2006) and Willett (2010) develop the mentioned approach of rectangular river basins and Eq. 2.10.

Flow directions

Water discharge computations require flow directions in all cells. In 1D codes, the flow direction is the downhill direction (Willett, 2010). In most 2D codes, the flow direction is computed with the aid of the fast D8 algorithm (O'Callaghan and Mark, 1984; Martz and de Jong, 1988), the D-infinity algorithm (Tarboton, 1997) or the multiple flow direction (MFD) algorithm (Freeman, 1991).

The fast D8 algorithm assigns to each cell a flow direction to the steepest descent neighbouring cell. The D-infinity and MFD algorithms avoid the restriction in possible flow directions. The MFD method disperses the discharge over all downslope neighbouring cells and is inefficient in data storage (Tarboton, 1997). An advantage of the MFD method is an unstable drainage network in nearly flat regions. This allows to model e. g. fans (Pelletier, 2004). The D-infinity method spreads the discharge over just two adjacent cells. This is meant to be closer to physics. Furthermore, the algorithm is less storage consuming than the MFD algorithm is.

However, the MFD and the D-infinity algorithms manage to model fans in low slope regions, but keep the water discharge on steep slopes in channels of one cell width. None of the mentioned algorithms is able to simulate wide channels on steep slopes (e. g. Daan River in Taiwan, Cook et al., 2014) in high resolution.

Depressions, filling and sedimentation

None of the named flow direction algorithms is able to define a direction for a local depression. This fact presents one of the computational most expensive challenges. For that reason, some SECs do not consider forming depressions (Chase, 1992; Beaumont et al., 1992; Pelletier, 2004). Especially in 1D, one can assume the water discharge to leave the model at such a depression (Willett, 2010).

In 2D SECs, routines that immediately fill depressions up to the outflow are more common. Most algorithms identify all depressions, define the lowest elevation outlet of the corresponding drainage area, and fill them one by one (Martz and de Jong, 1988; Jenson and Domingue, 1988; Martz and Garbrecht, 1992). Planchon and Darboux (2001) develop a faster filling algorithm, which handles the complete topography. Starting from an unlimited high topography their algorithm decreases cell by cell down to the lowest neighbour elevation plus an infinitesimally small offset, but not lower than the elevation of the original topography.

Plenty of more physical, but also more time consuming 2D solutions have been applied: O'Callaghan and Mark (1984) implement an assignment of flow directions to depressions that lead through it, to the lowest elevation outlet. Algorithms that settle the sediment in the lowest cell of a depression have been developed (Howard, 1994; Lin et al., 2008). This results in a patchy filling of lakes and basins which takes multiple time steps. Garcia-Castellanos (2002) presents a model that deposits the transported sediment in all directions from the river mouth. The deposition rate decreases exponentially with the distance from it. This avoids a patchy result, but ends up in a slow filling as well.

If the amount of eroded material in a model exceeds the amount of the material that is needed to fill all depressions, a total filling within one time step will be a convenient method to handle depressions. A benefit compared to the described sedimentation routines is the formation of a plane instead of unnatural sediment hills.

2.2.3 Model calibration

In 1998, van der Beek and Braun attempted to constrain the Surface Evolution Model's (SEM) parameters, comparing the model predictions with observations

from the south-eastern Australian highlands. Since then, few studies have been made about the calibration of SEMs to geomorphological data.

DeLong et al. (2007) study the influence of tectonic uplift, incision parameter and landslide-threshold slope on the development of synthetic topographies. They compare the modelled steady state topographies to DEMs, but avoid to run the code on Digital Elevation Models.

Pelletier (2007) adapts his model to the southern Sierra Nevada, California. He reduces the high relief regions of a DEM by a factor of five to construct the initial topography and uses cosmogenic data for upland erosion and river incision rates to limit the range of parameters of a stream power model on one hand and a sediment-flux-driven model on the other hand. Finally, he compares both models. He is not able to decide for one model on the base of the two different results. As he assumes sediment abrasion to be the dominant erosion mechanism in granitic landscapes and κ_{rb} to be dependent on uplift rate, he chooses the sediment-flux-driven model. In later research, Pelletier (2010) calibrates his model to the Grand Canyon. In addition to statistical data from a DEM, he uses geomorphological data, such as peak discharge, channel width, incision rates, erodibilities, river profiles and headcutting.

However, to my knowledge there are no publications of a SEM with a DEM as the initial topography.

2.3 Coupled modelling

Since the 1980's, numerical modelling serves for studies about the orogen evolution (e.g Koons, 1989; Stephenson and Lambeck, 1985; Sinclair et al., 1991; Beaumont et al., 1992). Beyond that, the influence of surface processes is widely discussed (Whipple, 2014; Begin, 1988; Molnar and England, 1990). While the influence of surface processes can be neglected in pure mantle convection models, this is generally not true for models on lithospheric scale (Beaumont et al., 1992).

2.3.1 Techniques

In order to study the influence of surface processes on orogen evolution, a two-way coupling between surface evolution models and lithospheric-scale models with free surface is of major interest. First coupling approaches have been made either as thin-sheet approximation (Braun and Shaw, 2001) or as a cross section in the main deformation direction. While Willett (1999) implements a 1D stream power law on the surface of a 2D thermo-mechanical code, Beaumont et al. (1992) couple

the strike average of a 2D SEC to a 2D mechanical code. Fuller et al. (2006) and Willett (2010) reduce the surface processes to one dimension (2.10) and couple the resulting approach with 2D (thermo-)mechanical models. Few models couple 2D surface evolution with 3D (thermo-)mechanical evolution (Garcia-Castellanos, 2002; Kurfess and Heidbach, 2009).

A conventional time step for lithospheric-scale (thermo-)mechanical models is within the order of tens of thousands of years (Beaumont et al., 1992; Kurfess and Heidbach, 2009; Popov and Sobolev, 2008). To guarantee a stable surface evolution that includes fluvial processes, usually a time step of hundreds of years (Beaumont et al., 1992; Braun and Sambridge, 1997; Kurfess and Heidbach, 2009) is chosen. This leads to the idea to split the (thermo-)mechanical time steps into smaller surface evolution steps (Beaumont et al., 1992; Garcia-Castellanos, 2002).

Aside from that, the resolution of (thermo-)mechanical models is commonly chosen in km-scale (Popov and Sobolev, 2008; Kurfess and Heidbach, 2009; Godard et al., 2006), while the resolution of SEMs varies from $30\,m$ (DeLong et al., 2007) to $250\,m$ (Pelletier, 2004) up to $2000\,m$ (Beaumont et al., 1992). Thus, an interpolation between different temporal and spatial resolutions has to be implemented in any modern coupled code.

An advanced coupling method between surface and lithospheric evolution should not only transfer vertical uplift but also horizontal movements to the SEC. Thus, the (thermo-)mechanical code needs to hand the 3D surface displacements over to the SEC. A smoothing of the (thermo-)mechanical model's free surface (described in Sec. 2.1) does not influence the surface displacements. Consequently, another way to stabilize (thermo-)mechanical codes has to be implemented.

Kurfess and Heidbach (2009) neglect the need for different resolutions. They choose an irregular grid-based SEC (CASCADE) in order to make it possible to use the same resolution as the thermo-mechanical code ABAQUS. Garcia-Castellanos (2002) solves the challenge of different resolutions in an inconvenient way. His mechanically moving blocks must advance an integer number of surface nodes in every time step.

Recently, a full coupling of models with different spatial and temporal resolution has been implemented by Collignon et al. (2014) and Thieulot et al. (2014). Nevertheless, Thieulot et al. neglect isostasy in their crustal model and may therefore miss isostatic uplift in response to erosion processes. Collignon et al.'s SEC is not able to simulate geomorphic features such as knickpoint migration or river capturing (Collignon et al., 2014). Since these features are important signs for a reorganization of river networks and thus for tectonic uplift, a suitable coupled code for a high resolution surface is still missing.

2.3.2 Applications

Few studies with fully coupled (thermo-)mechanical and surface evolution codes have been published. Coupled applications concern folding patterns (Collignon et al., 2014), thrust faults (Braun and Yamato, 2010), basins (Garcia-Castellanos, 2002), subduction zones (Beaumont et al., 1992; Willett, 1999) and intracontinental collision (Burov and Toussaint, 2007).

Beaumont et al. (1992) and Willett (1999) study the influence of climate on orogen evolution that is caused by subduction. Their climate models hold a predominant wind direction that increases the erosion rate on one side of the drainage divide. The model of Beaumont et al. is made to reflect the evolution of the New Zealand Alps. They conclude that the structural and metamorphic style of this orogen is controlled by fluvial erosion. Willett states the same fact for subduction forearcs in general.

It is still discussed if it will be possible to observe signs of a tectonic feedback as a result of erosion processes (e. g. Whipple, 2014; Wang et al., 2014). Even though folding patterns might be slightly influenced by surface processes (Collignon et al., 2014), a two-way coupling is predicted by numerical studies:

Braun and Yamato (2010) show that effective surface evolution allows thrust faults to get planar instead of kinked and Garcia-Castellanos' (2002) models demonstrate how strong fluvial transport influences the vertical movements in foreland basins. Finally, Burov and Toussaint (2007) study the evolution of intercontinental collision zones, such as the India-Asia collision. They show that the total amount of subduction may largely vary as a function of the erosion rate. Very strong and very slow erosion enhance the possibility of plate coupling and promote whole scale thickening or buckling. The maximum amount of subduction is achieved when the tectonic uplift rate is balanced by the denudation rate.

These studies indicate that surface processes control the tectonic evolution of the mantle. Whether this is valid for intercontinental collision has been studied in 2.5 dimensions (Burov and Toussaint, 2007). However, the tectonic movement in the Pamir region is highly three dimensional (Sippl et al., 2013). This implies a need of a fully coupled 3D model of the India-Asia collision zone, including the Pamir region - which is the subject of the next chapter.

Chapter 3

Numerical modelling techniques

Physical and mathematical models try to simplify observed phenomena. Numerical codes translate the governing equations and link them together. For a given problem, it is left to every modeller to find a balance between simple and therefore fast algorithms on the one hand and highly complicated algorithms that try to reflect observations in more detail on the other hand.

The aim of the TIPAGE project is to study how the India-Asia collision effected the formation of the Pamir orogen. Within this project, the collision is simulated with the thermo-mechanical C++ codes SLIM 2D and SLIM 3D (Popov and Sobolev, 2008). Since erosion processes in the Pamir may have a remarkable influence on the tectonic processes, coupling of a Surface Evolution Code (SEC) to SLIM is of major importance. I took the opportunity to develop new C++ surface evolution codes, especially designed for coupling and for versatile applications in the Pamir. The time range for the SECs should be in the range of thousands up to tens of millions of years.

Beside the coupling, the 2D SEC can be applied to Digital Elevation Models (DEM). For this purpose, it holds special features, including a new method for lateral incision in rivers (Sec. 3.2.4) that provides a much more versatile alternative to the multiple flow direction algorithm (Freeman, 1991, see Sec. 4.1.4 and 4.2.2 for more details). Additionally, the totally supply-limited model without any sedimentation in the riverbed (not even by diffusion), holds the possibility of headward erosion and river capturing in low resolution.

For the benefit of a fast computation, a slightly modified and faster method of O'Callaghan and Mark's (1984) drainage accumulation algorithm is implemented and a fast filling method (Planchon and Darboux, 2001) is adapted. Furthermore, time consuming routines that are not needed for a coupled model can be switched off. The possibility of a parallelization is discussed in Sec. 5.2.

In the following, the new SEC for coupling with a 2D lithospheric scale (thermo-) mechanical code, is termed *1D SEC* and the SEC for coupling with a 3D lithospheric scale (thermo-)mechanical code is defined as *2D*. The explicitly formulated 1D code is described in Sec. 3.1 and the explicit 2D code in Sec. 3.2. Sec. 3.3 explains how the coupling of the SECs to lithospheric scale (thermo-)mechanical codes was achieved. Finally, Sec. 3.4 shows partly classical and partly new benchmarks for the implemented codes. The source codes will be published soon at `http://xn--schr-8qa.de/DANSER`.

3.1 Numerical approaches in 1D

2D lithospheric scale (thermo-)mechanical models (in the following called *tectonic models*) are of major interest e. g. for investigating subduction zones and continental collision. If structures vary insignificantly perpendicular to the collision direction, a 3D model is not necessary. Since 2D models have the advantage of significantly faster computation at higher resolution compared to 3D numerical models, I decided to implement both, 1D and 2D surface evolution codes (SEC) for coupling to tectonic codes.

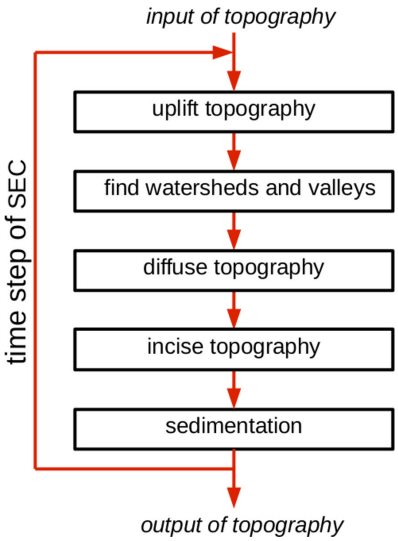

Figure 3.1: *Flowchart of the 1D surface evolution algorithm. The black boxes symbolize the surface evolution functions. The long red arrow on the left symbolizes a loop over the time steps.*

This section describes the new 1D SEC. The routine is implemented on a one dimensional, regular, equidistant, horizontally fixed *grid* of *nodes* and performs

multiple subroutines in every time step (Fig. 3.1 presents the flowchart). In every time step, the tectonic model deforms the topography first. Subsequently, the algorithm identifies the coordinates of watersheds and valleys (Sec. 3.1.1). With the aid of these extrema, the nodes for sediment deposition are identified. Furthermore, the extrema serve for computation of the distance from every node to the corresponding drainage divide. This approximates the channel length that is needed to compute the incision rates. Subsequently, the code uses linear diffusion as approach for hillslope processes (Sec. 3.1.2) and the stream power law, as well as Hack's Law, to simulate riverbed incision (Sec. 3.1.3). Finally, sedimentation is implemented with mass conservation between every pair of neighbouring water divides (Sec. 3.1.4).

3.1.1 Watersheds and valleys

Water divides separate different drainage areas. The deepest point of the valley provides the flow direction in all nodes within the same drainage area. Furthermore, all sediments within one drainage area settle inside the valley. Hence, the coordinates of water divides and valleys are of major importance for the *incision* and the *sedimentation* algorithms. I handle every local maximum of the topography as a water divide and every minimum as a valley.

The algorithm *find_extrema* identifies and stores all extrema of a given topography. It checks whether the elevation of the boundary nodes is higher than their neighbours' elevation. If so, they are stored as local extrema. In that way, the routine identifies each extremum one by one, comparing every three neighbour elevations.

If at least two neighbouring nodes that represent a local extremum have the same elevation, a special handling is needed. For such a *plane*, only the coordinate of one node in the plane is stored. This way, the resulting vector of stored extrema contains alternately maxima and minima. In any case, it starts and ends with maxima.

3.1.2 Linear diffusion

Since Roberts and White (2010) suggest to consider diffusion not only on hillslopes, but even in the riverbed for a transport limited system, I decided to implement linear diffusion for all nodes.

With coordinates x_i, elevations h_i and diffusion rates $\frac{\Delta_t h_i}{\Delta t}$ at node i, the numerical discretisation of the diffusion equation (2.3) is performed employing the central

differences method (Sec. 3.1.3):

$$\frac{\Delta_t h_i}{\Delta t} = \kappa_{hs} \frac{\frac{h_{i+1}-h_i}{x_{i+1}-x_i} - \frac{h_i-h_{i-1}}{x_i-x_{i-1}}}{\frac{x_{i+1}-x_{i-1}}{2}} \tag{3.1}$$

Note that this approach, with equidistant nodes $\Delta x = x_{i+1} - x_i \quad \forall i \in \mathbb{N}$, conserves the mass between each pair of extrema:

$$\sum_{i=k}^{l} \frac{\Delta_t h_i}{\Delta t} = \sum_{i=k}^{l} \kappa_{hs} \frac{(h_{i+1} - h_i) - (h_i - h_{i-1})}{(\Delta x)^2}$$

$$= \sum_{i=k}^{l} \kappa_{hs} \frac{h_{i-1} - 2h_i + h_{i+1}}{(\Delta x)^2} = \kappa_{hs} \frac{h_{k-1} - h_k - h_l + h_{l+1}}{(\Delta x)^2} \tag{3.2}$$

Since for maxima in the intervals $[x_{k-1}, x_k]$ and $[x_l, x_{l+1}]$ follows

$$\frac{h_{k-1} - h_k}{\Delta x} \approx 0 \quad and \quad \frac{h_{l+1} - h_l}{\Delta x} \approx 0, \tag{3.3}$$

$\sum_{i=k}^{l} \Delta_t h_i \approx 0$ is valid for each pair of extrema.

The user may decide between open, fixed boundary or for locally constant diffusion at the boundary and the water-providing node.

3.1.3 Bedrock incision

The riverbed *incision* routine is based on the stream power law (2.5), combined with Hack's Law (2.7). With water discharge Q_i and slope S_i, the bedrock incision rate in node i is implemented as

$$\frac{\Delta_t h_i}{\Delta t} = \kappa_{rb} \cdot {Q_i}^m {S_i}^n.$$

The algorithm computes the slope S_i of every node i via forward differences. The water discharge Q_i in every node is the discretization of (2.10). Starting from every local maximum k_{max}, the algorithm sums up the precipitation rates P_k of all downstream nodes k, down to the node i at channel length L:

$$Q_i = L_i^{p-1} \sum_{k=k_{max}}^{i} P_k. \tag{3.4}$$

Note that the algorithm combines the constants ${k_a}^m$ of Eq. (2.10) and the erodibility κ_{rb} to a new constant.

The topographic gradient serves as input for the stream power law. The fastest way to approach a derivative numerically is via finite differences. Possible computation methods are forward, backward and central differences. Usually, forward differences are used to compute the gradient for the stream power law, but an explanation is often missing (e. g. Willett, 2010). Here, I illuminate the reason for that choice.

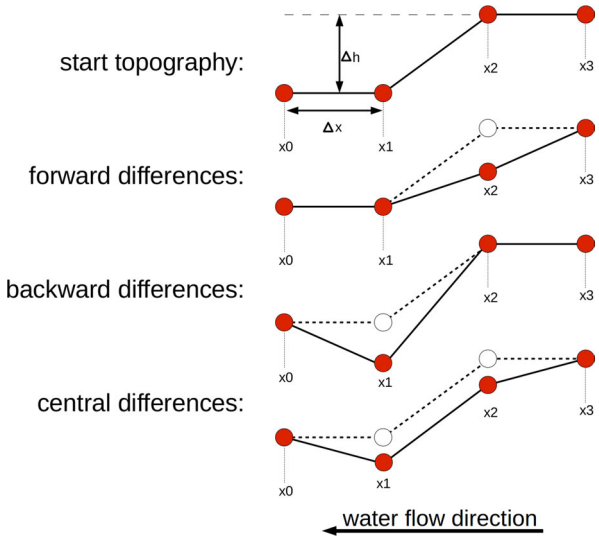

Figure 3.2: *Incision of a step along the riverbed: Four red circles symbolize nodes along the longitudinal river profile. From top to bottom the pictures show the original step, the effect of incision with slopes evaluated via forward, backward and central differences.*

Fig. 3.2 illustrates the process of incision to a steep step in the longitudinal river profile computing the slope according to the three different methods mentioned above. If the slope is computed via forward differences, the only non-zero derivative (and therefore incision rate) will be in the upper node $\underline{x_2}$:

$$\frac{\Delta_t h_2}{\Delta t} \sim \left(\frac{\Delta h}{\Delta x}\right)^n \tag{3.5}$$

with elevation change $\Delta_t h_i$ of node $\underline{x_i}$ per time step Δt, grid node spacing Δx, elevation difference Δh between the nodes $\underline{x_1}$ and $\underline{x_2}$ and stream power law exponent n.

In case the derivative is computed with backward differences the incision rate is zero except for the lower node $\underline{x_1}$:

$$\frac{\Delta_t h_1}{\Delta t} \sim \left(\frac{\Delta h}{\Delta x}\right)^n \tag{3.6}$$

For central differences, the derivative at the two nodes adjacent to the step is equal:

$$\frac{\Delta_t h_1}{\Delta t} = \frac{\Delta_t h_2}{\Delta t} \sim \left(\frac{\Delta h}{2\Delta x}\right)^n \tag{3.7}$$

In case of central differences, the nodes $\underline{x_1}$ and $\underline{x_2}$ get incised equally. Hence, the derivative between them will be preserved. In case of backward differences, $\underline{x_2}$ does not get incised at all. Rather, incision is concentrated on node $\underline{x_1}$, which leads to an increase of the slope. Hence, the stream power law tends to create artificial depressions in riverbeds for both backward and central differences. Alternating between incision and filling of the nodes behind steep slopes make these algorithms highly unstable.

However, in case of forward differences, only node $\underline{x_2}$ gets incised. This leads to upward propagation of steps in a riverbed, as it is observed in the field (e. g. waterfalls and rapids, Grotzinger et al., 2007, p. 436). Another technical feature of the stream power computation by forward differences is a smoothing of river profiles with strongly alternating slopes. Regarding all the mentioned advantages, I decided to implement forward differences in the new SEC.

Note that this argument is also valid for 2D SECs.

3.1.4 Sedimentation

For mass conservation, the material that is removed by incision has to be deposited. This is done by the *sedimentation* algorithm. It collects the incised material between every two local maxima and fills the local minimum in between with the same amount of sediments. In case the sediment volume is bigger than the capacity of the local minimum, the sediments flow over the lower one of the adjacent maxima into the minimum behind (see Fig. 3.3).

If a border of the model is a maximum, sediments from the adjacent nodes flow into the closest minimum. If the border is a local minimum, all the incised material, up to the next maximum, leaves the model. In that case the total mass of the system can change.

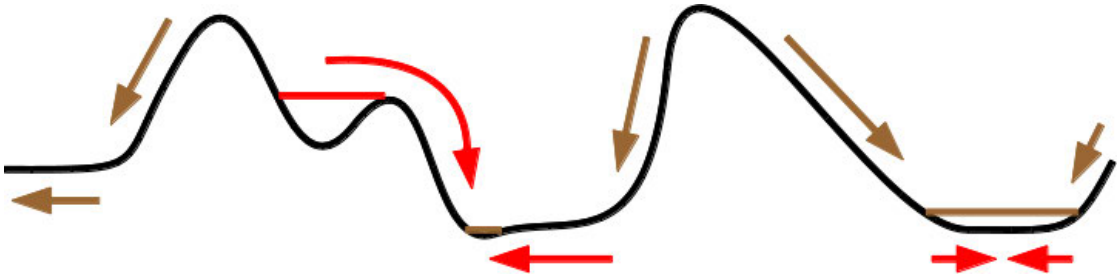

Figure 3.3: *Schematic drawing of the 1D sedimentation algorithm*

3.2 Numerical approaches in 2D

In a region where the topography is almost constant in one direction, a 1D model may reflect the surface processes sufficiently. For more complex models, especially those with outflow of material in more than one direction, a 2D Surface Evolution Model (SEM) is needed.

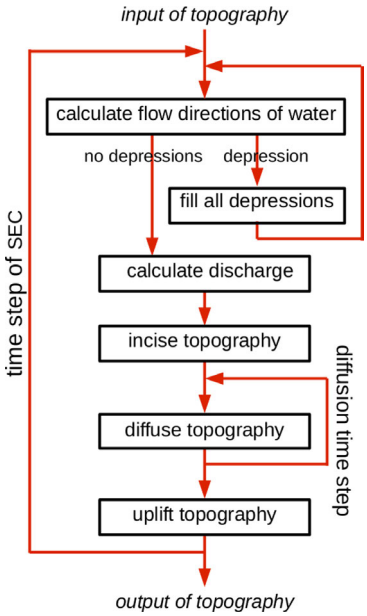

Figure 3.4: *Flowchart of the 2D surface evolution algorithm DANSER. The red arrow on the left symbolizes the surface evolution time steps, the short one on the right the diffusion steps. The algorithm performs the filling cycle (arrow in the upper right corner) once only, if it is needed.*

This section introduces the new and fast 2D Detachment limited lateral Abrasion Nonlinear diffusion Surface Evolution Routine (DANSER). The routine is not only

intended to be applied to simulated topography, but also to DEM. It follows the concept of the cellular automaton (Beaumont et al., 1992, definition in Sec. 3.2.1), implemented on a regular Eulerian grid.

Fig. 3.4 shows the subroutines of DANSER, performed on each time step. A comparison to the flowchart of the 1D model (Fig. 3.1) shows some important differences. Unlike in 1D, in a 2D SEM, one of the major problems are depressions in the topography. The new 1D model fills depressions with eroded material from the associated slopes (Sec. 3.1.4), whereas most of the 2D models do not consider forming depressions (Chase, 1992; Beaumont et al., 1992; Pelletier, 2004). However, no water flow direction can be defined in a depression. Thus, some modellers developed time consuming 2D algorithms that settle the sediment in the lowest cell of a depression (O'Callaghan and Mark, 1984; Howard, 1994; Lin et al., 2008). This results in a filling which takes multiple time steps. However, for big time steps this may lead to mountains of single cells. Furthermore, the size of the depression decides the number of time steps that the depression will be preserved. DANSER uses a new and fast filling algorithm (Planchon and Darboux, 2001) to generate a plane instead of a depression and to remove depressions within a single time step. If enough sediment is produced in every depressions' upstream catchment area, this filling with sediment matches field observations.

Another important difference between 1D and 2D erosion codes is the computation of incision rates. Whereas in the 1D code the water discharge Q in a node is approximated by the distance from water divide and an orthogonal constant precipitation rate (3.4), a 2D code is able to sum up the effective precipitation cell by cell.

Moreover, the flowchart shows an obvious difference in the computation of diffusion rates, because the diffusion time step might get very small compared to the biggest acceptable incision time step, especially for nonlinear diffusion. As an incision time step including computation of flow directions and water discharges is more time consuming than the computation of a diffusion step, I decided to split up each incision time step into multiple diffusion steps.

Sec. 3.2.2 to 3.2.6 explain the subroutines in detail.

3.2.1 The cellular automaton

A *cellular automaton* defines a regular grid. All *cells* in that grid may have one of a finite number of states. The evolution of a single cell from one time step to the next depends just on the state of its neighbours. The new 2D code is based on such a cellular automaton. The underlying grid shown in Fig. 3.5 consists of quadratic cells. The width of one cell is called *cell size*. A *(data) node* is situated

in the centre of each cell and holds all the information about it, like altitude, water discharge or lithology.

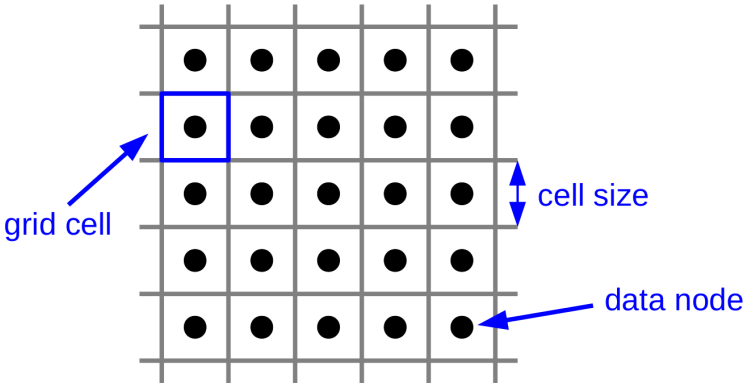

Figure 3.5: *Drawing of a cellular automaton grid. Black dots mark data nodes within the cells.*

Two adjacent cells are called *neighbours (neighbouring cells)*. A *donor cell* or just *donor* is a cell that provides water or sediment to one of its neighbours. A *receiver cell* or just *receiver* is the cell that gets water or sediment from a neighbouring cell. I define a set of at least two neighbouring cells of the same elevation as *plane*.

Computations on an Eulerian grid are much less storage and time consuming than in a Lagragian formulation. For more details about the decision for an Eulerian surface grid see sec. 3.3.2.

3.2.2 Flow directions and filling

In a cellular automaton, water flow directions serve for evaluation of water discharges. However, the flow direction in a depression is not defined. A DEM may contain lakes and other depressions, caused by inaccurate measurements and noise (compare Sec. 4.1.3). But even in simulated topographies tectonics may lead to depressions. In addition, steep slopes may cause strong incision in single cells. In a not sufficiently small time step such a cell may become a depression as well (Sec. 3.2.5). Sec. 3.2.6 points out that even the diffusion algorithm may establish depressions. To ensure that the new SEC is able to handle any topography, a filling of depressions might be needed in every time step.

The *outflow* routine computes the water flow directions with the aid of the D8 algorithm (O'Callaghan and Mark, 1984; Fairfield and Leymarie, 1991). It identifies the steepest descent among the eight neighbours in every cell. In case there is more than one cell of steepest descent, the algorithm prefers diagonal flow directions to

diminish zigzagging rivers. The advantage of preferred flow directions, compared to stochastic chosen directions, is the reproducibility of every model.

If the *outflow* routine does not find a lower cell among its eight neighbours, a depression is identified. Then, a modern *filling* algorithm (Planchon and Darboux, 2001) modifies the topography. Rather than adding offsets to the given topography, it starts with an infinite high topography of the entire model's size. Step by step, it decreases each cell of the topography up to the lowest neighbours elevation plus an offset $\epsilon \leq 1\,cm$, but never less than the original cell elevation. In this way, the forming topography holds neither depressions nor planes and the *outflow* routine is able to compute all flow directions.

This *filling* algorithm fills all depressions in the entire topography at once. This reduces computation time, especially when the DEM contains a high proportion of random noise.

3.2.3 Water discharge

The water discharge is one of the most important input data for the *incision* routine. The new *water_discharge* algorithm is able to cumulate the discharges in all cells without a time consuming sorting algorithm and is faster than other algorithms that compute the upstream drainage area for each cell (Martz and Garbrecht, 1992; O'Callaghan and Mark, 1984).

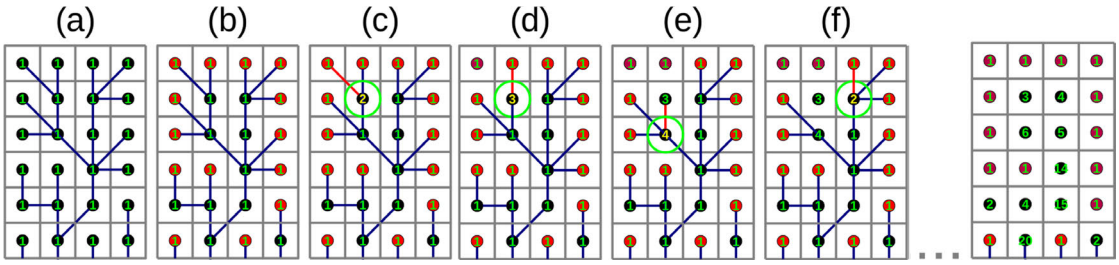

Figure 3.6: *Drainage area computation in 2D. The cellular grid is drawn in grey, red dots mark the springs, the numbers within the dots give the current amount of water discharge in that cell, the green circles mark changes, the blue connections depict the river network (water flow directions) and the red connections point out where the algorithm is just evaluating, from the spring up to another inflowing stream. From left to the right, the springs are identified (b) and the cumulation of water discharge starts (c)-(f).*

The algorithm is slightly transformed and therefore faster as O'Callaghan and Marks (1984) drainage accumulation algorithm. Similar to their algorithm, the

new and fast *inflow* algorithm counts and stores the number of inflowing streams per cell. Iterating each cell, it increases its receiver cell entry in a zero-initialized inflow matrix by one. This identifies cells without inflowing streams as springs.

Afterwards, the *water_discharge* routine handles the matrix of precipitation rates as matrix of water discharges and modifies it. Fig. 3.6 explains this procedure using the example of a locally constant precipitation rate (a). From each spring (b), one by one, a cell pointer advances in flow direction (c). In every cell the pointer processes, it adds its discharge to the receiver cell, marked by a green circle. In any cell with more than one incoming stream (c, e, f) the algorithm decreases the associated entry in the inflow matrix by one (illustrated by the removal of the red line, indicating the channel from the spring up to such a potential river mouth). Then, it continues the computation at the next spring (c, d, f) until no spring is left.

The new routine processes every cell exactly two times, one time to count the number of inflowing streams and a second time to add its final water discharge to the receiver cell. In contrast, O'Callaghan and Marks algorithm processes each cell multiple times. The number of cells of the longest river specifies the number of iterations. Thus, the new algorithm decreases the iterations by a factor of $\frac{\sharp cells(\text{longest river})}{2}$. Particularly for high resolution grids, this strongly decreases the computation time.

3.2.4 Spread water discharge: lateral incision

Usually, in surface evolution models an incised channel has a discretionary width of one cell, no matter what cell size is chosen. When working with high resolution, the natural equivalent may contain multiple cells in width. Furthermore, braided streams, meanders, forth and back drifting riverbeds, or downstream sweep erosion (Cook et al., 2014) may cause even larger valleys. In shallow regions (e. g. deltas) the multiple flow direction algorithm (Freeman, 1991, see Sec. 2.2.2 for details) is able to distribute the water discharge over several cells (Pelletier, 2004). But for steep slopes (e. g. Daan River in Taiwan, Cook et al., 2014), this method does not work. Hence, I decided to extend the *drainage_area* routine to a more versatile algorithm than the multiple flow direction.

To spread the water discharge over the whole riverbed, I attach the *spread_water* algorithm (shown in Fig. 3.8) to the computation of the water discharges. For each grid cell i, it evaluates the incision radius r_i^{lat}, that depends linearly on the computed water discharge in that cell. This radius describes a circle around the cell i. For a faster computation, this circle is approached by a squared window. Within this window of $2r_i^{lat} \times 2r_i^{lat}$ cells around the cell i, the water discharges Q_i

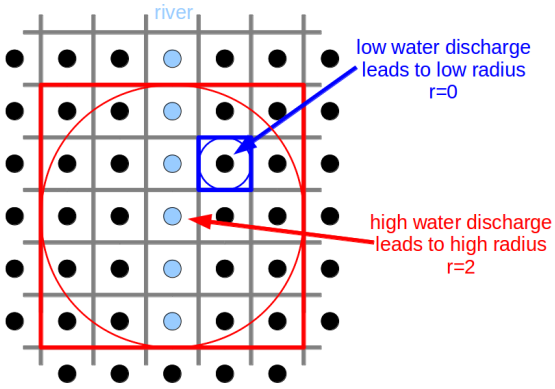

Figure 3.7: *Evaluation of the spread water discharge. The grid of the cellular automaton is drawn in grey, dots mark the grid nodes. Nodes with high water discharge after the* drainage_area *algorithm are coloured in faded blue. The blue and red circles give examples for the incision radii r_i^{lat} for low and high water discharges. The squares frame the cells that are taken into account for the cumulated water discharge in the according cells.*

are collected, summed and spread equally over all collection cells:

$$Q_i^{lat} = \frac{\sum\limits_{k \in M_i} Q_k}{\#M_i}, \tag{3.8}$$

with

$$|x_k - x_i| < r_i^{lat} \quad \wedge \quad |y_k - y_i| < r_i^{lat}.$$

Steep slopes in the riverbed in water flow direction are a hint that the water flow direction is orthogonal to the longitudinal river profile into a u- or v-shaped channel. Thus, the algorithm skips cells with steep slopes S_k in flow direction or large elevation difference to the donor cell to prevent the river from spilling over the valley margin:

$$\begin{aligned} M_i := \Big\{ k \;\Big|\; & |x_k - x_i| < r_i^{lat} \quad \wedge \quad |y_k - y_i| < r_i^{lat} \\ & \wedge \; |h_k - h_i| < \Delta h_i^{lat} \quad \wedge \quad S_k - S_i < S^{lat} \Big\} \end{aligned} \tag{3.9}$$

with the maximal elevation difference $\Delta h_i^{lat} := c_{\Delta h} \cdot Q_i$, the spreading radius $r_i^{lat} := c_{rad} \cdot Q_i$, the spreading slope S^{lat} and lateral incision controlling constants $c_{\Delta h}$, $c_{rad} \in \mathbb{R}^+$.

If a cell i is within the range of several lateral incision cells J, it receives the spread discharge from the set M_i of highest cardinality $\#M_i$. That means this cell gets

```
for (all cells of the surface grid) {

  radius = radiusMult * water
  deltaH = deltaHMult * water
  heightMax = height + deltaH
  heightMin = height - deltaH
  slopeMax = slope + offsetSlope

  // sum water discharge inside of the window
  nCells = 0;
  meanWater = 0;
  for (all cells within a square of 2*radius size around the cell) {
    if ( (height <= heightMax) && (height >= heightMin)
          && (slope <= slopeMax) ) {
      nCells++
      meanWater += water
    }
  }
  meanWater = meanWater/nCells

  // distribute water discharge inside of the window
  nDonors = 0
  for (all cells within a square of 2*radius size around the cell) {
    if ( (height <= heightMax) && (height >= heightMin)
          && (slope <= slopeMax) && (nDonors < nCells) ) {
      waterSmooth = meanWater
      nDonors = nCells
    }
  }

}
```

Figure 3.8: *Pseudocode of the spread_water algorithm*

its discharge from the set M_i that includes more cells than all the other sets that includes the cell:

$$k \in \bigcap_{l \in J} M_l \quad \Rightarrow \quad \left(Q_k^{lat} := Q_i^{lat} \quad with \;\; i \in J \;\; | \;\; \#M_i \geq \#M_l \;\; \forall \, l \in J\right). \qquad (3.10)$$

This feature guarantees a smoothing of water discharges in space. Additionally, it enables incision inside the whole river valleys. Fig. 4.5 in Sec. 4.1.4 shows topographic maps with resulting water discharges compared to the usual discharges. Sec. 4.2.2 explains further advantages of the new algorithm.

3.2.5 Incision

The supply-limited *incision* routine is based on the accepted stream power law (2.5). In every cell, the routine requires the slope in flow direction and the water discharge as input. For stability reasons, the calculation of the slope is implemented via forward differences (see Sec. 3.1.3 for more details). Sec. 3.2.3 explains the computation of water discharges.

The boundary is open for sediment flux, and the user may choose between fixed boundary (no incision at any boundary cells) and a maximum incision rate I_{bound} at the boundary. In the latter case, the incision rate of the upstream cell of highest water discharge is copied to the boundary cell. To prevent the model from oversteepening the boundary slopes, the incision rate is limited to the mentioned maximum I_{bound} at all boundary cells.

Without explanation, Davy and Lague (2009) and Tucker and Bras (1998) suggest an incision threshold I_{min}, below that no incision happens. This makes the occurrence of incision dependent not only on drainage area, but also on channel slope. Contradictorily, they choose $I_{min} = 0$ due to a lack of data. However, observations show that a channel starts to incise when a critical amount of water discharge is exceeded, mostly independent of the steepness. Thus, I adopt the idea of a water discharge threshold Q_{min} (O'Callaghan and Mark, 1984). More precisely, DANSER defines a river channel where the water discharge exceeds the threshold value Q_{min} (see Sec. 2.2.2 for more details about this channel initiation function).

All known SECs make incision dependent on diffusion in a way that the diffused material settles in the channel, and thus modifies the river slope. The new *incision* routine removes the incised and the diffused material from the well defined river channels immediately and neglects sedimentation. This approach is supported by the supply-limited stream power law. The new approach leaves the incision code decoupled from diffusion, since effectively no diffusion happens in cells where incision takes place and vice versa. It has to be mentioned that decoupling incision from diffusion is non-physical. In fact, not only the shear-stress of water but saltating and abrasing sediments cause incision (Sklar and Dietrich, 2001). Hence, both processes, incision and diffusion, are dependent on each other. But up to now, the coupling between sediment load and incision of rivers is not yet completely understood. For this reason, I decided to decouple incision from diffusion with the benefit of a simpler calibration (see Sec. 4.1 for more details).

Dependence on resolution

The stream power law (2.5) suggests that the incision rate in a channel depends on the volume of water flowing through it. Hence, the local incision rate is not

dependent on the resolution of the model or the channel width. However, this approach leaves the amount of sediments that gets removed by incision resolution dependent, because the amount of incised material is dependent on the channel width.

The routine *spread_water* spreads the water discharge over several cells and therefore reduces the water volume in the former main stream. With the original stream power law, this leads to a resolution dependent incision rate. Rather than keeping the water volume independent of cell size, the water flux through a vertical cross section of $1\,m$ width, $\frac{Q}{\Delta x}$, should be considered for the new approach.

A modification of the stream power law to

$$\frac{\delta h}{\delta t} = \widetilde{\kappa_{rb}} \cdot \left(\frac{Q}{\Delta x}\right)^m S^n, \tag{3.11}$$

is simply a substitution of the incision coefficient $\widetilde{\kappa_{rb}} = \kappa_{rb} \cdot \Delta x^m$ with grid node spacing Δx.

Assuming a resolution independent water flux, I implement the modified stream power law (3.11) as

$$\frac{\Delta_t h_i}{\Delta t} = \kappa_{rb} \cdot \left(\frac{Q_i}{\Delta x}\right)^m S_i^n. \tag{3.12}$$

With the modified stream power law, a channel of width w_c on low resolution $\Delta x = w_c$ has similar effect as an equally spread river with same width, but high resolution $\Delta x = \frac{w_c}{k}$, $k \in \mathbb{N}$.

This statement gets obvious on closer examination: The water discharge $Q := Q_l$, $l \in \mathbb{N}$ in any cell of low resolution is k times as high as the discharge $\frac{Q}{k}$ in any of the correspondent cells of high resolution. Equal incision rate on both resolutions results from

$$\frac{\Delta_t h_l}{\Delta t} = \kappa_{rb} \cdot \left(\frac{Q}{w_c}\right)^m S_l^n = \kappa_{rb} \cdot \left(\frac{\frac{Q}{k}}{\frac{w_c}{k}}\right)^m S_l^n. \tag{3.13}$$

Note that the modification of the stream power law changes κ_{rb}, but guarantees a resolution-independent incision rate and sediment production.

Time stepping

Scholars (e. g. Braun and Sambridge, 1997; Kurfess and Heidbach, 2009) choose incision time step lengths of $100\,y$ to induce a stable surface evolution. This section discusses whether this time step is sufficiently small for the new *incision* routine.

The time step length Δt is sufficiently small if it avoids filling, since filling might lead to oscillations of elevation. Hence, the sum of elevation h_d and negative incision depth $\Delta_t h_d$ in a donor cell d must be larger than the elevation of the receiver cell r after incision:

$$h_r + \Delta_t h_r \leq h_d + \Delta_t h_d$$

Inserting the modified stream power law (3.12) gives

$$h_r - \kappa_{rb} \cdot \left(\frac{Q_r}{\Delta x}\right)^m {S_r}^n \cdot \Delta t \leq h_d - \kappa_{rb} \cdot \left(\frac{Q_d}{\Delta x}\right)^m {S_d}^n \cdot \Delta t$$

I transform the inequality to

$$({Q_d}^m {S_d}^n - {Q_r}^m {S_r}^n) \cdot \Delta t \leq \frac{(\Delta x)^m}{\kappa_{rb}} \cdot (h_d - h_r).$$

Neglecting stream bifurcation points, I assume nearly equal water discharges in the two neighbouring cells $Q_d \approx Q_r$:

$$({S_d}^n - {S_r}^n) \cdot \Delta t \leq \frac{(\Delta x)^{m+1}}{\kappa_{rb} \cdot {Q_d}^m} \cdot S_d. \tag{3.14}$$

For a convex profile ($S_d < S_r$), this gives

$$\Delta t \geq \frac{(\Delta x)^{m+1}}{\kappa_{rb} \cdot {Q_d}^m} \cdot \frac{S_d}{{S_d}^n - {S_r}^n}.$$

Since the right side is negative and Δt positive, this condition is always fulfilled.

A concave profile ($S_d > S_r$) leads to

$$\Delta t \leq \frac{(\Delta x)^{m+1}}{\kappa_{rb} \cdot {Q_d}^m} \cdot \frac{S_d}{{S_d}^n - {S_r}^n}. \tag{3.15}$$

For an approximately linear river profile ($S_d \approx S_r$), Δt can be chosen extremely high, but in the case of a small slope at the receiver cell r ($S_r \approx 0$), the condition gives

$$\Delta t \leq \frac{(\Delta x)^{m+1}}{\kappa_{rb} \cdot {Q_d}^m} \cdot {S_d}^{1-n}. \tag{3.16}$$

For $n > 1$, the maximal slope and the maximal water discharge are the limiting factors for the time step. For $n \in [0, 1]$, the water discharge and the minimum

slope should govern the time stepping. Assuming $n \in [0, 1]$, the minimum elevation difference between the neighbours d and r affects the stability of the algorithm. The minimum elevation difference ϵ is governed by the *filling* routine. Hence, the time step has to fulfil

$$\Delta t \leq \frac{(\Delta x)^{m+n} \cdot \epsilon^{1-n}}{\kappa_{rb} \cdot {Q_{max}}^{m}}. \tag{3.17}$$

for a totally stable algorithm.

The fixed values $\Delta x = 150\,m$, $\epsilon = 0.001\,m$, $m = 0.3$ and $n = 0.7$ (see Sec. 4.1) lead to

$$\Delta t \lesssim \frac{18.9}{\kappa_{rb} \cdot {Q_{max}}^{0.3}}. \tag{3.18}$$

For a model of 3000×2000 cells and constant precipitation rate, the water discharge will not exceed the discharge of $6000,000 \cdot (\Delta x)^2$. Hence, if the time step length is chosen to be $\Delta t = 100\,y$, κ_{rb} should not exceed 0.002 much. The following model stays within that range. Using the mentioned time step length, the *incision* routine turned out to smooth riverbeds (Sec. 3.1.3). This fact indicates the stability of the time step.

Note that the stability condition (3.16) is valid for the 1D incision code as well. Since ϵ might be zero, the 1D *incision* routine sets the incision rate for nodes with slopes smaller than $S_{min} = 0.0001$ to zero. With maximum channel length L and maximum precipitation rate P_{max}, this leads to the stability condition

$$\Delta t \leq \frac{\Delta x \cdot {S_{min}}^{1-n}}{\kappa_{rb} \cdot (L^h \cdot P_{max})^m}. \tag{3.19}$$

3.2.6 Diffusion

In most SEM, linear diffusion combines all hillslope processes in a first order approach. On one hand, I adopt Beaumont's implementation (Beaumont et al., 1992) of the diffusion equation (2.3), on the other hand, I implement nonlinear diffusion (2.4). Both *diffusion* algorithms are based on the continuity equation (2.1) and finite differences.

With diffusion rate $\frac{\Delta_t h_i}{\Delta t}$ in cell i, sediment flux $(q_s)_{i,j}$ between cell i and one of the four straight neighbouring cells j, the continuity equation is implemented as

$$\frac{\Delta_t h_i}{\Delta t} = \frac{1}{\Delta x} \sum_{\{\, j \mid (x_j = x_i \wedge y_j = y_i \pm 1) \vee (y_j = y_i \wedge x_j = x_i \pm 1)\}} (q_s)_{i,j}. \tag{3.20}$$

The routine uses finite differences for the diffusive sediment flux as well as for the nonlinear weighting factor $w_{i,j}$ between donor cell i and receiver cell j:

$$(q_s)_{i,j} = \kappa_{hs} \left(\frac{h_j - h_i}{\Delta x} \right) \cdot w_{i,j} \tag{3.21}$$

$$w_{j,i} := w_{i,j} := \begin{cases} 1 & \text{for} \quad \text{linear diffusion} \\ \left[1 - \left(\dfrac{u_i}{S_c \cdot \Delta x} \right)^2 \right]^{-1} & \text{for} \quad \dfrac{u_i}{S_c \cdot \Delta x} < 0.99 \\ \left[1 - 0.99^2 \right]^{-1} \approx 50.25 & \text{for} \quad \dfrac{u_i}{S_c \cdot \Delta x} \geq 0.99 \end{cases} \tag{3.22}$$

$$u_i := \sum_{\{k \mid (x_k = x_i \wedge y_k = y_i \pm 1) \vee (y_k = y_i \wedge x_k = x_i \pm 1)\}} |h_i - h_k| ,$$

with the diffusivity κ_{hs}, the elevation difference between two cells $h_i - h_k$, the critical value of the slope S_c and the sum u_i of elevation differences between the donor cell and its four neighbours.

As discussed in Sec. 2.2.1, the weight $w_{i,j}$ is only slightly above 1 for small u_i compared to $S_c \cdot \Delta x$. That means, for small u_i the linear diffusion is a good approximation. However, with increasing u_i the weight $w_{i,j}$ becomes much larger than 1 and when u_i approaches $S_c \cdot \Delta x$, $w_{i,j}$ will go towards infinity. For numerical reasons, I set $w_{i,j}$ to a constant for $u_i > 0.99\, S_c \cdot \Delta x$.

Both linear and nonlinear diffusion allow fluxes from one cell to its four straight neighbours and precisely conserve the mass in the inner cells of the model. Complete mass conservation can be achieved by forbidding material flux from the boundary cells out of the model. Another possible boundary condition is a fixed elevation in all boundary cells. This simulates diffusive sediment flux through the boundary. The user may choose between these two boundary conditions.

Need for filling

Own simulations have shown that the 2D diffusion algorithm may cause depressions. This paragraph explains why depressions may evolve.

Fig. 3.9 gives an example for a forming depression, owing to the *diffusion* algorithm. The blue cell in the centre is surrounded by slightly higher cells and a single neighbour of lower altitude (green). This leads to a low sediment supply into this cell. The green cell is highly positively diffused, because it receives a large amount of sediments from two of its neighbours. This will certainly increase the elevation

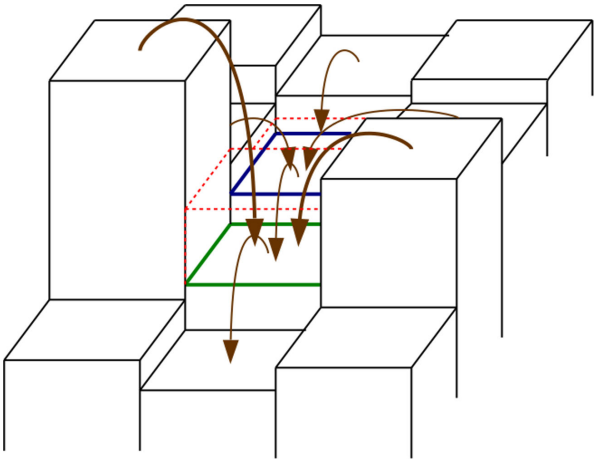

Figure 3.9: *Chart of the 2D diffusion algorithm when it generates a depression. The cellular elevations are painted in black, the brown arrows indicate the sediment flux and the resulting elevation in the two centre cells is drawn in red.*

of the green cell more than the elevation of the blue cell and may result in a higher elevation of the green centre cell. A depression has evolved.

Since the elevation difference between two neighbouring cells may be as small as ϵ (Sec. 3.2.2), particularly in a DEM, generating depressions like this cannot be avoided without making the algorithm much more computationally expensive (see implicit methods, Willett, 2010). Hence, the *filling* routine has to fill depressions not only formed by incision but also by *diffusion*.

Time stepping

In the following, I develop a condition to stabilise the diffusion algorithm. The condition avoids oscillation of elevation change $\Delta_t h_i$. If the elevation of cell i was increased in one time step, it may not be decreased in the next step or the other way around.

I examine the elevation change of cell i, neglecting the change of all neighbours j. With operator Δ_t for (elevation) change in time, the continuity equation (3.20) and the diffusive flux (3.21), the elevation change of cell i is

$$\Delta_t h_i = \frac{\kappa_{hs} \cdot \Delta t}{(\Delta x)^2} \cdot \sum_j \Big([h_j - h_i] \cdot w_{i,j} \Big)$$

The elevation change of cell i in the following time step is

$$\Delta_t(h_i + \Delta_t h_i) = \frac{\kappa_{hs} \cdot \Delta t}{(\Delta x)^2} \cdot \sum_j \Big([h_j - (h_i + \Delta_t h_i)] \cdot (w_{i,j} + \Delta_t w_{i,j}) \Big)$$

$$= \frac{\kappa_{hs} \cdot \Delta t}{(\Delta x)^2} \cdot \left(\sum_j \Big[(h_j - h_i) \cdot (w_{i,j} + \Delta_t w_{i,j}) \Big] - \sum_j \Big[\Delta_t h_i \cdot (w_{i,j} + \Delta_t w_{i,j}) \Big] \right)$$

$$\approx \Delta_t h_i - \frac{\kappa_{hs} \cdot \Delta t}{(\Delta x)^2} \cdot \Delta_t h_i \cdot \sum_j (w_{i,j} + \Delta_t w_{i,j})$$

$$= \Delta_t h_i \cdot \left(1 - \frac{\kappa_{hs} \cdot \Delta t}{(\Delta x)^2} \cdot \sum_j (w_{i,j} + \Delta_t w_{i,j}) \right)$$

The mentioned condition that $\Delta_t h_i$ and $\Delta_t(h_i + \Delta_t h_i)$ must have the same sign, is logical equivalent to

$$0 \leq 1 - \frac{\kappa_{hs} \cdot \Delta t}{(\Delta x)^2} \cdot \sum_j (w_{i,j} + \Delta_t w_{i,j})$$

Since $w_{i,j} + \Delta_t w_{i,j}$ is defined as positive for all i and j, this leads with (3.22) to

$$\Delta t \leq \frac{(\Delta x)^2}{\kappa_{hs} \cdot \sum_j (w_{i,j} + \Delta_t w_{i,j})} \leq \frac{(\Delta x)^2}{201 \kappa_{hs}}. \tag{3.23}$$

Linear diffusion ($w_{i,j} = 1$, $\Delta_t w_{i,j} = 0 \ \forall i, j$) reduces the term to

$$\Delta t \leq \frac{(\Delta x)^2}{4 \kappa_{hs}}. \tag{3.24}$$

This result defines the upper bound for a stable diffusion algorithm more precisely than Beaumont et al. (1992) does. Note that in a 1D SEM the sum in (3.23) has just two summands. Hence, the denominator reduces to $2\kappa_{hs}$.

In SECs, short-range transport processes are usually coupled to long range transport, using the same time step in the range of hundreds of years (Beaumont et al., 1992; Braun and Sambridge, 1997; Kurfess and Heidbach, 2009). Using linear diffusion, this is reasonable even for high resolution ($\Delta x < 100\,m$) and high diffusion rates ($\kappa_{hs} > 1$). But for nonlinear diffusion, a time step of $100\,y$ could lead to a highly unstable algorithm, as (3.23) reveals. Since one computation of all diffusion rates is less time consuming than the computation of incision rates, I decouple the diffusion time step from the incision step. This allows smaller diffusion steps, keeping the incision step constant.

3.3 Coupling with tectonics

Numerical modelling can serve as a tool for studying the influence of surface processes on tectonic deformation. To fulfil this purpose, the presented Surface Evolution Codes (SECs) are designed for coupling with (thermo-)mechanical codes that model lithospheric-scale processes with free surface (in the following named *tectonic codes*). This section presents how the coupling is implemented. I focus on the coupling of the 2D SEC to a 3D tectonic code. The 1D/2D coupling is a reduction of this case.

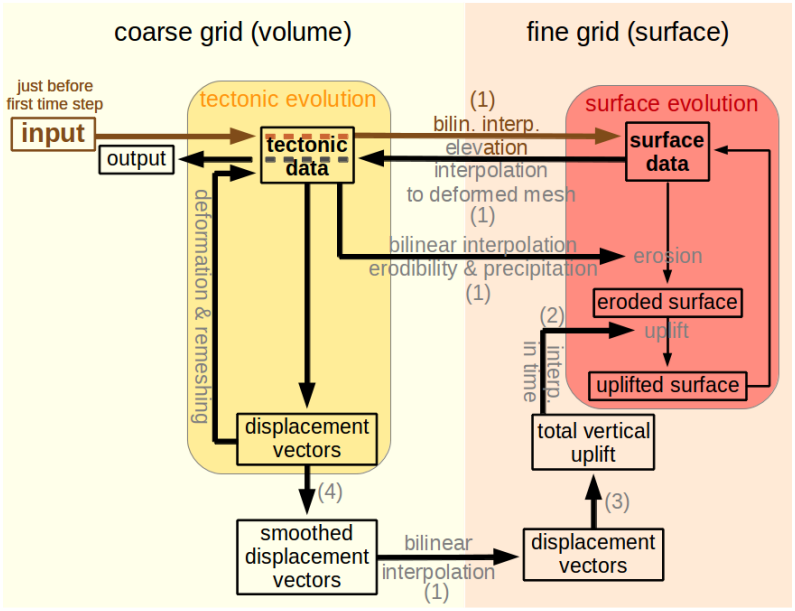

Figure 3.10: *Coupling of DANSER to a tectonic code. Black boxes symbolize data matrices and arrows illustrate methods of data computation. The brown arrows indicate a computation that is performed once before the first tectonic step. The numbers in brackets refer to the subsections. 1 refers to Sec. 3.3.1, 2 refers to Sec. 3.3.3, 3 refers to Sec. 3.3.2 and 4 refers to Sec. 3.3.4.*

Processes modelled by SEMs require a higher spatial resolution than a tectonic model. In addition, it consumes remarkably more time to execute one time step of a tectonic code than that of a SEC, which makes bigger tectonic time steps desirable. As a consequence, a modern coupling method of SECs and tectonic codes should include the option to interpolate both spatially and temporally between the two.

Fig. 3.10 illustrates the coupling of DANSER to a tectonic code. Before the first tectonic time step, the surface elevations are extracted from the tectonic model and interpolated to the higher resolution SEM (see Sec. 3.3.1 for a more detailed

explanation). This fine grid with initial elevation data is stored in a static array.

After every tectonic step, erodibilities and precipitation rates are interpolated to the SEC (Sec. 3.3.1). Furthermore, the tectonic code passes the surface deformation data in form of three-dimensional displacement vectors to the SEC. Smoothed (Sec. 3.3.4) and interpolated to the fine surface grid (Sec. 3.3.1), these vectors are used to evaluate the total uplift in every cell (Sec. 3.3.2). Linear interpolation in time (Sec. 3.3.3) is used to compute the averaged uplift rates. DANSER continues with alternating uplift and erosion computations in finer time steps. Subsequently, the new fine resolution elevation data are stored for the next tectonic step in the mentioned array. Finally, the high resolution elevation data are interpolated (Sec. 3.3.1) onto the deformed (and eventually remeshed) coarse topography and used to modify the surface coordinates of the underlying tectonic model. Thereafter, the tectonic code performs the next time step.

As mentioned above, the coupling of the 1D SEC to a 2D tectonic model is a reduction of this case. For simplification, the 1D uplift rate is not computed with the aid of displacement vectors, but as height difference between old and new topography. This approach transfers horizontal displacements of the tectonic model into vertical uplift of the SEM. As a consequence, high frequency elevation oscillations on the fine grid are locally fixed and barely influence the coarse mesh. The absence of strongly incising rivers in a 1D SEM and the potentially high resolution of a 2D tectonic model lead to structures with similar wavelength in the SEM and the tectonic model. Hence, the error resulting from the negligence of the horizontal displacements is assumed to be small in comparison to a 2D SEM.

3.3.1 Interpolation and averaging

The resolution of tectonic models is chosen in km-scale, while the resolution of orogenc-scale SEMs is usually much lower. Thus, a method for the interpolation between different resolutions for coupled tectonic and surface evolution models is needed.

As a requirement for the coupling, the tectonic model should provide a topography that consists of surface nodes with elevation data. The surface nodes have to be arranged as a quadrilateral, structured mesh. Additionally, precipitation rates and erodibility factors should be provided in these nodes. Furthermore, the tectonic code must provide 3D displacement vectors for every time step.

Given the surface node spacing Δx, the resolution $nx \times ny$ and the position of the first cell $\underline{x_0}$, the *initialization* routine constructs an Eulerian fine surface grid. In case of horizontal displacement, the tectonic model may expand the domain to a region that is not covered by the SEM. This will avoid erosion in these cells. In

that case, the user is advised (but not required) to choose the surface model larger than the tectonic surface.

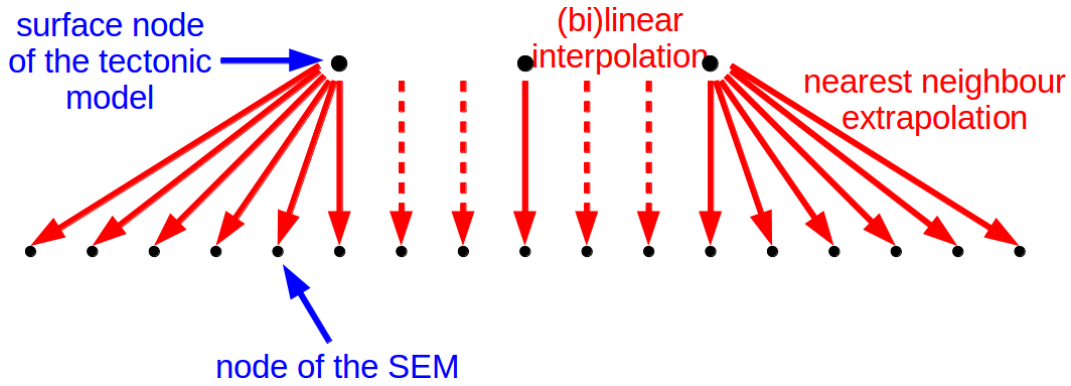

Figure 3.11: *Data interpolation from low to high resolution. Big black dots illustrate the low resolution nodes, the small ones represent the high resolution nodes. Dashed red arrows symbolize (bi)linear interpolation from low to high resolution and the other red arrows symbolize that the data gets copied.*

Before the tectonic deformation starts, the low resolution surface elevations are bilinearly interpolated to the fine grid, as Fig. 3.11 illustrates. Cells outside of the coarse mesh are approximated by copying the elevation of the nearest low resolution node. These initial elevations are stored in a static array.

After every tectonic time step the resulting 3D displacements, the erodibility and the precipitation rates are bilinearly interpolated to the fine grid (similarly to the elevations before the first tectonic time step, see Fig. 3.11). For cells outside of the coarse grid the erodibility and the precipitation rate of the nearest neighbour gets copied. The user may choose whether the displacements for those cells are set to zero (*fixed boundary*) or whether they get copied from the nearest neighbour (*free slip*).

The interpolated displacement vectors serve for evaluation of the total uplift (see Sec. 3.3.2 for details). After performing several erosion time steps, followed by applying the temporally interpolated uplift (see Sec. 3.3.3 for details about interpolation in time), the modified elevations are averaged and projected to the deformed surface of the tectonic mesh. The new elevation data are used to modify the surface of this mesh. To compute the average, each high resolution cell is assigned to its nearest low resolution node. All cells that are associated with a particular node are considered in the unweighted average for this node.

The applied interpolation methods should satisfy mass conservation. If one of the interpolation methods added or removed material, this change would be erroneously treated as result of the surface evolution. For this reason, I decided for

bilinear interpolation from low to high resolution. In the opposite direction, the routine interpolates by averaging, because bilinear interpolation from high to low resolution is not mass conserving.

3.3.2 From deformation to uplift rate

After interpolating the surface displacement vectors from low to high resolution, the resulting uplift has to be added to the topography in multiple time steps. Fig. 3.12 illustrates how the vertical uplift is computed.

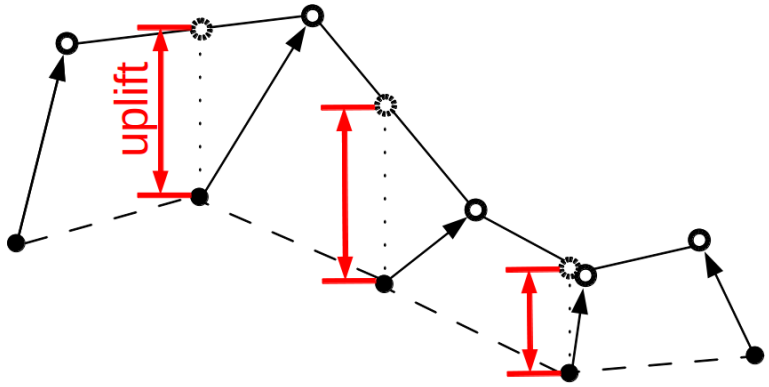

Figure 3.12: *Computation scheme of the vertical uplift in the high resolution surface nodes. Dots symbolize the surface nodes and arrows the displacement vectors. Circles represent the displaced nodes and dashed circles indicate the bilinearly interpolated elevations. The red arrows symbolize the resulting uplift in each high resolution surface node.*

The high resolution surface displacement vectors are added to a copy of the fine grid. This process deforms the equidistant grid. Bilinear interpolation projects the new elevations to the original surface grid. The subtraction of original and projected elevations gives the total vertical uplift in each cell. The uplift rate might be nonlinear in time. However, the nonlinear effect is negligible for relatively low mass movement in horizontal direction. Hence, the total uplift is linearly interpolated to the finer surface evolution time steps.

Another way is to break up the displacement vectors in regular parts, add them to the topography and interpolate the resulting heights back to the original grid in each surface evolution time step. Unfortunately, the large number of interpolations leads to accumulation of errors and is computationally expensive. The accumulated errors can be bigger than the error that is caused by linear interpolation of the uplift rates.

A more accurate way to compute the modification of the topography is a Lagrangian surface grid (e. g. Braun and Sambridge, 1997). This would lead to much higher costs for computing derivatives, like terrain slope and curvature. Furthermore, a strongly deforming grid must be remeshed regularly. The solution stated above is exactly the same as a Lagragian SEM with remeshing before every tectonic time step. In order to find a path between accuracy on the one hand and fast computation on the other hand, I choose bilinear interpolation.

3.3.3 Splitting of the time step

A conventional time step for tectonic models is within the order of tens of thousands of years (Beaumont et al., 1992; Kurfess and Heidbach, 2009; Popov and Sobolev, 2008). To guarantee a stable surface evolution, usually a time step of hundreds of years (Beaumont et al., 1992; Braun and Sambridge, 1997; Kurfess and Heidbach, 2009) is chosen. For the coupling of a SEM to a tectonic model, it is necessary either to reduce the time step size of the time consuming tectonic code, or to split it into smaller ones. Here, I point out how I implement the coupling in time.

The coupling method divides every tectonic time step into multiple erosion steps of equal duration. In these fragmented time steps, the surface is alternately uplifted and eroded. This method ensures that the surface lifts continuously during surface evolution.

The user of DANSER can choose between manual and automatic time steps. In the latter case the time step size is chosen in such a way that the incision stability condition (3.17) derived in Sec. 3.2.5 is satisfied. Manual time stepping means that the user chooses a fixed time step. For the stability of the diffusion algorithm, the incision step is split in smaller ones, as descibed in Sec. 3.2.6. This method fulfils the stability condition in (3.23) or (3.24).

3.3.4 Smoothing

A challenge for every coupled SEC are high frequency surface anomalies in the underlying tectonic model. High frequency surface anomalies are single nodes at the free surface with large or low elevation compared to its neighbours, caused by instabilities in tectonic codes. Especially in 1D SEMs, these anomalies may form water divides and trap sediments. Thus, they must be removed.

Most of the tectonic codes that involve a free surface include a surface smoothing in every time step to reduce the instabilities (Popov and Sobolev, 2008; Huismans,

2014). This smoothing leaves the displacement vectors themselves unsmoothed. Since the displacements transfer the movement from the tectonic model to the SEM, this kind of smoothing is not transferred to the high resolution surface.

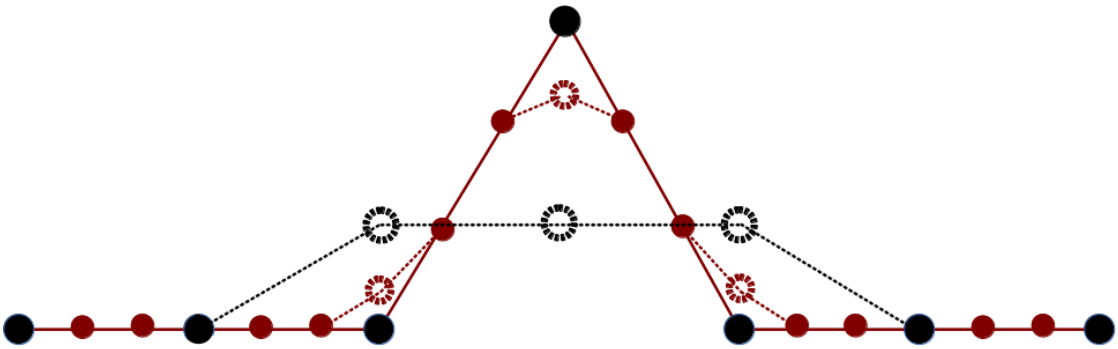

Figure 3.13: *Comparison of a high frequency anomaly smoothed in low and high resolution. Black dots symbolize the coarse mesh and red and black dots together represent the fine grid. Dashed circles indicate the node elevation after one step of strong smoothing. The graphic shows that a smoothing in high resolution slightly affects the anomaly. The smoothing in low resolution shows a much stronger influence.*

The introduced SECs smooth the topography by linear diffusion. But Fig. 3.13 makes clear that an anomaly in a single low resolution node will be partly transmitted by interpolation to all high resolution nodes close by. Therefore, a smoothing in high resolution is not able to fully remove high frequency anomalies.

Hence, the 2D code DANSER includes its own weighted *smoothing* routine with window size n_{smooth}. This routine smoothes the low resolution displacement vectors. The higher n_{smooth}, the stronger the smoothing. Although it is not recommended, the user may switch the smoothing off by setting $n_{smooth} = 0$.

Any other surface smoothing should be switched off for coupling a 3D tectonic code to DANSER. The in-built smoothing routine performs much better, as stated above.

3.3.5 Mass conservation

An intended application for the presented SECs is the Pamir orogen. Surface processes carry mass out of the Pamir, which was transferred into it by tectonic processes. This is why the SEMs are not intended to be fully mass conserving.

DANSER neglects sedimentation and instead *filling* (Sec. 3.2.2) takes place. In addition, there might be outflow of diffused material at the model boundaries.

The 1D SEC has sediment outflow, if a boundary node is a local minimum.

If mass conservation is required, it is possible to adjust the tectonic uplift to the sediment outflux. The tool *accumulate_sediments* (Sec.A) computes the total amount of outflowing sediments in DANSER and allows control in this way. A similar tool for the 1D SEC can be implemented easily.

3.4 Benchmarks

In this section, I benchmark the 1D and 2D incision and diffusion routines. I compare suitable incision models to the analytical solution of the stream power law. The diffusion routines are benchmarked with an analytical approach for the heating of a half space.

3.4.1 Riverbed incision

The presented SECs simulate riverbed incision with the aid of the stream power law (introduced in Sec. 2.2.1). To benchmark the incision routines, models with stream power exponents $m = n = 1$ are compared to Willett's (1999) analytical solution of the stream power equation. To my knowledge, benchmarks for varying exponents do not exist.

Fig. 3.14(a) presents the 2D benchmark at $200\,ky$. A plane of 200×200 cells of $1\,km \times 1\,km$ width is evolved by DANSERs incision routine and uplifted simultaneously by $u = 5\,\frac{mm}{y}$. Diffusion and lateral incision are switched off, the boundary at $y = 0$ is fixed at $z = 0$, and all other boundaries are closed. The time step is $1\,y$ and the incision coefficient is $\kappa_{rb} = 3 \cdot 10^{-5}$. The 1D incision benchmark is presented by an uplifting line with open fixed boundary at $y = 0$, closed boundary at $y = 200\,km$ and same parameters as the 2D model.

Fig. 3.14(b) compares the 1D incision benchmark and a cross section through the 2D incision benchmark parallel to the y-axis to the analytical steady state solution of Willett:

$$h(x) = -\frac{u \cdot \ln x}{\kappa_{br} \cdot L}$$

with the uplifting plane's length L, the distance from the base level x, and the riverbed elevation $h(x)$.

The numerical 1D and 2D results match the analytical solution.

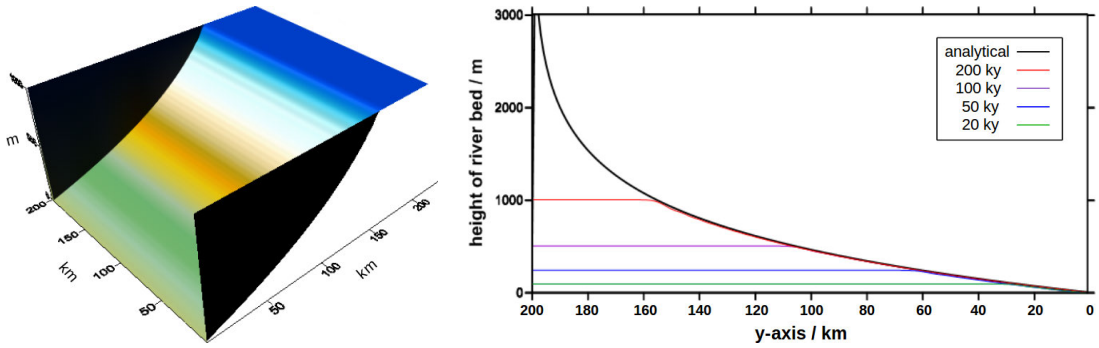

(a) (b)

Figure 3.14: *Incision benchmark for the 1D and 2D SECs. The left figure shows a 2D model of a homogeneously uplifting plane with closed boundaries and stable base level at $x = 0\,km$ after $200\,ky$ of surface evolution. The right figure shows the development of an uplifting 1D plane with closed boundary to the left and fixed boundary to the right. Differently coloured profiles illustrate different time steps. The black profile illustrates the analytical steady state solution of the stream power law. A cross section through the 2D model parallel to the y-axis cannot be distinguished from the red profile.*

3.4.2 Hillslope processes

The presented SECs use linear and nonlinear diffusion to simulate hillslope processes. Linear diffusion (defined in Sec. 2.2.1) is well known from thermal diffusion processes. The heating of a half space is a good model for comparison. Hence, I benchmark the 1D and 2D numerical results of the diffusion routines with the analytical solution.

The analytical solution of the instantaneous heating of a semi-infinite half space (Turcotte and Schubert, 2014, p.155) with time t, distance from origin x, temperature $T(x,t)$, initial temperature $T(x,0) = 0$ and diffusivity κ is

$$T(x,t) = T(0,0) \cdot \left[1 - \mathrm{erf}\left(\frac{x}{2\sqrt{\kappa t}}\right)\right].$$

Substituting the temperature $T(x,t)$ by the height $h(x,t)$ and the thermal diffusivity κ by the diffusivity κ_{hs}, I obtain

$$h(x,t) = h(0,0) \cdot \left[1 - \mathrm{erf}\left(\frac{x}{2\sqrt{\kappa_{hs} t}}\right)\right]$$

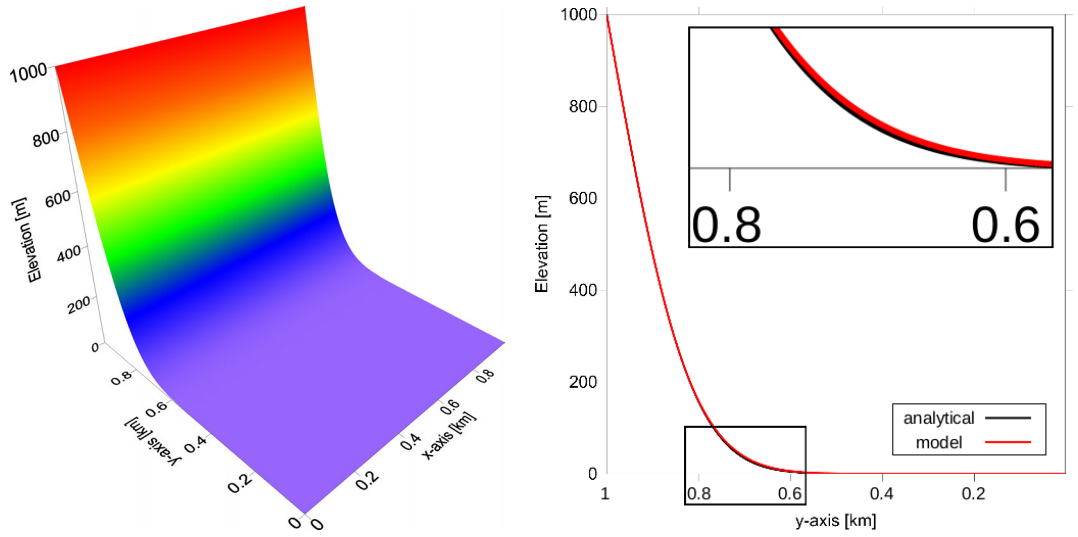

Figure 3.15: *Diffusion benchmark for the 1D and 2D SECs. The left figure shows an initially* $0\,m$ *high plane, which was filled by diffusion from the* $1000\,m$ *high, fixed boundary at* $y = 1\,km$*. The boundaries at* $x = 0\,km$ *and* $x = 1\,km$ *are closed. The right figure shows a cross section through the 2D model parallel to the y-axis. The red profile of a 1D diffusion model with the same setting exactly covers the extracted profile. The black profile shows an approximation to the analytical solution. The framed part of the profile is enlarged in the figure's upper right corner.*

with the Error Function $\mathrm{erf}(x)$, which gets approximated by

$$\mathrm{erf}(x) \approx \frac{2}{\sqrt{\Pi}} \cdot (\sqrt{1 - e^{-x^2}}) \cdot \left[\frac{\sqrt{\Pi}}{2} + \frac{31}{200} e^{-x^2} - \frac{341}{8000} e^{-2x^2} \right].$$

The models in Fig. 3.15 evolved in $4 \cdot 10^4$ steps with a product of diffusivity κ_{hs} and time steps Δt of $\kappa_{hs} \cdot \Delta t = 0.25$. Incision is switched off. The 2D model's resolution is 1000×1000 cells, the 1D model holds 1000 nodes.

The benchmarks of the 1D and 2D diffusion routines match the analytical approximation.

Chapter 4

Applications: The Pamir case

The collision of the Indian and Asian continents formed the Himalaya, as well as the Tien Shan and Pamir. The TIen Shan – PAmir GEodynamic Programme (TIPAGE) focuses on the evolution of the latter orogens. Numerical modelling – as key part of the project – allows to combine the constraints provided by geomorphological data to a consistent picture and to understand the dynamics of the physical processes affecting the evolution of the Pamir – Tien Shan region. Within this project, I focus on the erosion processes in the Pamir and their interaction with lithospheric deformation (Sec. 1 explains the interaction).

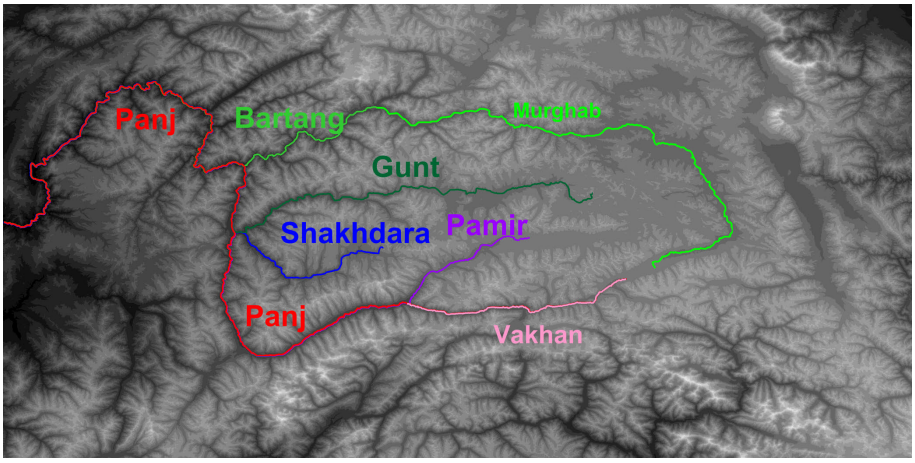

Figure 4.1: *Topographic map of the Pamir orogen with labelled main streams*

Tympel (2014) presents our cooperative 2D modelling results of the erosion's influence on the Pamir's development, simulated by the 1D Surface Evolution Code (SEC, described in Sec. 3.1) coupled with SLIM 2D. In this section, I focus on the advanced 2D SEC "DANSER" (described in Sec. 3.2).

In order to apply a SEC to a certain study region, the modelling result must agree with geomorphological data. This can be achieved by calibrating the model parameters (explained in Sec. 2.2.1). Sec. 4.1 discusses challenges, advances and limits of a detailed calibration with a Digital Elevation Model (DEM) of the Pamir region as initial topography on a time-scale of thousands of years.

Sec. 4.2 addresses the recent evolution of the Panj that is the main river of a powerful drainage network (shown in Fig. 4.1), which transports loads of sediments out of the orogen. Fuchs et al. (2013) interprets the Panj's fragmented profile as a result of multiple river captures along today's riverbed. I assume the captures to be induced by a fault and model the evolution of a channel network in such a system of fault-bounded block rotations.

Finally, Sec. 4.3 reveals first model results of DANSER coupled with the lithospheric-scale thermo-mechanical code SLIM 3D (Popov and Sobolev, 2008) concerning the last 20 My of the Pamir's evolution. Different models illustrate how strongly surface processes may influence the lithosphere's deformation.

4.1 Model calibration on a DEM

Physical and empirical equations give the opportunity to model surface evolution. The adaptation of the equations' parameters to a certain region can be achieved by comparing model results to geomorphological data. I name the adaptation of the model input parameters calibration.

The ambitious aim to calibrate the parameters of a Surface Evolution Model (SEM) to the Pamir orogen is complicated due to the few available data on fluvial incision and hillslope erosion. In order to calibrate the input parameters of the developed code DANSER (described in Sec. 3.2) to today's Pamir on a time scale of thousands of years, I use a Digital Elevation Model (DEM) and constrain model predictions with geomorphological data.

Topographic variations (e.g. altitudes, slopes) cause differing process domains. Whether a fluvial or a glacial model needs to be applied is discussed in Sec. 4.1.1. Sec. 4.1.2 presents the decision between a supply limited model and a transport limited one. The DEM and its modifications for the calibration are described in Sec. 4.1.3. The calibration of the different parameters is shown in Sec. 4.1.4 to 4.1.7. Finally, Sec. 4.1.8 presents the time development of the DEM modelled with the calibrated code in order to validate the calibration result.

4.1.1 Glacial vs. fluvial processes

Above the Equilibrium Line Altitude (ELA) glacial processes predominate incision processes. In the Pamir orogen, the ELA ranges from $4000\,m$ at the margins up to $4800\,m$ above sea level (a.s.l.) at the central plateau (Fuchs et al., 2013). Late Pleistocene glaciers (up to $100\,ka$) are characterized in the eastern Pamir by ELA depressions of 370 to $380\,m$, in the Turkestan Range by ELA depressions of more than $750\,m$, and in the Alay Range by ELA depressions of $600\,m$ (Abramowski et al., 2006). This poses the challenge to model fluvial as well as glacial erosion for higher altitudes.

It has been discussed if glacial erosion is more effective than fluvial incision (e. g. Godard et al., 2012; Norton et al., 2010). Koppes and Montgomery (2009) present global erosion rates in regions of rapid tectonic uplift. Their data indicate that both fluvial and glacial erosion rates are driven by tectonics. They observe cycles in the glacial erosion rates, while fluvial incision rates are stable in a range of 10^1 to $10^7\,y$. These observations question the formerly accepted concept that glacial erosion is more efficient than fluvial incision. As an approximation, I assume that they have the same strength in average.

As the long-term scale variations in the climatic conditions that favour glacial erosion or fluvial incision are not resolvable with geomorphological data, I assume fluvial incision to be the predominant process and apply a stream power model to the entire Pamir.

4.1.2 Supply and transport limited conditions

Pohl et al. (2013) state that the uppermost catchments are characterized by a transport-limited situation. In contrast, the lowermost catchments show a strong hysteresis effect. Especially in spring, which is related to the onset of snowmelt, high water and sediment discharges are transported within the rivers (Pohl and Gloaguen, 2012; Pohl et al., 2015b). This indicates that during spring the main rivers wash away nearly all deposited sediments close by. I interpret this behaviour as a supply-limited system within time scales of more than one year.

Since DANSER is designed for time-scales of thousands to millions of years, the lowermost catchments may be modelled with its supply-limited approach (see Sec. 3.2.5). The impact of the transport limitation in the uppermost catchments are assumed to be negligible.

4.1.3 Digital Elevation Model

A DEM is a matrix of elevation data in a georeferenced coordinate system for projection to the earth's elipsoid. Rather than measuring elevations in the field, providers capture the data with satellites or airplanes. They present DEMs as rasters or triangular irregular grids, the coordinates are usually Cartesian or geographic.

Because of the high quality, I decided to apply the numerical model to the DEM of the Advanced Spaceborne Thermal Emission and Reflection Radiometer (ASTER, Tachikawa et al., 2011). The mentioned DEM consists of elevation data on an equidistant Cartesian grid of $30m$ resolution. I decided to use an extract containing the whole Pamir region, extending from 36° to 39° latitude and from 70° to 76° longitude. The DEM (presented in Fig. 4.1) has more than 22,000 x 11,000 ($= 2.42 \cdot 10^8$) cells of $30\,m$ x $30\,m$ size and covers all the Pamir mountains.

Examples of lower resolution are the GTOPO30 and the DEM of the Shuttle Radar Topography Mission (SRTM, Rodriguez et al., 2006). The GTOPO30 (GTOPO30, 1996) is a free DEM with data fragments from 8 different sources. It covers the whole world, but the quality is not equally good and the resolution of 30 arcseconds (about $1\,km$) is insufficient for my model. The SRTM data provides a DEM of 3 arc-seconds (about $90\,m$) resolution, but it does not cover mountains and deserts and is therefore useless for the purpose of this study.

The DEM builds the basis for DANSER's calibration in Sec. 4.1. The lateral incision parameters' verification in Sec. 4.1.4 is done by checking the modelled water discharge at the DEM. The river profiles in Sec. 4.1.5 are extracted from the DEM. The incision strength and the diffusivity is calibrated while the SEC performs on the DEM (Sec. 4.1.6 and 4.1.7). Finally, the evolution of the calibrated model is tested on the basis of the DEM's development (Sec. 4.1.8).

Resolution of the DEM

The resolution of the topography is an important parameter for the model's calibration. It influences the computed slopes and therefore most of the calibration parameters. When the resolution of a model is modified, many calibration parameters need to be adapted. In order to avoid adapting the calibration parameters to several resolutions, I choose the resolution in advance and calibrate the model afterwards.

The DEM provides a resolution of $30\,m$. To speed up the SEC, I reduce the resolution. I decide for a resolution of $150\,m$ cell size, since this should be enough to resolve even tributaries to the main river Panj. The tool *reduce_resolution*

(detailed description in Sec. A) finds the lowest elevation of the DEM within a $150\,m \times 150\,m$ square around each cell of a new, coarser grid. It stores this value as elevation in the new grid, preserving the channel depth, but underestimating hilltops.

Preservation of the channel depth leads to preservation of the channel slope, whereas the hilltop height defines the hillslope. As the channel slope is most important for the computation of fluvial incision rates and the incision rate is the erosion's driving force, I decided to preserve the river depths rather than the hilltops.

Artefacts and noise in DEM data

A DEM contains noise from satellite (or aeroplane) measurements. In addition, there may be artefacts in steep valleys: Because of the view angle from a satellite to the earth's surface, the satellite may not be able to detect the bottom of the valley. Hence, the elevation of steep valleys such as strongly incised rivers are systematically overestimated.

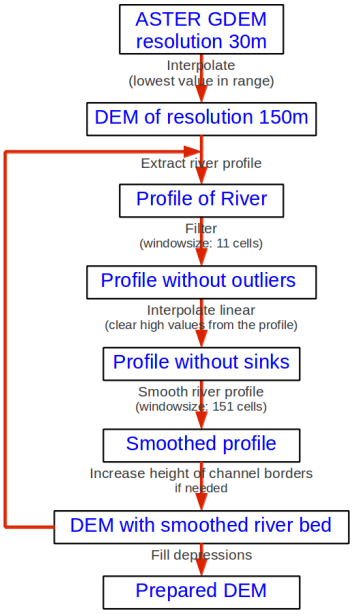

Figure 4.2: *Preparation of a DEM as initial topography for a SEC.*

In order to avoid huge errors in the computed derivatives along a river profile, I pre-process the DEM as depicted in Fig. 4.2. After the interpolation to lower resolution, I use the tool *smooth_riverbed* to prepare the main channels. It identifies a stream from a given starting point via flow directions. Within this stream's

longitudinal profile, it filters outliers above the standard deviation in a moving window of 11 cells along the stream profile. In addition, it corrects elevation values of the chosen river profile that are higher than the elevation of the water-providing cell. These values are interpolated linearly in water flow direction to guarantee a riverbed directed downstream, without any sinks or steps. Afterwards, the tool smooths the resulting monotonic decreasing profile over 151 cells. This long-waved smoothing is needed in order to receive a profile, whose second derivative is smooth enough to avoid oscillating incision and filling during surface evolution. In fact, this long-waved smoothing does not change a concave profile much, but slightly reduces the curvature. To avoid that the river changes its original flow direction and turns back in a roughened one, cells close to the riverbed are elevated infinitesimally above the channel level. I apply this tool to all labelled rivers in Fig. 4.1. Finally, the *filling* routine (Sec. 3.2) completes the DEM preparation procedures, without affecting the prepared channels.

This succession of DEM preparation procedures avoids that the main channels get partly filled because of artefacts in the DEM. Furthermore, the succession guarantees the fastest computation (in lower resolution) without affecting the resulting topography. The plotted river profiles in Sec. 4.1.5 are extracted from the original high resolution DEM and were prepared equally.

4.1.4 Lateral incision

DANSER models riverbed incision and hillslope diffusion. Since it decouples incision from diffusion (described in Sec. 3.2.5), the incision parameters can be scaled independently from the diffusion routine. As soon as the incising processes reproduce geomorphological data, I calibrate the diffusion model that is driven by the calibrated incision routine with river sediment fluxes.

As the routine *spread_water*, which causes lateral incision, only modifies the water discharges, it is not influenced by any other calibration parameter. However, the local incision rate changes with changing discharge distribution. Thus, the calibration parameter κ_{rb} has to be adapted to chosen spreading parameters $c_{\Delta h}$, c_{rad} and S^{lat} (defined in Sec. 3.2.4). Hence, the calibration of the routine *spread_water* is done before choosing κ_{rb}.

Finite channel width

Most of the main rivers in the Pamir orogen, especially the westward flowing part of the Panj river, formed wide valleys (e. g. $3\,km$, compare Fig. 4.4) over hundreds of thousands of years. In some parts, drainage migration causes valleys that are

Figure 4.3: *Channel sections in the Pamir orogen. On the left, the Vanj river is shown. The right photograph presents a section of the northward flowing part of the Panj. Source: Author's pictures, Sep. 2010.*

wider than the streams themselves. Fig. 4.3 shows photographs of such channel sections. The left picture shows a braided section of the Vanj river and the right one shows that the valley of the Panj river is also wider than the stream.

As discussed in Sec. 2.2.2, commonly used methods for the computation of water flow directions are not capable of reflecting the behaviour of migrating channels. Even if hillslope material is allowed to be deposited in the riverbed (softening of the supply-limitation), the stream does not leave its original bed. Consequently, modelled fluvial processes incise channels of exactly one cell width.

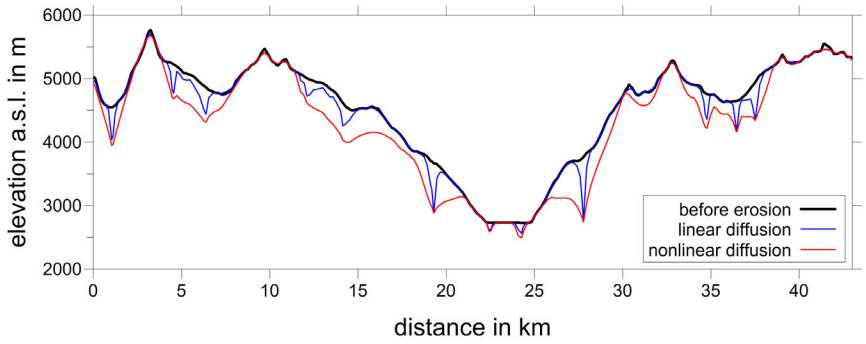

Figure 4.4: *Elevation profile across the Panj river and corresponding drainage divides. The black profile shows the cross section that was extracted from the Pamir DEM. The DEM evolves with varied diffusion mechanisms. The blue profile results from linear diffusion, the red one from nonlinear diffusion.*

Fig. 4.4 shows a cross section through the Panj river (black profile). The blue and red profiles present the same cross section after DANSER evolved the DEM for 50 ky. The profiles demonstrate that neither linear (blue) nor nonlinear diffusion (red) is able to widen the channel. Two parallel channels of one cell width form inside the existing wide river valley, because the diffusion can not reverse the

gradient from a channel cell to one of its hillslope neighbours.

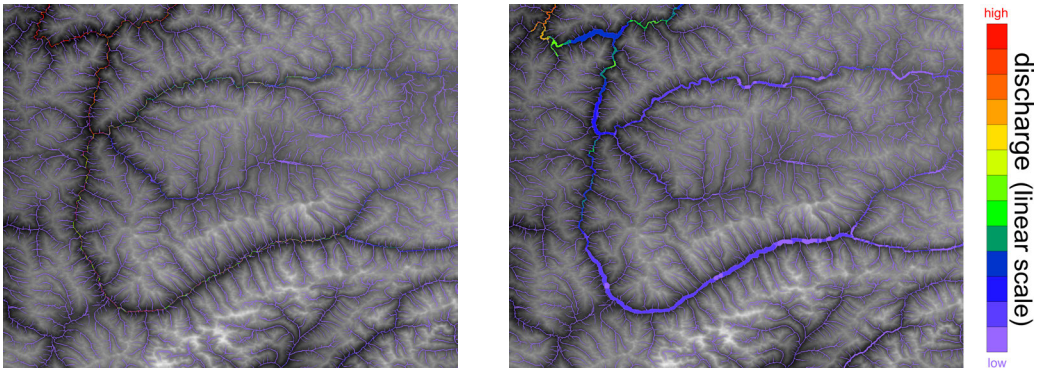

Figure 4.5: *Extract of the DEM with coloured water discharges. Dark grey regions represent low elevations. The figure on the left displays the usual cumulated water discharge, the figure on the right shows the spread water discharge.*

I apply the new lateral incision method, which incises the whole valley width in each time step: The routine *spread_water* (introduced in Sec. 3.2.4) modifies the result of the *water_discharge* algorithm (described in Sec. 3.2.3). It spreads the water discharge over several cells and enlarges the channel width in this way (compare Fig. 4.5). Accordingly, it imitates a migrating channel by incising the entire valley. The resulting cross section after $50\,ky$ of surface evolution with nonlinear diffusion is highlighted in Fig. 4.6.

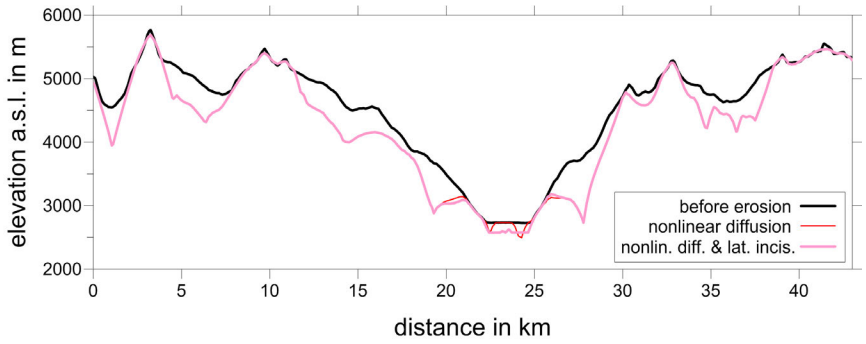

Figure 4.6: *Elevation profile across the Panj river and corresponding drainage divides. The black profile shows the cross section that was extracted from the Pamir DEM. The red profiles are extracted after the DEM evolved with varied incision mechanisms. The difference between the dark and light profile is induced by the lateral incision routine.*

Calibration parameters

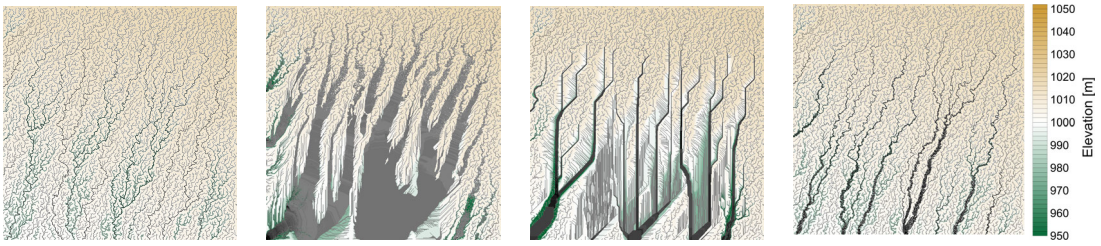

$c_{\Delta h}$ or c_{rad} very low | c_{rad} high, $c_{\Delta h}$ low | $c_{\Delta h}$ high, c_{rad} low | $c_{\Delta h}$ & c_{rad} calibrated

Figure 4.7: *Evolved inclined plane with white noise. The colour scale indicates the elevation a.s.l. in m, the main rivers are marked in grey. The model on the left does not include lateral incision, because of low $c_{\Delta h}$ and c_{rad}. The two centred models show the effect of one high lateral incision parameter in each case ($c_{rad} > 10^{-3}$ and $c_{\Delta h} > 10^{-2}$). For the model to the right, $c_{\Delta h} = 10^{-6}$ and $c_{rad} = 10^{-4}$ are chosen.*

Before calibrating the spreading routine, the influence of its parameters $c_{\Delta h}$ and c_{rad} must be evaluated. Fig. 4.7 illustrates this on the example of an inclined plane with white noise up to $1\,m$ amplitude as start topography after $50\,ky$ of surface evolution. The initial topography starts from $1000\,m$ (lower left edge) and ends at $1020\,m$ elevation (upper right edge). The resolution is 1000×1000 *cells* of $150\,m \times 150\,m$. The incision parameter is set to $\kappa_{rb} = 0.005$ and the diffusion parameter to $\kappa_{hs} = 0.5$. Models with different spreading parameters show that – compared to the topographic noise – low values of $c_{\Delta h}$ or c_{rad} result in effectively no lateral incision. If c_{rad} is high compared to the water discharge (in this case $> 10^{-3}$), the channels get broader and incise larger areas. Higher elevations close by might even split one river into isolated parts. If $c_{\Delta h}$ is high compared to the water discharge and the topographic noise (in this case $> 10^{-2}$), even bigger elevations are considered to belong to the channel and all channels are more or less straight. This leads to parallel drainage patterns in DANSER's preferred flow directions. For $c_{\Delta h} = 10^{-6}$ and $c_{rad} = 10^{-4}$, the model shows a dendritic network with valleys up to $3\,km$ width.

To summarize, high values for c_{rad} lead to large flood-areas. For moderately high c_{rad}, the model is able to reflect the observation of braided streams and deltas. High $c_{\Delta h}$ compared to the topographic roughness should be avoided, since this causes unnaturally straight rivers.

Visual validation

Knowledge about the influence of the lateral incision parameters allows to calibrate the spreading routine to a DEM.

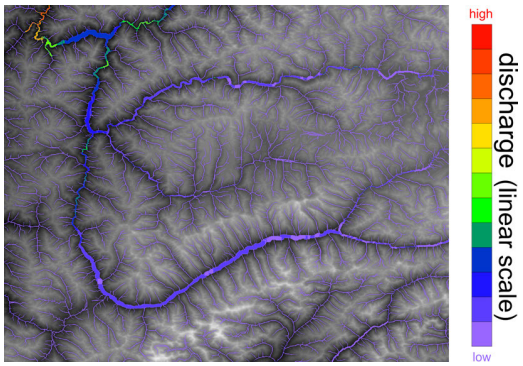

Figure 4.8: *Map extract of the Pamir DEM with calibrated spread water discharge. The colour represent the local water discharge, dark grey regions indicate low elevations.*

On a DEM, one can observe the areas that are influenced by fluvial incision. Incised areas are more flat than hillslopes and mostly surrounded by steep slopes. This opens up the opportunity to visually validate the result of the *spread_water* routine. For the described DEM (Sec. 4.1.3), the spreading slope $S^{lat} = 0.2$, the incision radius coefficient $c_{rad} = 10^{-4}$, and the lateral incision height coefficient $c_{\Delta h} = 10^{-6}$ offer a convincing result (Fig. 4.8).

4.1.5 Stream power exponents

This section explains the calibration of the stream power law (2.5) exponents. In order to evaluate their ratio $\theta := \frac{m}{n}$, I focus on stream profile analysis (Sec. 2.2.1 explains the theory) of the Pamir's main rivers.

The assumption for stream profile analysis is that the chosen stream is in erosional equilibrium. The erosional equilibrium (also called steady state) is reached when the incision rate compensates the vertical uplift rate in each location of the stream. I assume erosional equilibrium in the Pamir's main rivers. Whether this assumption is justified, is discussed in the following paragraphs.

In case of steady state, the logarithmic slope plotted against the logarithmic catchment area along a river, approaches a linear graph. The gradient of this graph is, according to stream profile analysis, the ratio $-\frac{m}{n}$. The following longitudinal stream profiles (joined in Fig. 4.9) and log-log plots are extracted from the

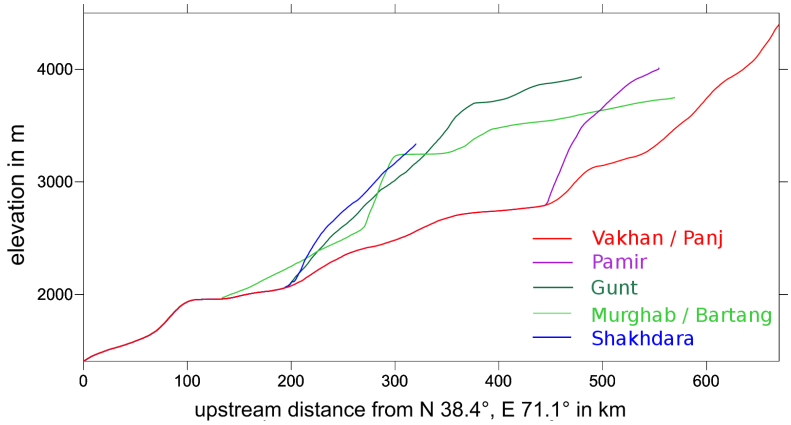

Figure 4.9: *Profiles along the main rivers in the Pamir orogen, extracted from the Pamir DEM.*

Pamir DEM (described in Sec. 4.1.3) by the *river_profile_analysis* tool (explained in Sec. A).

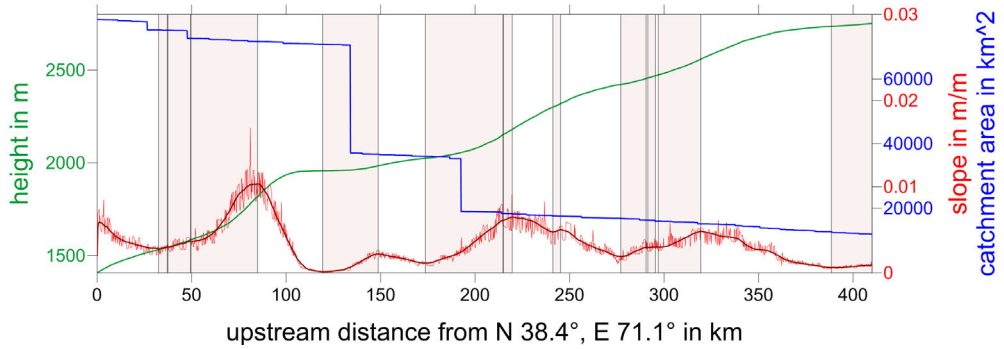

Figure 4.10: *Profile along the* Panj *river in green. The catchment area along the river is plotted in blue, the slope (tangent of the angle) in light red, the smoothed slope in dark red. Selected profile parts that are identified as concave are marked with shaded background.*

Fig. 4.10 shows the longitudinal profile of the Panj river, the matching catchment area, and the slope. In Fig. 4.11, its slope is plotted against its catchment area. Huge data gaps indicate where a tributary flows into the channel. The stream profile analysis of the Panj river does not lead to a concavity index θ that is valid for the entire river. The best fit among the concave profile parts has a gradient of $\theta = 7.6$, which appears to be unrealistically high (see Sec. 2.2.1 for values of θ). Looking at Panj's longitudinal profile in more detail reveals fragmentation. Fuchs et al. (2013) rule out erodibility variations caused by different rock types, catchment geometry and climatic reasons for this fragmentation. They suggest

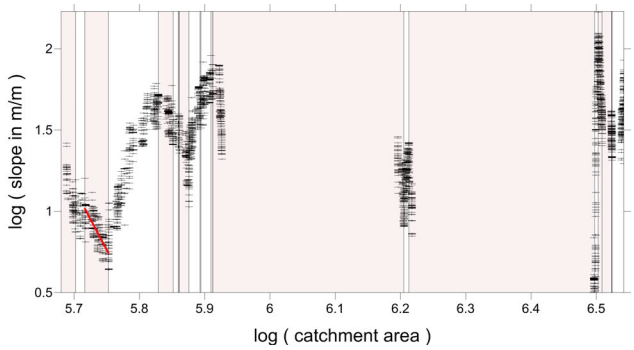

Figure 4.11: *Log-log plot of slope against catchment area along the* Panj *river. Black crosses mark data points. A computed best-fit line is drawn in red. The background of some concave profile parts are shaded as in Fig. 4.10.*

that three different base levels shaped Panj's profile. These different base levels may indicate three river capturing events along today's Panj river. They calculate $\theta = 0.43$, $m = 0.3$ and $n = 0.7$ (R. Gloaguen, personal communication, April 23, 2015). Their hypothesis about the negligible influence of rock erodibility motivates Sec. 4.2.4.

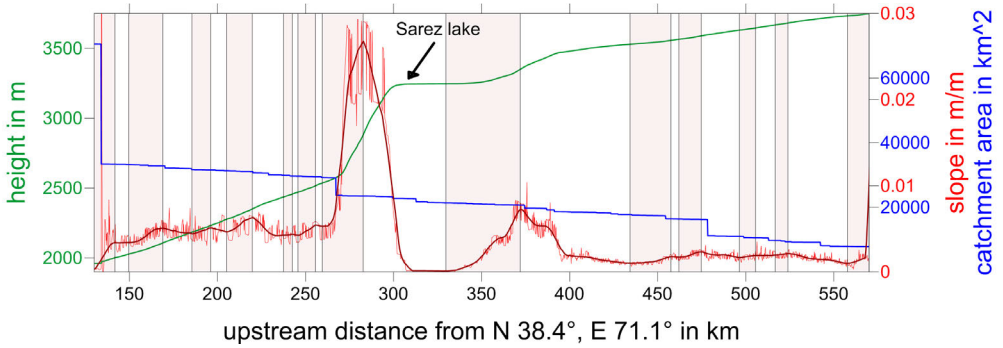

Figure 4.12: *Profiles along the* Murgab and Bartang *rivers in green. The catchment area along the rivers is plotted in blue, the slope (tangent of the angle) in light red, the smoothed slope in dark red. Selected profile parts that are identified as concave are marked with shaded background. The black arrow indicate the location of the Sarez lake.*

An earthquake-induced landslide completely blocked the valley of the Murgab river in the winter of 1911 (Schuster and Alford, 2004). Then, the Sarez Lake begun to flood the upstream area at about 3250 m above sea level. A short way downstream of that lake, the Murgab river empties into the Bartang river. The longitudinal profile of the connected rivers (Fig. 4.12) is governed by the natural dam, 300 km upstream of the reference coordinate $N\,38.4°$, $E\,71.1°$ at the DEM's boundary

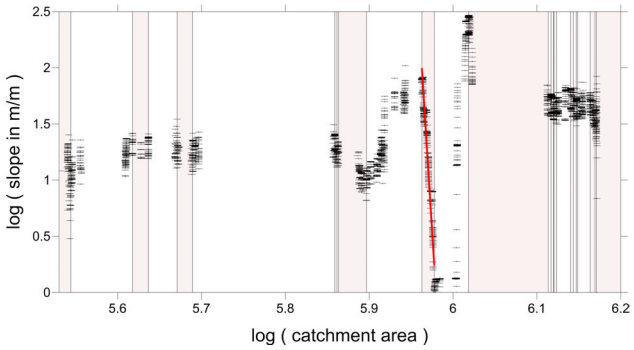

Figure 4.13: *Log-log plot of slope against catchment area along the* Murgab and Bartang *rivers. Black crosses mark data points. A computed best-fit line is drawn in red. The background of selected profile parts are shaded as in Fig. 4.12.*

(marked as Sarez Lake). The profile part from 330 km to 370 km leads to the red best fit line in the log-log plot (Fig. 4.13). Unfortunately, the gradient of the best fit is $\theta = 118$. Whipple and Tucker (1999) argue that such high values rule out an equilibrated river. Other long concave profile parts could not be identified.

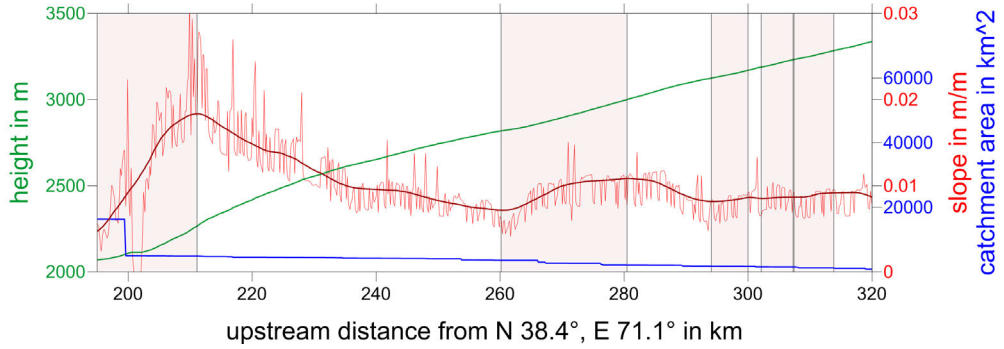

Figure 4.14: *Longitudinal profile of the* Shakhdara *river in green. The catchment area along the river is plotted in blue, the slope (tangent of the angle) in light red, the smoothed slope in dark red. Selected profile parts that are identified as concave are marked with shaded background.*

The Shakhdara river flows at the surface of the Shakhdara dome, a Cenozoic gneiss dome (Stübner et al., 2013a). The river profile in Fig. 4.14 and the log-log plot in Fig. 4.15 make it obvious that river profile analysis is not applicable for this river. If the convex part from 210 to 260 km was in equilibrium, this would result from a tectonic uplift, which is increasing downstream (Kirby and Whipple, 2001). This theory is unlikely, because Stübner et al. (2013b) suggest that the Shakhdara dome's uplift stopped at about 2 Ma. The concavity index $\theta = 0.87$ of the concave section from 260 to 280 km may indicate a disequilibrated part of the profile.

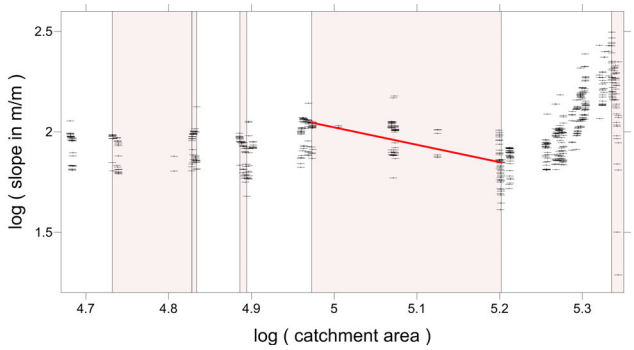

Figure 4.15: *Log-log plot of slope against catchment area along the* Shakhdara *river. Black crosses mark data points. A computed best-fit line is drawn in red. The background of selected profile parts are shaded as in Fig. 4.14.*

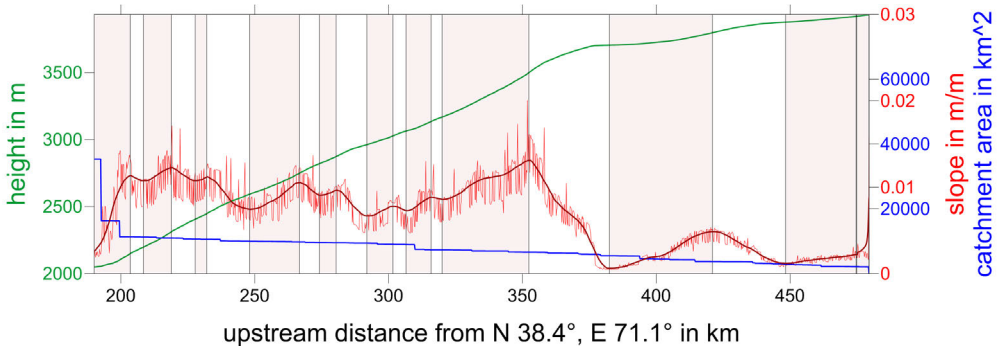

Figure 4.16: *Longitudinal profile of the* Gunt *river in green. The catchment area along the river is plotted in blue, the slope (tangent of the angle) in light red, the smoothed slope in dark red. Selected profile parts that are identified as concave are marked with shaded background.*

The Gunt's profile (Fig. 4.16) shows a similar convex part as the Shakhdara does. Fig. 4.9 highlights that both profiles are almost identical, even though the Gunt river flows at the boundary of the Shakhdara dome, while the Shakhdara river flows in the centre of the dome. If the dome was still active, this would induce different uplift patterns along the two rivers. The river profiles' similarity supports the suggestion of a sudden base level drop, induced by a recent river capturing event (Fuchs et al., 2013) downstream of the mouth of both rivers. Further upstream, the Gunt has two knickpoints at 375 km and at 425 km. The concave parts close to those knickpoints lead to concavity indices ranging from $\theta = 1.3$ to 4.9. Such high values indicate disequilibrium conditions as well.

Fig. 4.18 shows the longitudinal profile of the Pamir river. Because of its convex shape Fuchs et al. (2013) suggest that this might indicate an ongoing capture.

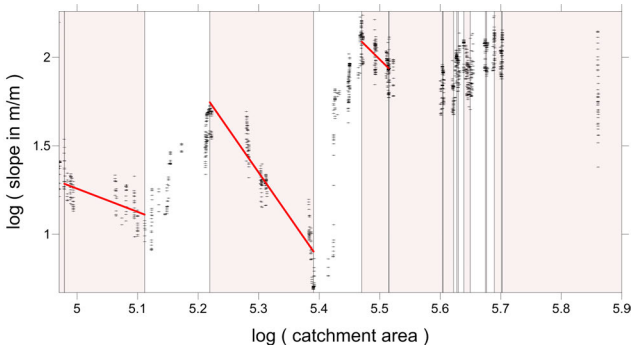

Figure 4.17: *Log-log plot of slope against catchment area along the* Gunt *river. Black crosses mark data points. Some computed best-fit lines are drawn in red. The background of selected profile parts are shaded as in Fig. 4.16.*

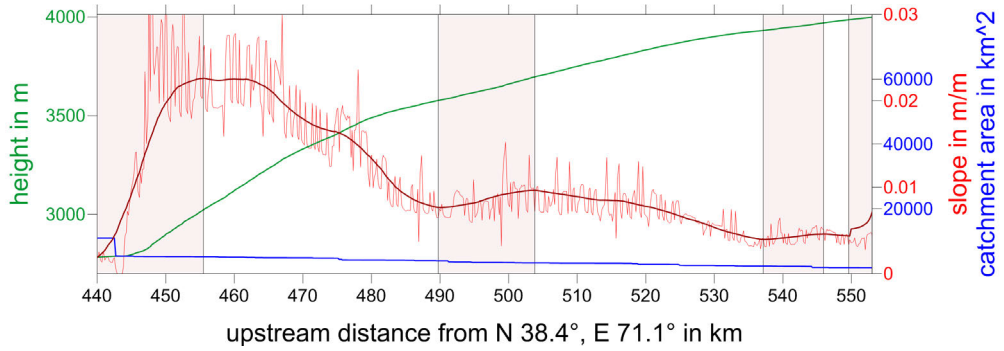

Figure 4.18: *Longitudinal profile of the* Pamir *river in green. The catchment area along the river is plotted in blue, the slope (tangent of the angle) in light red, the smoothed slope in dark red. Selected profile parts that are identified as concave are marked with shaded background.*

Sec. 4.2.6 presents a capturing model, which develops such a convex river profile.

The highest river I study is the Vakhan. Since the tracked profile (Fig. 4.19) starts at 4500 m a.s.l., the upper part of the profile might be influenced by glacial processes (compare Sec. 4.1.1). Neglecting the region downstream of the knickpoint at 480 km, stream profile analysis (Fig. 4.20) produces the local concavity index $\theta \approx 0.6$ at 4000 m a.s.l. as well as a reasonable best fit gradient $\theta \approx 0.4$ for the entire river. The obvious concave profile and the range of the computed concavity indices indicate a steady state profile.

To summarize, stream profile analysis gives little reasonable concavity indices for the Pamir orogen's main rivers. As pointed out in Sec. 4.1.3, the DEM-recording satellite might have been partly not able to detect the bottom of a narrow gorge within a broader valley. It is possible that the described DEM preparation did not

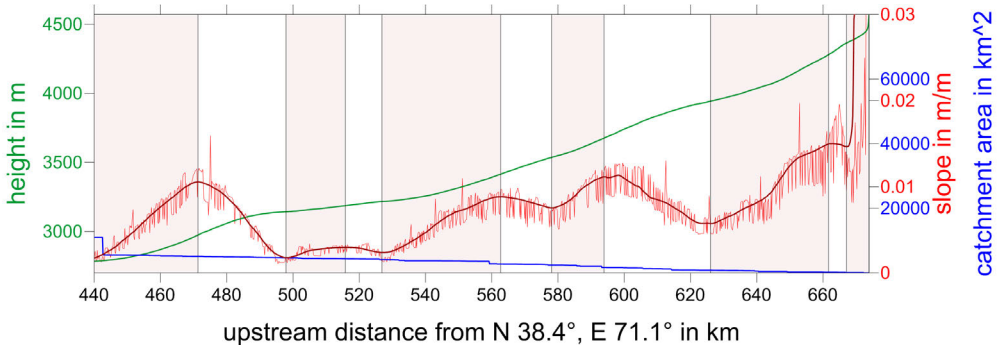

Figure 4.19: *Longitudinal profile of the* Vakhan *river in green. The catchment area along the river is plotted in blue, the slope (tangent of the angle) in light red, the smoothed slope in dark red. Selected profile parts that are identified as concave are marked with shaded background.*

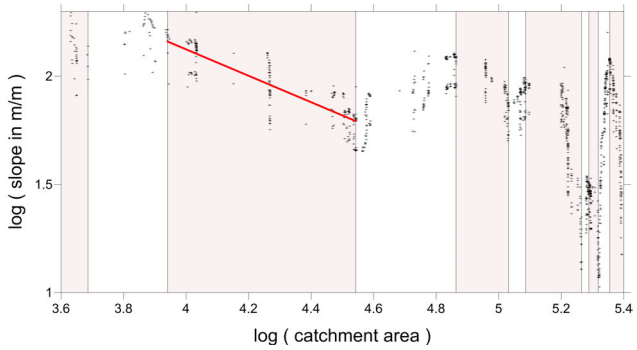

Figure 4.20: *Log-log plot of slope against catchment area of the* Vakhan *river. Black crosses mark data points. A computed best-fit line is drawn in red. The background of selected profile parts are shaded as in Fig. 4.19.*

eliminate all those artefacts. This might have lead to partly wrong river profiles. Otherwise, the sparse reasonable concavity indices hint at a transient landscape with unequilibrated river profiles. One reason for the disequilibrium conditions could be recent glacial influence. The Shakhdara's and Gunt's u-shaped valley (K. Stübner, personal communication, June 04, 2015) may indicate that fluvial incision very recently displaced glacial erosion. I do not follow this hypothesis in the scope of this study, but assume the transient landscape to be caused by a reorganizing river network and several river capturing events that lead to sudden base level drops in the captured rivers, while only minor influence is attributed to climate change and erodibility variations (Fuchs et al., 2013, see Sec. 4.2.4 for models about the influence of erodibility on river capturing events).

The longitudinal profiles of the Gunt, the Shakhdara, the Pamir and the Panj

river seem to be mainly shaped by capturing events. This motivates a model of the evolution of longitudinal river profiles during capturing events (Sec. 4.2.6). The profile of the connected Bartang and Murghab rivers is governed by the natural dam that embeds the Sarez lake. This dam makes it difficult to interpret the profile. The obviously concave Vakhan's river profile has a concavity index $\theta \approx 0.4$, which is within the range of commonly used scaling values. This hints at equilibrium conditions.

The only reasonable concavity index that was evaluated in this study is $\theta \approx 0.4$. As Fuchs et al. (2013) computes a similar concavity index ($\theta \approx 0.43$) and stream power exponents $m = 0.3$ and $n = 0.7$ for the dissected Panj, I decide to adopt these stream power exponents for the entire Pamir.

4.1.6 Stream power coefficient

The numerical discretisation of the stream power law (3.12) involves the calibration parameter κ_{rb}. In order to adjust this parameter, reference fluvial incision rates are required.

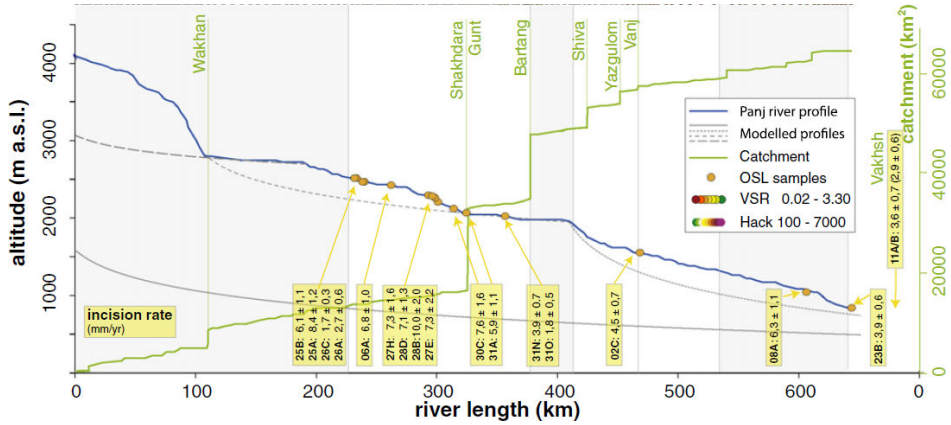

Figure 4.21: *River profile (blue) of the Panj river with marked sediment sampling points (yellow dots) and the evaluated incision rates. The catchment area along the profile is drawn in green. Source: Fuchs et al. (2014).*

Fuchs et al. (2014) sampled fluvial terrace sediments along the Panj river. On the base of the Optically Stimulated Luminescence (OSL) method, they estimate terrace ages. Kinematic GPS measurements give the elevation difference from the terrace to today's riverbed. With the aid of these two values they calculate averaged incision rates in the last 500 to 23000 y. Fig. 4.21 presents the highly variable rate of incision along the Panj from 1.7 mm/y to 10.0 mm/y. Variations

are explained by spatial incision rate variations rather than temporal variations, since incision rates indicate stability over time for terraces in proximity of each other but differing age.

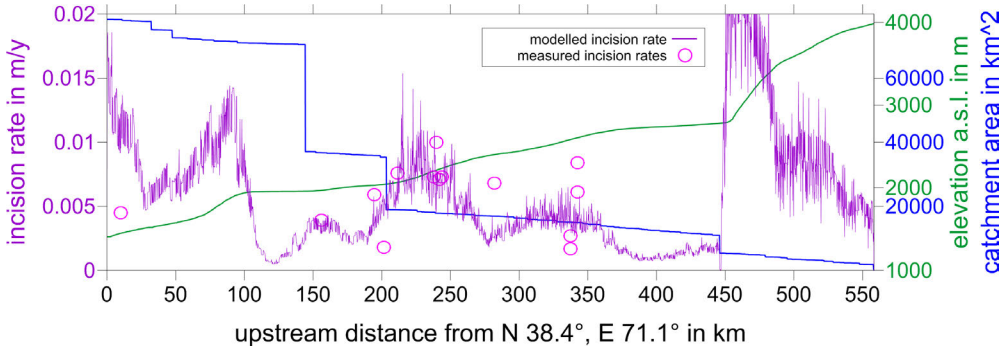

Figure 4.22: *Calibrated modelled incision rates ($\kappa_{rb} = 1.7 \cdot 10^{-3}$) along the* Panj *river in purple. Magenta circles mark in situ incision rates. The green profile illustrates the channel elevation and the blue one the drainage area.*

The stream power coefficient that produces the modelled incision rates matching the in situ rates best can be identified by varying κ_{rb} and comparing both rates visually. The *river_profile_analysis* tool (described in Sec. A) extracts the incision rates along the Panj river for a given stream power coefficient. Fig. 4.22 shows the resulting plot for $\kappa_{rb} = 1.7 \cdot 10^{-3}$ combined with measured incision rates. Since the modelled incision rates match the geomorphological data's range, I adopt this coefficient for further calibration steps.

4.1.7 Diffusivity

Once the incision model is calibrated, the diffusivity κ_{hs} needs to be adapted. Hillslope erosion rates and suspended sediment yields provide reference values for the calibration.

Suspended sediment transport

Sedimentary discharges along the Pamir's main rivers reveal further insights into present-day hillslope erosion rates. With sediment yields across specified channel sections, hillslope diffusion can be calibrated to short time scales.

Pohl et al. (2015a) present historical suspended sediment yields from April to August averaged over less than five years, which are shown in Fig. 4.23. Pohl et al. (2013) state that most of the sediment transport occurs during the summer. Hence,

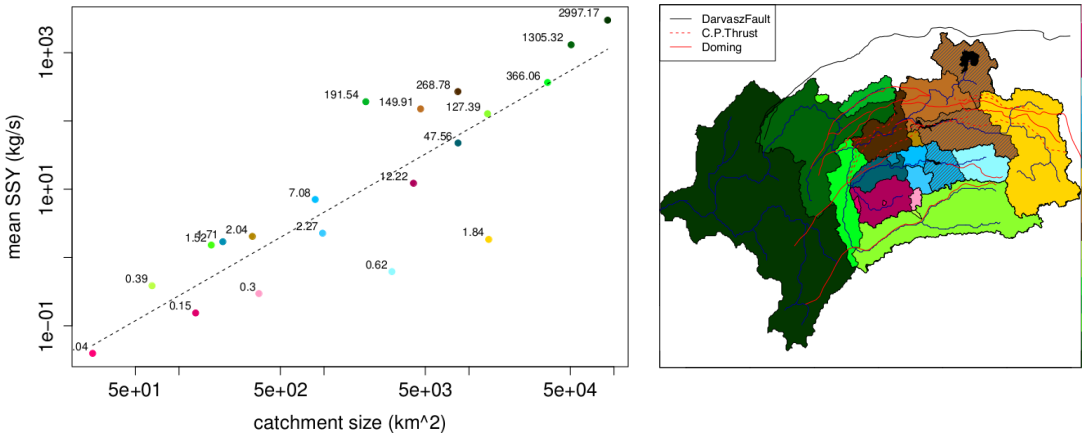

Figure 4.23: *Suspended sediment yield in the Pamir's river network. On the left, the averaged sediment yield from several years from April to August in kg/s is plotted against the catchment size. The colour of the dots marks the catchment regions that are plotted at the figure on the right. Source: Pohl et al. (2015a)*

I approximate the annual sediment yield by multiplying the averaged monthly sediment yield (taken from Fig. 4.23) with $6\,months/year$. In order to compare the measured sediment yield to the models' sedimentary discharge, the adjusted data is plotted in Fig. 4.24.

The available data on river sediment yields focus on suspended load, while the contribution from bedload remains unresolved. To my knowledge, studies about the Pamir river's bedload do not exist. Thus, I assume resembling proportion of suspended sediment yield to bedload as in the Himalaya. Galy and France-Lanord (2001) estimate the total Himalayas' sediment flux to be twice the measured flux of the suspended load. This shows that the bedload in the Pamir orogen's rivers might be not negligible.

Hillslope erosion rates

Hillslope erosion rates offer further details about the sediment transport of the Pamir's rivers. Fuchs et al. (2015) use cosmogenic Beryllium-10 concentrations in fluvial sediments to calculate basin-wide erosion rates. They derive erosion rates of 0.05 to $0.16\,mm/y$ at the Pamir plateau and 0.54 to $1.45\,mm/y$ at the margins in averaging intervals smaller than $1000\,y$. For the entire Pamir, they compute averaged erosion rates of about $0.64\,mm/y$. This value is used to validate the computed suspended sediment yield.

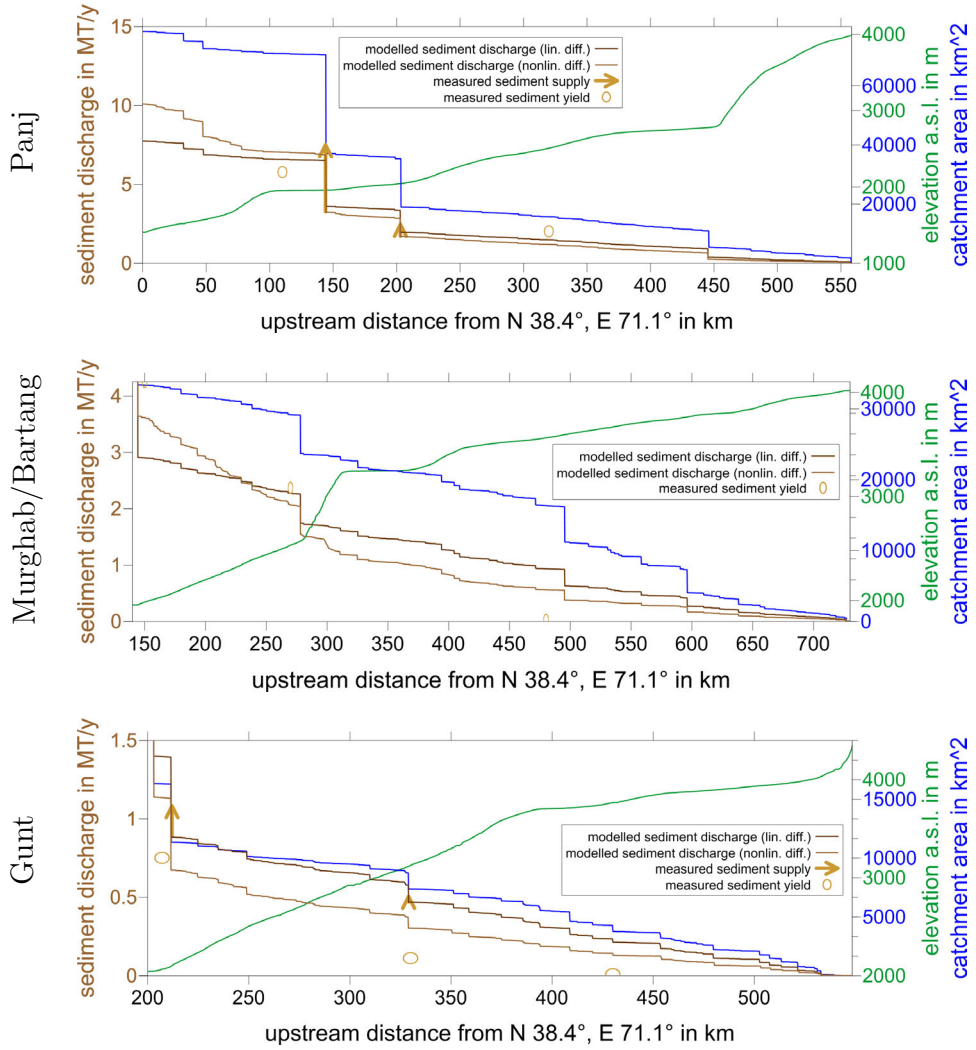

Figure 4.24: *Sediment discharges along the Panj, Murghab/Bartang and Gunt rivers. Golden circles mark the measured suspended sediment yield and the length of the golden arrows symbolizes the measured suspended sediment supply. Modelled sediment discharge for linear diffusion ($\kappa_{hs} = 0.27$) is plotted in dark brown, for nonlinear diffusion ($S_c = 1$, $\kappa_{hs} = 0.15$) in light brown. The green profile illustrates the channel elevation and the blue one the catchment area.*

Erosion rates vs. sediment yield

I compare the erosion rates to the suspended sediment yield at two measuring points. For that purpose, I multiply the erosion rate with the sediment density

$2\,t/m^3$ and the upstream catchment area from each suspended sediment yield measuring point. This results in a total sediment discharge of $84 \cdot 10^6\,t/y$ at one of the measuring points and $13 \cdot 10^6\,t/y$ at the other one. The first value is about 14 times higher, the second value about 6 times higher than the measured suspended sediment yield. Potential reasons are that the geomorphological erosion rates did not capture major mass wasting, that the suspended load measures did not capture the sediment yield peaks, that the erosion rates are overestimated due to the unknown contribution of sediments from glaciers, that the sediment transport in winter is not negligible, that the erosion rates dramatically decreased within the last thousand years, or that the Panj's bedload is much higher than the measured suspended sediment yield.

Because of the apparent mismatch between sediment yield measures and erosion rates, I decide to design two models. One model is based on the assumption of negligible bedload and the other one assumes the total sediment yield to be ten times as high as the suspended sediment yield. Accordingly, I pick two values for the diffusivity: one time and ten times the suspended sediment flux. I assume the total sediment flux to be within the range of one of these values.

Calibration

Surface evolution on a DEM reduces significantly the influence of artefacts (compare Sec. 4.1.3) on the diffusion rate. Thus, I decide to match the diffusivity to the suspended sediment yield after running DANSER on the DEM for $1\,000\,y$. The tool *stream_profile_analysis* (see Sec. A for further description) accumulates all sediments that result from hillslope processes along the channel. I compare the measured sediment yields to the modelled sediment discharge for different diffusivities κ_{hs} and choose the appropriate one.

Fig. 4.24 illustrates the modelled sediment discharge, which is calibrated to the measured suspended sediment yield along the Panj river. The calibrated linear diffusivity is $\kappa_{hs} = 0.27$. A model with critical gradient $S_c = 1$ leads to $\kappa_{hs} = 0.15$. The measured sediment yield in the Murghab and Bartang rivers is approached by the same diffusivities. However, the modelled nonlinear sediment discharge of the Gunt river overestimates the measured sediment yield by about 100 %, calibrated linear diffusion overestimates the sediment yield by even more than 100 %. In order to adapt the diffusivity to the measured sediment yield in all marked measuring points one by one, the linear diffusivity varies between $\kappa_{hs} = 0.07$ and 0.4 and the nonlinear diffusivity with the critical gradient $S_c = 1$ varies between $\kappa_{hs} = 0.05$ and 0.25. This large variation of diffusivities (a factor of five) emphasizes the imprecision of this calibration.

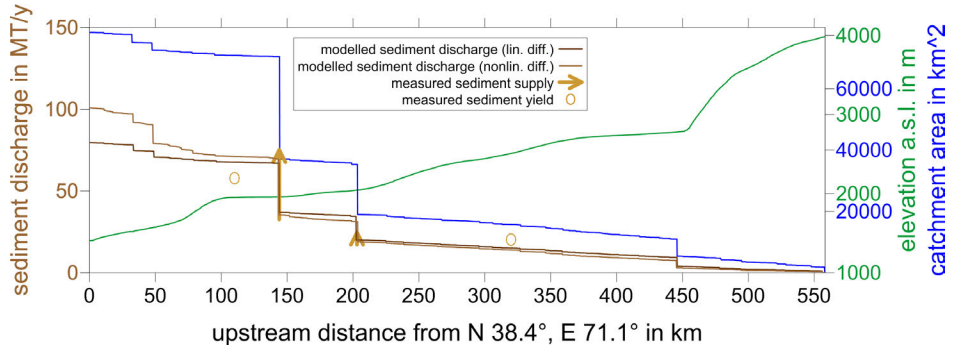

Figure 4.25: *Sediment discharge along the* Panj *river. Golden circles mark ten times the measured suspended sediment yield and the length of the golden arrows symbolizes ten times the measured suspended sediment supply. Modelled sediment discharge for linear diffusion ($\kappa_{hs} = 2.7$) is plotted in dark brown, for nonlinear diffusion ($S_c = 1$, $\kappa_{hs} = 1.7$) in light brown. The green profile illustrates the channel elevation and the blue one the catchment area.*

Calibrating the diffusion model to ten times the suspended sediment yield (Fig. 4.25) results in the linear diffusivity $\kappa_{hs} = 2.7$ and in the nonlinear diffusivity $\kappa_{hs} = 1.7$.

In summary, a detailed calibration of hillslope diffusion to the suspended sediment yield on a Pamir DEM can only be achieved with locally variable diffusivity. A calibration with locally constant diffusivity leads to more than two times over- or underestimation of geomorphological erosion rates. The following section discusses models with both diffusivities.

4.1.8 Calibration result

In order to validate the calibration parameters, DANSER evolves the Pamir DEM $50\,ky$. This chapter discusses the calibration results.

Fluvial incision

Fig. 4.26 highlights the calibrated incision rates ($\kappa_{rb} = 1.7 \cdot 10^{-3}$) on the Pamir DEM. The model cannot exactly reproduce the geomorphological incision rates along the Panj river (compare to Fig. 4.21), but achieves a reasonable order of magnitude. The incision rates in the tributaries reach up to almost $20\,mm/y$. Such high incision rates have not yet been observed. However, some channel segments in the Pamir region might be incised that strongly over short periods of time because of a highly unstable river network. Another reason for these high incision rates

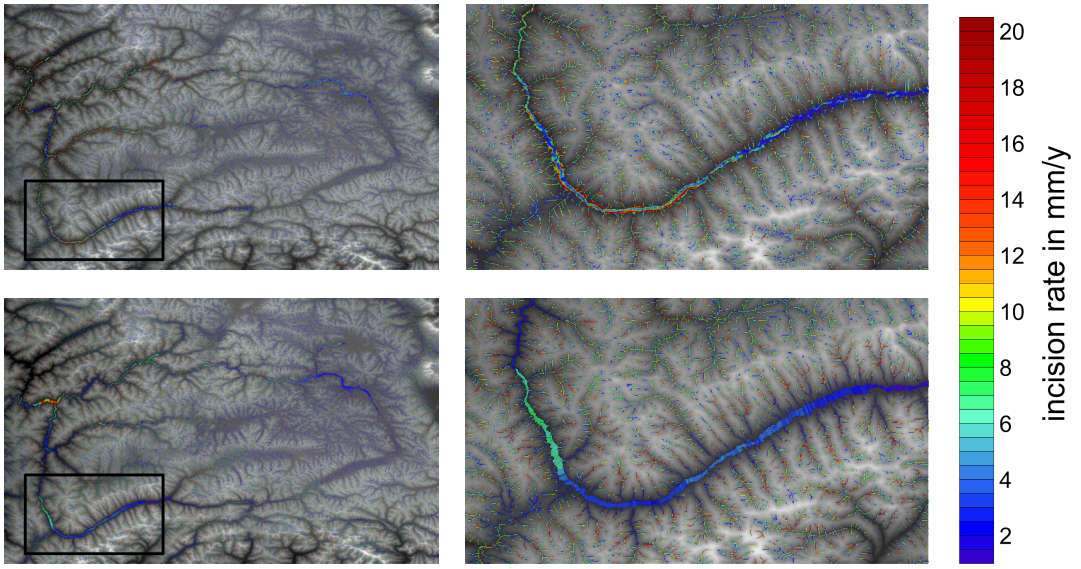

Figure 4.26: *Development of the calibrated incision rates on a Pamir orogen's DEM. The figures on top present the incision rate at* $1\,ky$*, the figures on bottom illustrate the incision rate at* $50\,ky$*. The left figures show the entire DEM and the right ones enlarge the framed region. Lower elevations are painted in darker grey.*

in the tributaries may be the imposed supply-limitation. Pohl et al. (2013) state the uppermost catchments to be transport-limited (see Sec. 4.1.2). The settled sediment prevents the bedrock underneath from weathering. In contrast to this observation, DANSER removes all the river sediments immediately and incises the uncovered riverbed. This may lead to higher incision rates than the observed ones.

The strongly incised channel segment in the framed region in Fig. 4.26 marks a deep, narrow canyon. This channel developed very recently. A stronger incision rate is therefore very likely. The incision rate peak further downstream is an upstream migrating knickpoint that was caused by the model boundary. However, this does not affect the calibration.

The evolution of the model shows that the channel width is preserved over time and the incision rate is smoothed spatially over time. This demonstrates that the incision time step $\Delta t = 100\,y$ is chosen small enough and highlights the benefit of *lateral incision*.

Hillslope diffusion

Fig. 4.27 illustrates the development of the linear diffusion rates in two different models. The model in the upper part of the figure assumes negligible bedload in the main rivers, the model in the lower part assumes ten times higher bedload transport than suspended load transport.

In all models, sedimentation strongly decreases with time, because they do not involve spatially heterogeneous uplift, the only mechanism that could increase concavities outside of the riverbeds.

At $1000\,y$, the models show hilltop erosion rates of up to $2\,mm/y$ (negligible bedload) and $20\,mm/y$ (high bedload). While the erosion near hilltops decreases, the erosion close to incised regions strongly increases over time. Calibrating the model to ten times the suspended sediment yield reduces this phenomenon, but cannot fully stabilize the erosion rates.

Similar to linear diffusion, nonlinear diffusion strongly increases the erosion rate with time (Fig. 4.28). However, the nonlinear diffusion model ($S_c = 1$) shows a less homogeneous pattern than linear diffusion. The erosion on hillslopes strongly increases, while the erosion on hilltops is nearly zero. This model highlights the slope dependence of nonlinear diffusion.

All evaluated diffusivities induce a diffusion rate that is strongly increasing with time. This effect is reduced by increasing the diffusivity. This hints at much higher erosion rates (and much higher diffusivity) than the measured ones or a transient landscape as suggested by Fuchs et al. (2015). A transient landscape might be effected e. g. by the suggested river captures or by recent glacial influence.

Technical reasons for the increasing diffusion rate might be the inappropriateness of linear as well as nonlinear diffusion for models employing DEMs, the inappropriateness of a supply-limited model for the Pamir orogen, or the importance of the rock erodibility's distribution along the model's topography.

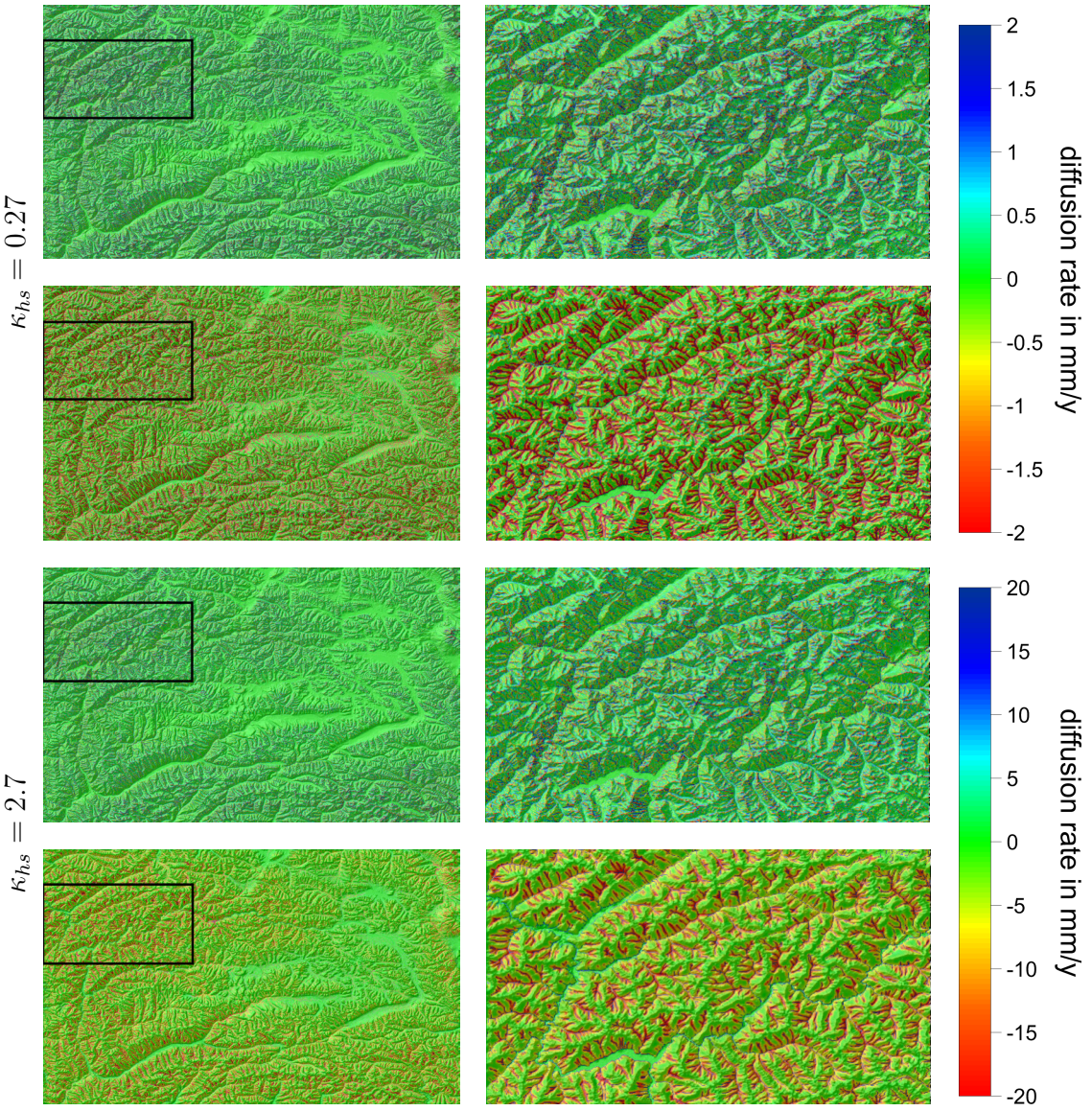

Figure 4.27: *Development of linear hillslope diffusion rates on a Pamir DEM. The diffusivity is $\kappa_{hs} = 0.27$ in the models shown in the four pictures on top and $\kappa_{hs} = 2.7$ in the models shown in the four pictures on bottom. Within each four figures, the figures on top show the diffusion rates at $1\,ky$ and the figures on bottom illustrate the diffusion rates at $50\,ky$. The left figures present the entire DEM and the right ones enlarge the framed region. Red regions are eroded, blue spots receive sediments from the surrounding area.*

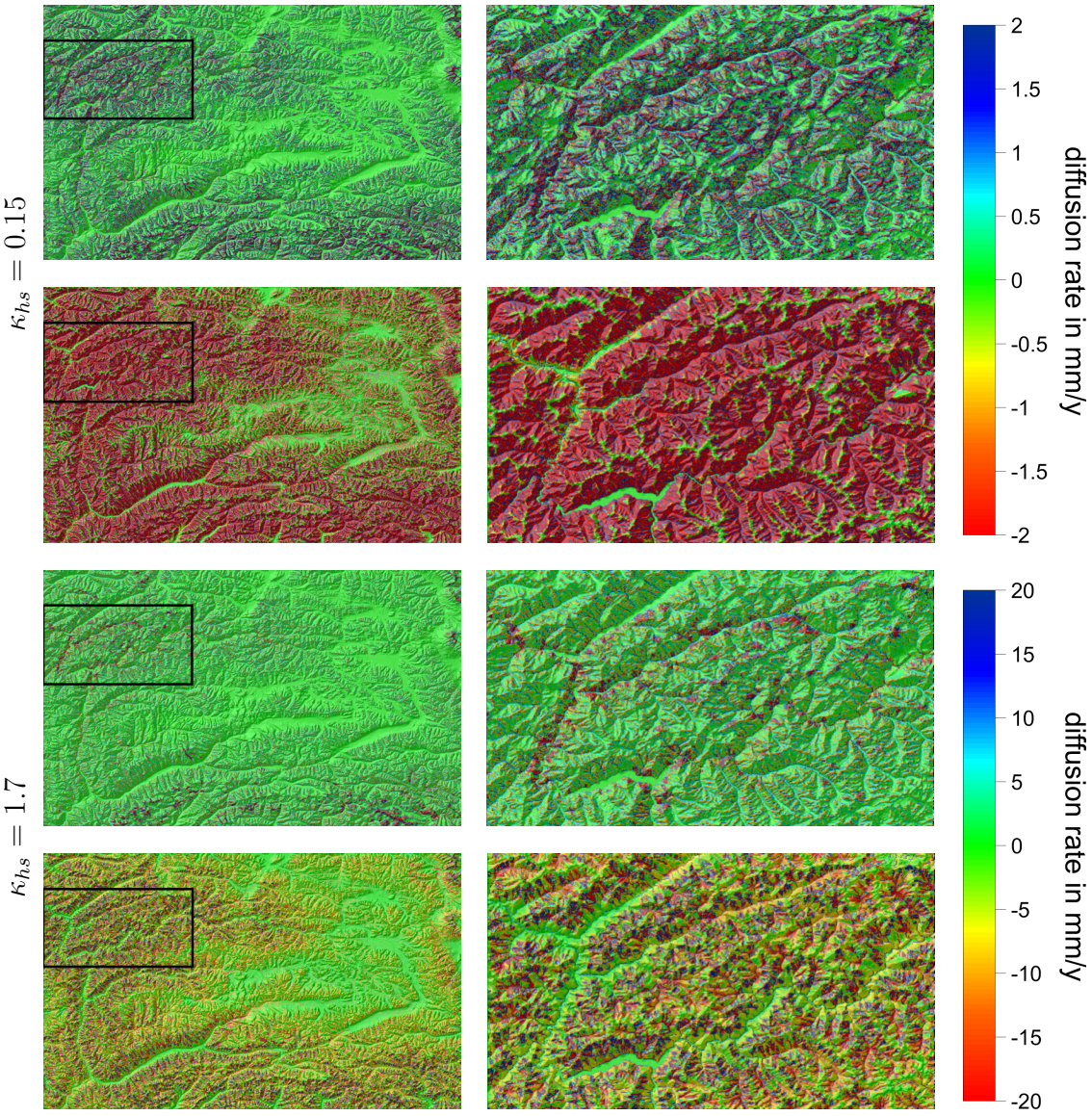

Figure 4.28: *Development of nonlinear hillslope diffusion rates on a Pamir DEM. The diffusivity is* $\kappa_{hs} = 0.15$ *in the models shown in the four pictures on top and* $\kappa_{hs} = 1.7$ *in the models shown in the four pictures on bottom. Within each four figures, the figures on top show the diffusion rates at* $1\,ky$ *and the figures on bottom illustrate the diffusion rates at* $50\,ky$*. The left figures present the entire DEM and the right ones enlarge the framed region. Red regions are eroded, blue spots receive sediments from the surrounding area.*

I have been able to calibrate the model parameters to the geomorphological properties of the Pamir successfully.

Lateral incision pushes the code development further in applying SECs to DEMs. It preserves the existing valley width, reflects the range of incision rates on a Pamir DEM, stabilizes the range of incision rates over time and smooths spatially the incision rates with time steps of $100\,y$.

However, there are still open questions concerning the applicability of the diffusion equation to DEMs. Whether diffusion is able to reflect geomorphological data should be investigated in an orogen where erosion rates tend to balance the local uplift. Regions with high erodibility variations, or unstable drainage network should be avoided. Furthermore, reliable geomorphological data are essential. The DEM's development will reveal if changes to the diffusion equation are required for the calibration to a DEM.

4.2 Simulation of fault-bounded block rotations

The highly active Pamir orogen is penetrated by sub-parallel faults. The main rivers flow from east to south-west, following this fault system (see Fig. 4.29). They join the river Panj that abruptly turns at 71.5° longitude from south-west direction north. At the sudden turn a south-westward directed valley starts. Belousov (1976) investigate sediment terraces along the Panj river. North of the old riverbed, he observed a terrace that dips from north to south against today's river flow direction. He interprets this as north-south dipping uplift of the terrace, but today's dip could also be caused by a recent change of the river flow direction. A plausible explanation for that change is a drop of the river base level that triggered a spontaneous upstream river capturing event (Gloaguen et al., 2014; Fuchs et al., 2013) taking away most of the water discharge from the valley that starts at 71.5° longitude.

There is not yet evidence how strong the impact of a fault system, such as the one observed in the Pamir orogen, on a river network is. Is it possible that a fault system forces the rivers in its direction? May a forming fault induce a sudden river capturing event?

This numerical study aims to clarify if and how a system of faults may influence the development of a river network. Beforehand, Sec. 4.2.1 explains the model setup and Sec. 4.2.2 highlights the importance of the new lateral incision routine for the simulation of river capturing events. Then, I discuss for which configurations a deflection of the river is possible (Sec. 4.2.3). The influence of uplift and high erodibility zones on the deviation of river networks are compared in Sec. 4.2.4.

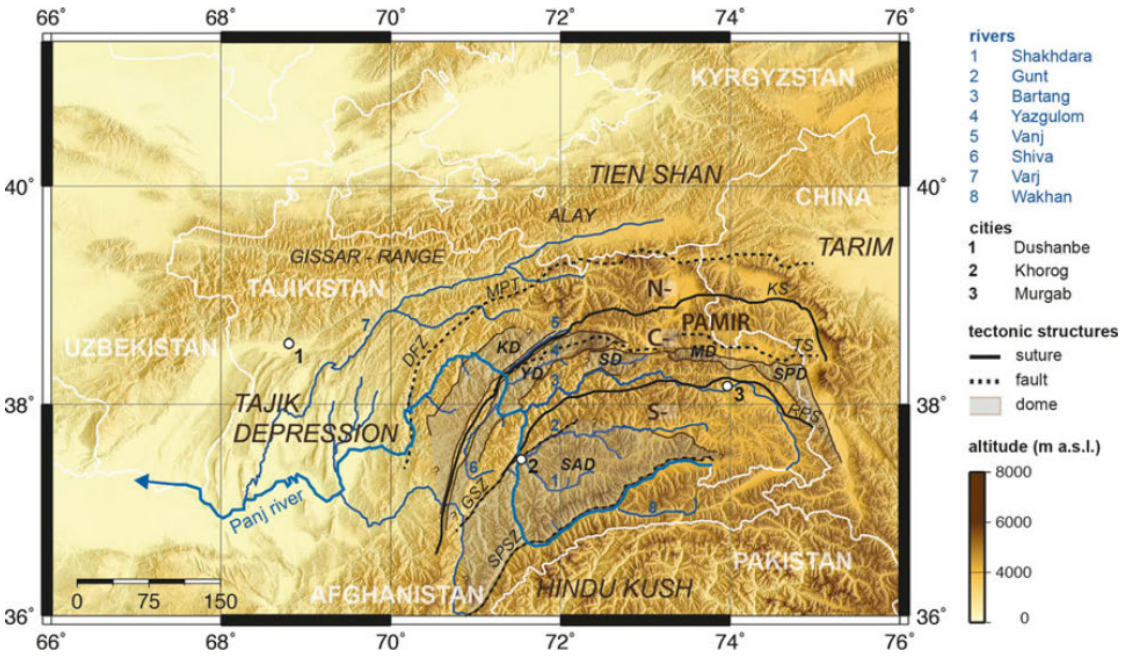

Figure 4.29: *Map of the Pamir region with labelled main streams and faults. This map shows that many rivers' direction are aligned parallel to the fault system. From Fuchs et al. (2013)*

Sec. 4.2.5 presents simulations that demonstrate the effect of varying angles between riverbed and fault on river flow direction. Finally, Sec. 4.2.6 reveals the longitudinal profiles' development of captured rivers.

4.2.1 The model setup

I study fault-bounded block rotations that are modelled as regions of increased erodibility and analytically imposed uplift.

Table 4.1: *Parameters of the inclined plane as initial topography*

Model size	$150\,km$ x $150\,km$
Cell size	$150\,m$ x $150\,m$
Initial elevation	5000 - $5020\,m$
White noise amplitude	$1\,m$
Fault locations (y-coord)	15, 45, 75, 105, $135\,km$
Fault width	$1\,km$

The initial topography is an inclined plane with added white noise (Table 4.1 lists

its parameters). DANSER (explained in Sec. 3.2) evolves this plane for $1\,My$. The main flow direction of the forming rivers is determined by the direction of inclination. Fig. 4.30 depicts an example of the topography at $0.5\,My$. Red lines mark high erodibility zones along the dip-slip faults, which are arranged from east to west (w.l.o.g) and start to evolve at $0.5\,My$. Fig. 4.31 illustrates the uplift distribution in north-south direction. I neglect isostatic rebound, since a rebound effect is assumed to be negligible at this length- and time-scale.

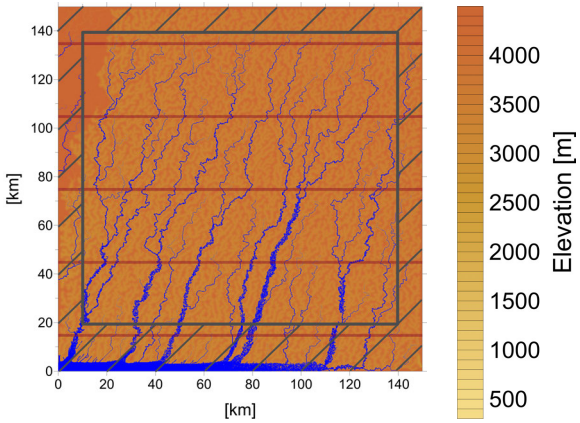

Figure 4.30: *Example of a model before the faults start to evolve. The inclined plane with white noise evolved for* $0.5\,My$. *The main rivers are plotted in blue. Dark red lines mark the regions that will develop as high erodibility zones along the faults. The grey box frames the map extract that is shown in Sec. 4.2.3 to 4.2.5*

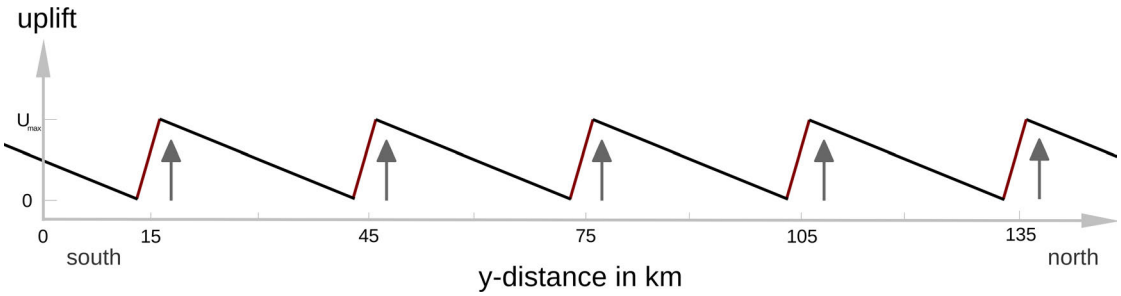

Figure 4.31: *Analytically imposed uplift from south to north. The uplift in east-west direction is constant. Dark red lines mark high erodibility zones. The maximum uplift* U_{max} *varies in the following models.*

Table 4.2 gives an overview of the computed models. The calibration parameters $S^{lat} = 0.2$, $c_{rad} = 10^{-4}$, $c_{\Delta h} = 10^{-6}$ of the lateral incision and the stream power

Table 4.2: *Model parameters*

Model	Fig. 4.7	Fig. 4.32	Fig. 4.33	Fig. 4.34	Fig. 4.35	Fig. 4.37
Incision parameter	0.005	0.005	varies	0.005	0.005	0.005
Diffusion parameter	0.5	0.5	0.5	0.5	0.5	0.5
Factor for lateral incision radius	varies	0 - 10^{-4}	10^{-4}	10^{-4}	10^{-4}	10^{-4}
Factor for lateral incision height	varies	0 - 10^{-6}	10^{-6}	10^{-6}	10^{-6}	10^{-6}
Angle between riverbed and faults	70°	70°	70°	70°	45 - 80°	70°
Erodibility factor (fault)	1	1 - 10	100	1 - 100	100	100
Max. uplift rate	$0\frac{mm}{y}$	0 - $1\frac{mm}{y}$	$1\frac{mm}{y}$	$10\frac{mm}{y}$	$1\frac{mm}{y}$	0 - $10\frac{mm}{y}$

exponents $m = 0.3$, $n = 0.7$ are adopted from Sec. 4.1.4 and 4.1.5. The diffusivity $\kappa_{hs} = 0.5$ is chosen within the proposed interval in Sec. 4.1.7. The uplift rates are based on the range of vertical exhumation rates.

4.2.2 River capturing in orogen-scale resolution

Fig. 4.29 reveals the influence of the Pamir's fault system on its river network. A common SEC with channel initiation function is not able to simulate such a river network's response to tectonic processes in a resolution lower than about $10\,m$ (see Sec. 2.2.2 for more details).

Fig. 4.32 compares four models. All figures display the described inclined plane after $50\,ky$ of surface evolution computed by DANSER. The incision parameter is set to $\kappa_{rb} = 0.005$ and the diffusion parameter to $\kappa_{hs} = 0.5$. In the models on the right, fault-bounded block rotations are added. The lower models include calibrated lateral incision (see Sec. 4.1.4 for calibration).

Without lateral incision, the fault system only slightly changes the river network over time. In contrast, the influence of the fault system on a model with lateral incision is clearly visible: Some channels are deflected from their original flow direction and aligned with a fault. This clearly shows that *lateral incision* enables river capturing for orogen-scale resolution models with channel initiation function. Thus, the following models in Sec. 4.2.3 to 4.2.6 include calibrated lateral incision.

4.2.3 Proportion of uplift and incision rate

One of the controlling factors for river capturing is the ratio of uplift and incision rate. This section discusses for which ratios river capturing is possible.

I adopt geomorphological uplift rates of the Pamir. Uplifting domes cover the western part of the Pamir region (Stübner et al., 2013a). Stübner et al. (2013b) evaluate vertical footwall exhumation rates of 1-3 mm/y for these domes averaged from 18-15 Ma to 2 Ma. As the probability of river capturing is dependent on the

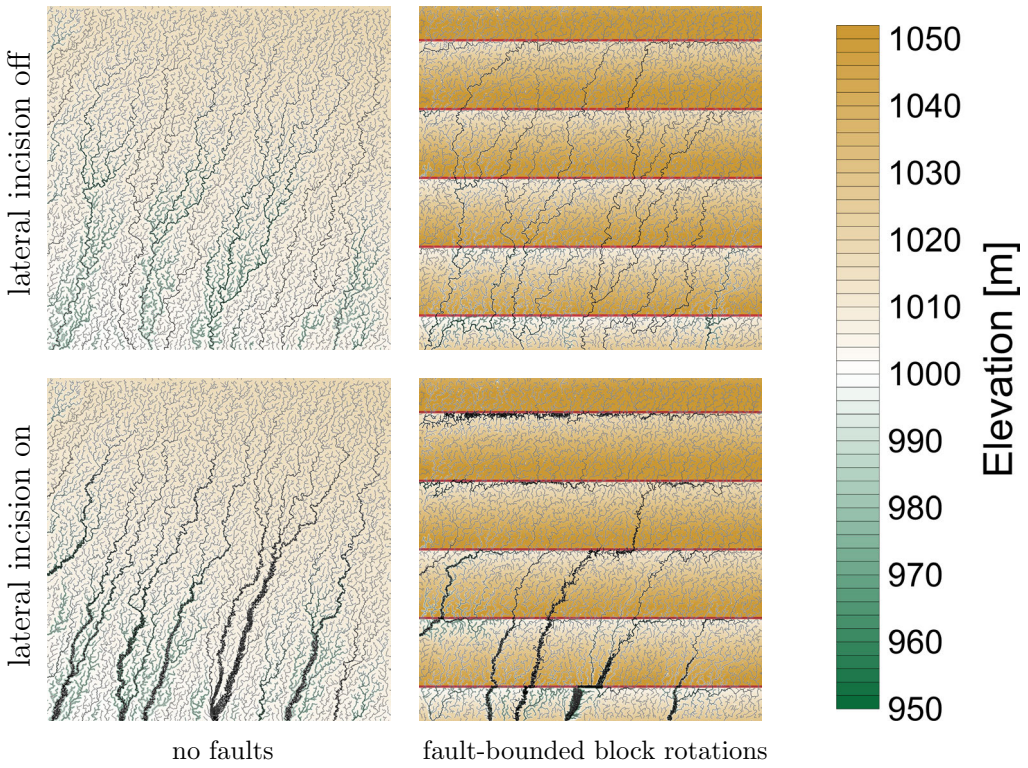

Figure 4.32: *Inclined plane with white noise after* 50 *ky of surface evolution. The colour scale represents the elevation a.s.l., the river system is marked in grey. In the right column, five fault-bounded block rotations with an uplift up to* $1\,mm/y$ *(see Fig. 4.31 for distribution of uplift rates) and* 10 *times increased erodibility in the faults (marked in red) are modelled at the plane. Upper row: Lateral incision is off. Bottom row: Lateral incision is switched on.*

proportion of uplift and incision rate rather than the uplift rate itself, I adopt the lower observed vertical dome exhumation rates up to $1\,mm/y$ and vary the ratio by varying the stream power.

Fig. 4.33 shows the centre of fault-bounded block rotation models (the setup is described in Sec. 4.2.1). The plane evolves $0.5\,My$ before the faults with a hundred times increased erodibility start to evolve. For $\kappa_{rb} \leq 0.003$, the incision rate is so low compared to the uplift that it takes the river network more than $0.5\,My$ to start the adaptation to the fault system. For $\kappa_{rb} = 0.005$, the channel of the highest water discharge within a fault captured all rivers. The stronger the incision gets, the quicker is the reorganization of the rivers. Even channels with low water discharge start to capture streams. Finally, for $0.02 < \kappa_{rb} < 0.05$, the tectonic

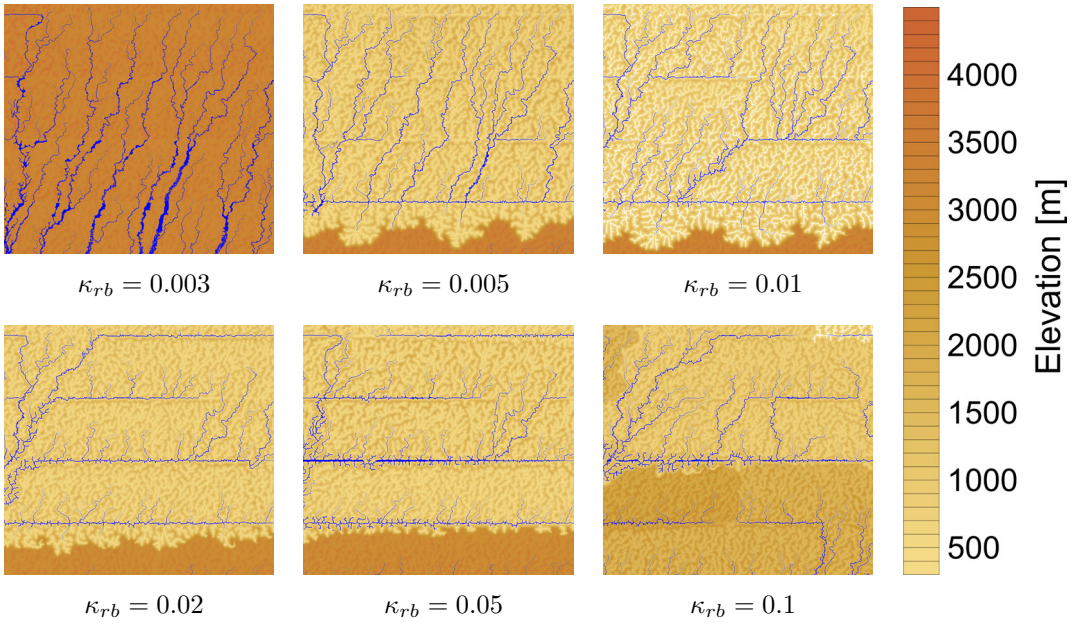

Figure 4.33: *Extract of fault-bounded block rotation models at* $1\,My$*. The colour scale labels the elevation a.s.l., the main rivers are marked in blue. From left to right, the stream power coefficient increases from* $\kappa_{rb} = 0.003$ *up to* 0.1*.*

uplift forces all main channels into faults in little more than $0.5\,My$. Stronger incision (e.g $\kappa_{rb} = 0.1$) leads to less capturings in the model because the tectonic uplifting force is nearly compensated by the stream power.

In the Pamir orogen, the river network is partly influenced by the fault system similar to Fig. 4.33, $\kappa_{rb} = 0.005$. Hence, I adopt this stream power coefficient for further models.

4.2.4 Influence of high erodibility zones on a developing river system

The material inside of a fault is strongly deformed. Particularly at the surface, the mechanical force produces fractures and increases the erodibility by rupturing the material. How does such an increased erodibility affect the probability of river capturing events? To answer that question, this section compares the influence of uplift to the influence of high erodibility zones.

Fig. 4.34 shows fault-bounded block rotation models with varying uplift rate and different erodibilities within the faults. The models show a strong influence of the

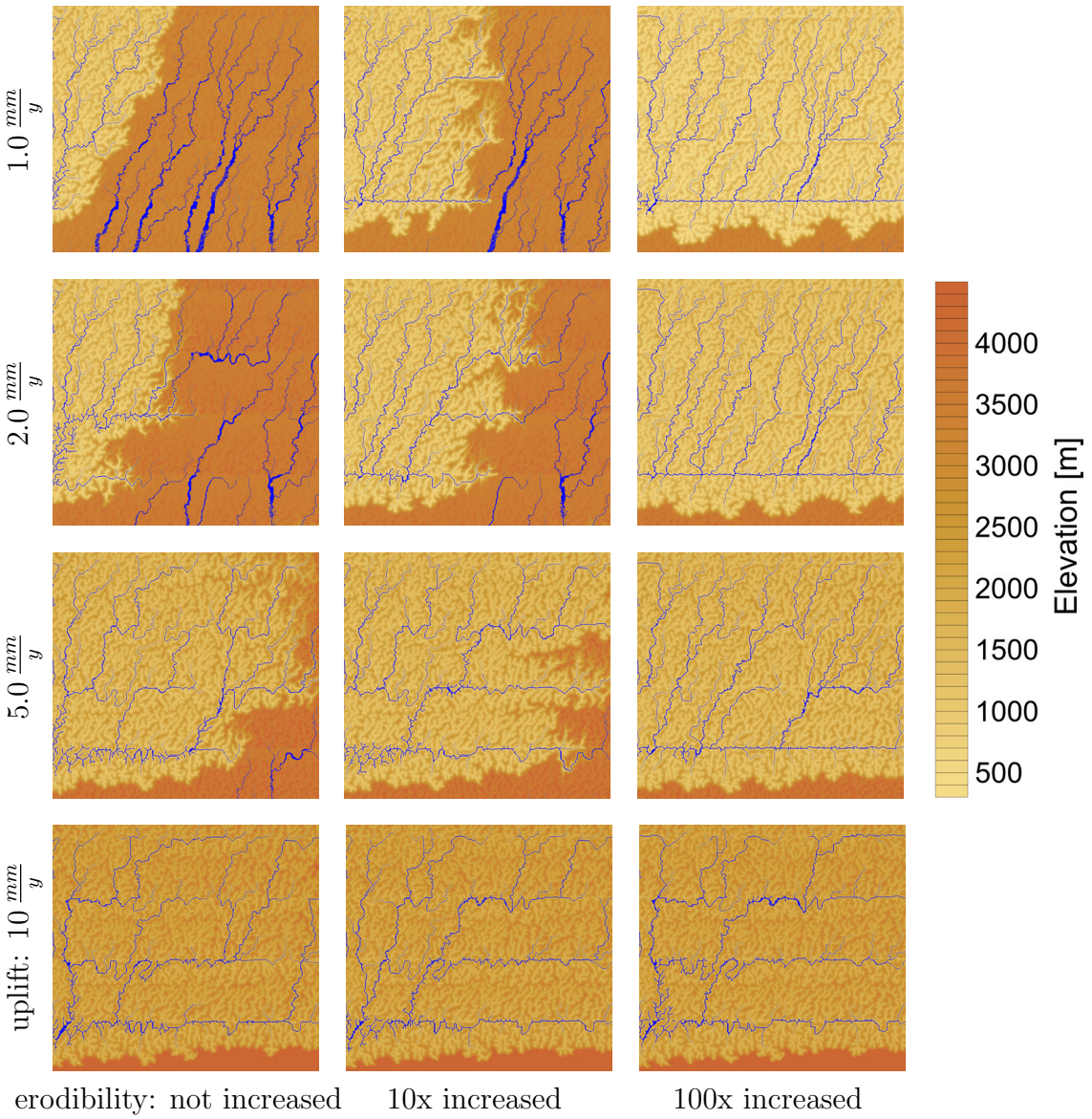

Figure 4.34: *Fault-bounded block rotation models with different uplift rates and different erodibilities inside the faults. The colour scale represents the elevation a.s.l, the main rivers are marked in blue. From top to bottom, the uplift rate increases, from left to right the erodibility increases.*

uplift rate on the probability of capturing events. In contrast, high erodibility zones do not influence the number of capturing streams, but speed up the headward erosion along the fault and hence the capturing process of the stream. It is remarkable that rivers are captured even without increased erodibility. The high

uplift gradient within the faults induces river captures on its own.

4.2.5 Influence of the angle between riverbeds and faults on a developing river system

To study the influence of the angle between faults and channels on the probability of capturings, I adopt the parameters of the second model in Fig. 4.33. The maximum uplift rate is $1\,mm/y$ and the erodibility of the material in the faults is a hundred times increased.

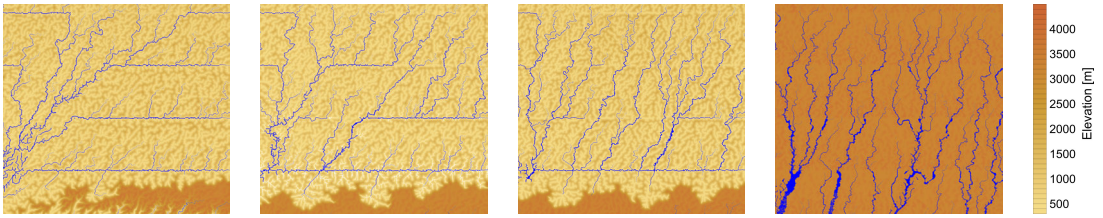

50° 60° 70° 80°

Figure 4.35: *Fault-bounded block rotation models with varying angle between faults and channels. The colour scale labels the elevations a.s.l., the main rivers are marked in blue. From left to right, the angle between faults and riverbeds varies from* 50° *to* 80°.

With the given uplift-incision relation, the models in Fig. 4.35 present the importance of the deflection angle. For an angle of 50°, the model shows the highest probability of a river capturing. The higher the angle, the less captures happen. Finally at 80°, the topography does not indicate any capturing events within $1\,My$.

The results suggest that river capturing, induced by dip-slip faults, is highly sensitive to the angle between a riverbed and the fault. Only very strong uplift rates may lead to river capturing with a deflection angle of more than 80°, as assumed for the Panj river.

4.2.6 Development of a captured river's profile

This section addresses a captured channel's evolution along a fault. I present a model with two river capturing events in sequence, as they could have happened in the Panj river.

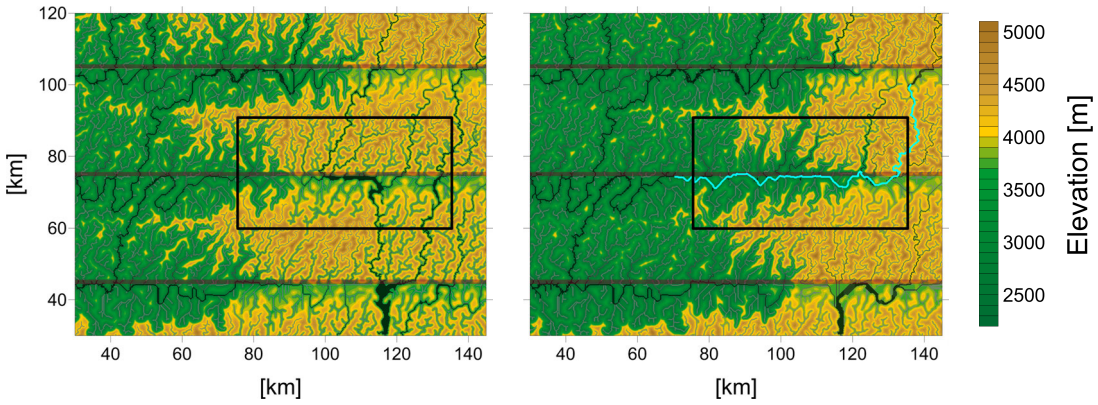

Figure 4.36: *Map extracts of a fault-bounded block rotation model before and after a double-capturing event. The left map shows the model at* 730 *ky, the right one at* 780 *ky. The faults are marked in red. The river network is drawn in dark grey. The black box frames the region that is enlarged in Fig. 4.37. The cyan line marks the river pathway after the captures, whose longitudinal profile is plotted in Fig. 4.38.*

Fig. 4.36 presents the model of interest before and after the two capturings. The maximum uplift rate is 10 mm/y. The erodibility in the faults is 100 times increased. The framed region is extracted in Fig. 4.37. It reveals how fast the modelled capturing events happen. In less than 1 ky, tributaries of more than 25 km (first capture) and 5 km length (second capture) invert their flow direction and become main rivers.

Fig. 4.38 shows the longitudinal profile's evolution of the new riverbed. The tilted channel profile from 100 to 120 km distance result from the linear tectonic uplift rate. This profile gets strongly incised because of the steep slope. The elevation drop leads to headward erosion up the drainage divide at 95 km distance and finally to the first capturing event at 230 ky. A fast development of the reversing river profile from 65 to 95 km distance starts: A convex channel profile develops. The convexity migrates upstream until it reaches the tributary and the hillslope that divides it from another tributary of a north-south flowing main stream. Because of the sudden base level drop the second water divide at 53 km distance gets strongly eroded and finally turns into a channel. This induces the second capture along the tributary from 43 to 53 km distance. Similar to the first capturing event, a knickpoint migrates upstream as a convexity in the longitudinal channel profile.

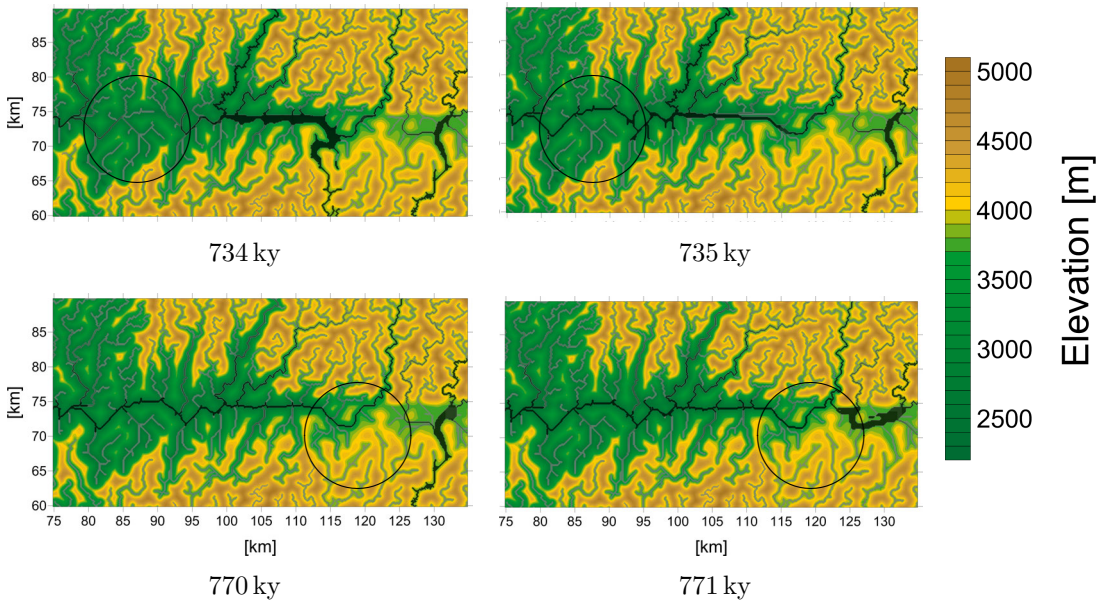

Figure 4.37: *Two river capturing events that happen in the model shown in Fig. 4.36. The figures enlarge the framed region. The four map extracts present the topography at 734 ky, 735 ky, 770 ky, and 771 ky. The main channel network is drawn in dark grey. Black circles mark the river capturings.*

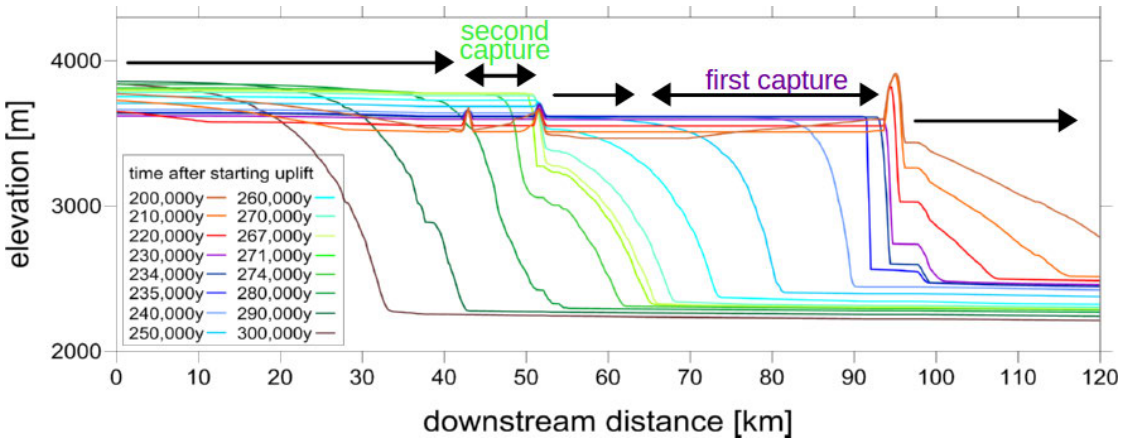

Figure 4.38: *Longitudinal profile's evolution of the cyan coloured channel at Fig. 4.36 from 0.7 My to 0.8 My. The black arrows indicate the water flow direction. Arrows with two heads symbolize a reversed flow direction after a capturing event.*

This section shows the importance of the *lateral incision* routine for modelling river capturing events. Beyond that, the models provide important suggestions about the probability of river capturing at dip-slip faults: While the angle between riverbed and fault and the uplift rate have direct influence on the capturing probability, the erodibility inside a fault influences the probability indirectly. It speeds up headward erosion of channels that are already trapped in a fault and in this way reduces the time between two capturings along the same fault. This indicates that an isolated capturing event may be unlikely. Several river capturing events along a fault are suggested to start from downstream, developing convex upstream migrating knickpoints.

The presented models agree with the idea that multiple capturing events along a fault happen in sequence as assumed for the Panj. The modelled longitudinal profiles show convex sections similar to the Panj's profile (compare to Fig. 4.21). However, the angle between the westward directed part of the Panj river and the northward directed part is about 90°. Sec. 4.2.5 indicates that very high uplift rates may be needed to induce a deflection of such an angle. The probability of modelled captures with lower deflection angle is much higher. Moreover, a fault in the northward flowing Panj is assumed to be a strike-slip fault rather than a dip-slip fault, according to the tectonic movements. As the uplift rate mainly affects the probability of capturings, such a fault would have small influence on the Panj's evolution. Hence, the suggestion that the development of the Panj river was induced by river capturing events is not supported by this study.

4.3 Coupling of DANSER and SLIM 3D

Research shows that tectonics influence surface evolution (e. g. Adams, 1980; Cook et al., 2014; Koppes and Montgomery, 2009; Bookhagen and Strecker, 2008). However, it is still controversial if in reverse some observed tectonic movements may be interpreted as a feedback to surface processes (e. g. Whipple, 2014; Wang et al., 2014). Meanwhile, numerical studies suggest that surface processes may control the tectonic evolution of the lithosphere (see Sec. 2.3.2). For intercontinental collision, this has been studied up to 2.5 dimensions (Burov and Toussaint, 2007).

However, the tectonic movement in the Pamir region is highly three dimensional (Sippl et al., 2013). The importance of 3D models for intercontinental collision (especially in the India-Asia collision zone) has been further underlined by recent numerical studies (Lechmann et al., 2014; Pusok and Kaus, 2015). This implies a need for a fully coupled 3D model of the India-Asia collision zone, including the Pamir region.

Sec. 3.3 introduces the coupling method between the presented surface evolution codes (SECs) and a lithospheric-scale (thermo-)mechanical code on a Lagrangian quadrilateral mesh. I make use of the described coupling method, the thermo-mechanical code SLIM 3D (Popov and Sobolev, 2008) and DANSER (described in Sec. 3.2) to model indenter tectonics, giving an impression how strong the influence of erosion to the evolution of the Pamir – Tien Shan region might be.

Sec. 4.3.1 introduces the setup of the model. Its parameters' calibration is outlined in Sec. 4.3.2. Different surface settings and their influence on the model are presented in Sec. 4.3.3. Finally, Sec. 4.3.4 shows the model's evolution in time steps of 5 My.

4.3.1 Setup

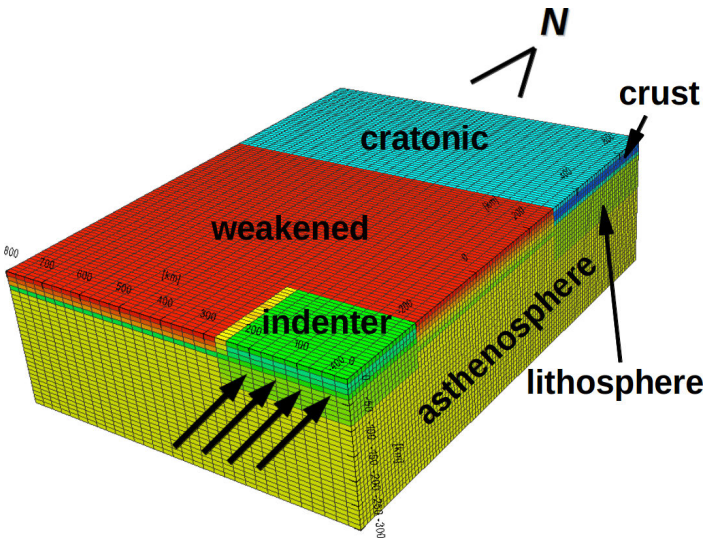

Figure 4.39: *Setup of the thermo-mechanical indenter model. Model of* $1100\,km \times 800\,km \times 300\,km$ *(N-S, E-W, vertical) with a resolution of* $110 \times 32 \times 30$ *nodes. The black arrows indicate that the green indenter at the southern model boundary moves to the north.*

The thermo-mechanical model (setting in Fig. 4.39) improves the model of Tympel (2014, Chap. 9.3). His model was developed in order to represent the western half of the India-Asia collision zone, assuming reflection symmetry and no material flux through the eastern model boundary. The tectonic time step is 10 ky and the evolution time 25 My. The 260 km wide, 200 km long and 120 km thick indenter at the south-eastern model boundary moves to the north with a velocity of 4 cm/y. This velocity linearly decreases to 0 cm/y within 40 km in westward direction and

within 30 km depth. The northern and western model boundaries allow no slip, the eastern boundary has free slip conditions and the southern boundary allows no slip in east-west direction, but free slip in vertical direction. The entire model moves northward with a velocity of 2 cm/y, inducing effective material flux through the model from north to south. This moving box allows to follow the area of interest, with reduced model size. The reader is referred to Tympel (2014) for further details about the thermo-mechanical setting.

Slim 3D includes a simple surface smoothing in every time step to reduce numerical instabilities at the free surface. As explained in Sec. 3.3.4, this smoothing is switched off. Instead, the DANSER-own *smoothing* routine is switched on.

The surface evolution model's cell size is $1\,km \times 1\,km$. The incision time step is $1\,ky$. Channel initiation is switched off, because the threshold for water discharge, from which fluvial incision starts, may not be higher than $1\,km^2$. Accordingly, hillslope diffusion performs in every cell and the diffused material is not removed in channel cells (compare to Sec. 3.2.5). Lateral incision is switched off as well, because it is not needed in order to model the rearrangements of the river network without channel initiation function. The eastern model boundary is closed for any water and sediment flux. All other boundaries are closed for diffusion and limited to a maximum incision rate of $10^{-4}\,mm/y$.

The immobile surface model exactly covers the thermo-mechanical model in east-west direction. In north-south direction, it starts at the thermo-mechanical model's starting point ($-400\,km$) and ends at $1000\,km$. This means the surface model overlaps the thermo-mechanical model at the southern boundary. At the northern boundary it overlaps until $15My$. From $15My$, erosion at the northern end of the thermo-mechanical model is neglected, because this area is almost flat.

4.3.2 Rough calibration

The surface model parameters' calibration is straightforward. Without channel initiation, the mass conservative diffusion is not able to transport sediments out of the model. Thus, the stream power coefficient is the only controlling parameter for outflowing material. The material outflow is equal to the average mass removal times the area. As the percentage of fluvial incised material is assumed to be negligible in comparison to hillslope processes, I calibrate the stream power coefficient with the aid of long-term erosion rates.

Stübner et al. (2013b) employ titanite, monazite, and zircon U/Th-Pb, mica Rb-Sr and 40Ar/39Ar, zircon and apatite fission track, and zircon (U-Th)/He ages to determine long-term erosion rates from about 18-15 Ma to 2 Ma. They compute hillslope erosion within the domes of 0.3 to 0.5 mm/y and 0.1 to 0.3 mm/y in the

horst separating the Shakhdara and Alichur domes and in the southeastern Pamir plateau. I use an average erosion rate of $0.3\,mm/y$ to estimate the sediment flux out of the Pamir. I compute models with varying stream power coefficient and the cumulated sediment outflow. The best fitting model has a stream power coefficient of $\kappa_{rb} = 1.4 \cdot 10^{-4}$.

The diffusivity controls the number of channels evolving at the topography. The number of parallel main channels can be counted at the Pamir DEM (Fig. 1.1). Visual validation of models with different diffusivities lead to $\kappa_{hs} = 5.0$.

Important for the model's reliability is that the quantity of filling material is slightly below that of the eroded material.

4.3.3 Influence of incision, filling and smoothing on orogen evolution

This section compares five different settings to illuminate the influence of riverbed incision, hillslope diffusion, filling of depressions, and technically required displacement smoothing on the model. The following model with filling but without fluvial incision may just be used for a qualitative study, because the amount of total filling material is 25 % smaller by including fluvial incision.

Fig. 4.40 highlights the effect on the topography. Without displacement smoothing the computation aborts due to numerical instabilities at the free surface of SLIM 3D. With low smoothing ($n_{smooth} = 2$), instabilities can still be observed at the northern and southern orogen's boundaries. A smoothing window size $n_{smooth} = 6$ flattens the displacements enough, while avoiding to destroy the uplifting relief. Hillslope diffusion further smoothes the evolving relief. Filling that may be interpreted as sedimentation lifts the southern basin by $1000\,m$. It helps to push the northern orogen front further north by depositing sediments in the basin in between. Furthermore, it lifts the southern part of the orogen. The orogen expands to the south and widens there. Additional riverbed incision increases the highest peak's elevation, while strongly incising the orogen's south-western part.

Fig. 4.41 reveals little influence of the described surface settings on the lithospheric structure. The filling routine slightly changes the bending of the southern plate by loading it with sediments.

The brittle surface strain (Fig. 4.42) indicates more than six faults sub-parallel to the orogens borders. Some brittle structures in orthogonal direction are visible as well. The figures emphasize the strong influence of the displacement smoothing and the filling on the brittle surface deformation. The displacement smoothing removes material from the regions of strongest uplift. It decreases the weight

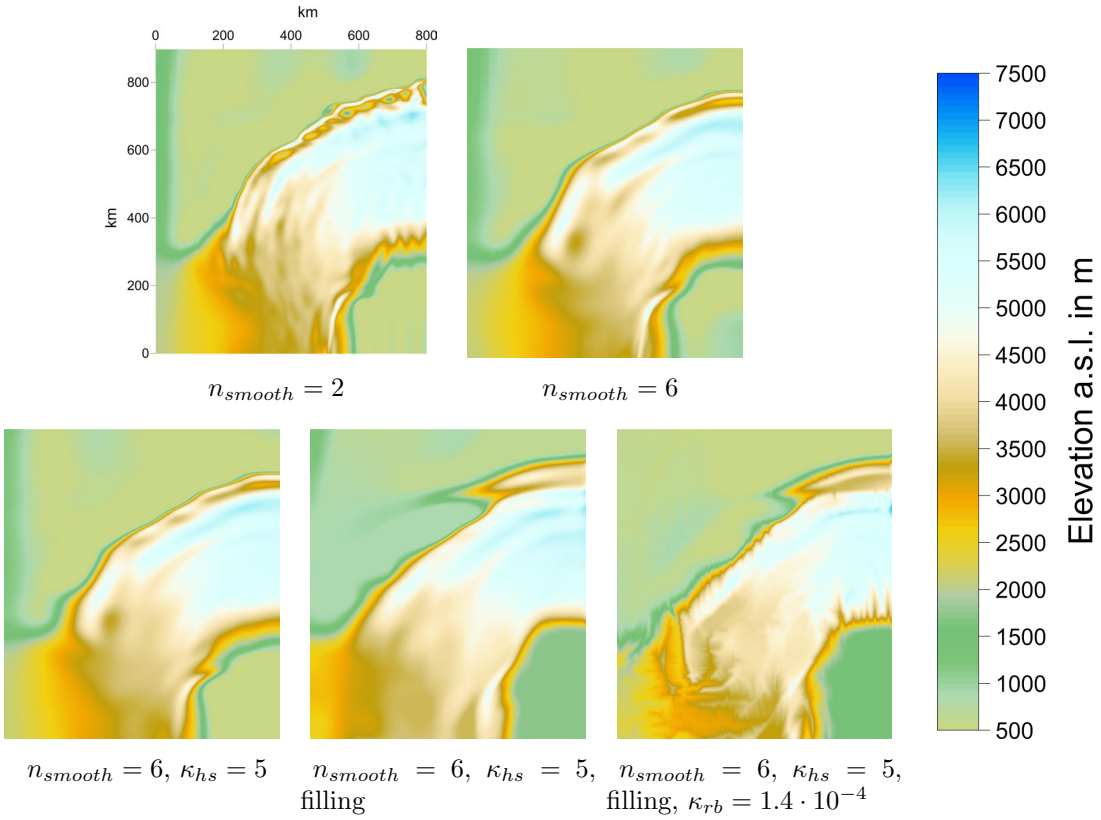

Figure 4.40: *Extract of five models' topographies at* $20\,My$. *Comparison with different settings. The left top model is smoothed with a window size* $n_{smooth} = 2$, *all other models are computed with* $n_{smooth} = 6$. *The left bottom model includes hillslope processes and the centred model adds filling. The lower model at the right involves additional riverbed incision.*

exactly where it works against surface movements. This is much more effective in order to amplify the brittle surface defomation than a normal surface smoothing such as hillslope diffusion. In contrast, filling reduces the brittle deformation as described above. As the figures illustrate, the modelled incision is not able to reduce significantly the filling's influence on the brittle deformation.

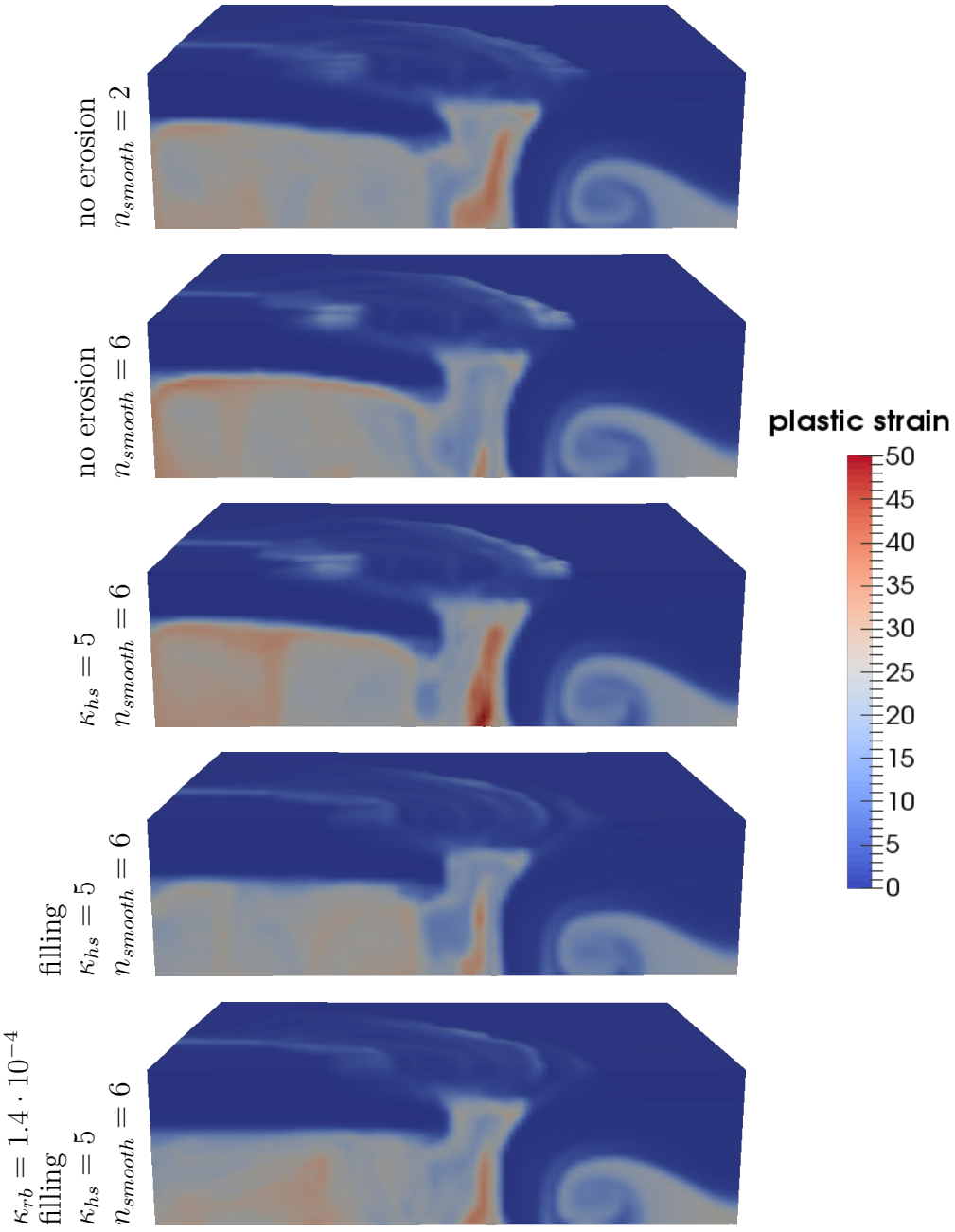

Figure 4.41: *Plastic strain at 20 My. View of the entire thermo-mechanical model from the east. Comparison with different settings. The top model is smoothed with a window size $n_{smooth} = 2$, all other models have a smoothing window size $n_{smooth} = 6$. The third model includes hillslope diffusion and the fourth model filling of depressions. The model at the bottom additionally involves riverbed incision.*

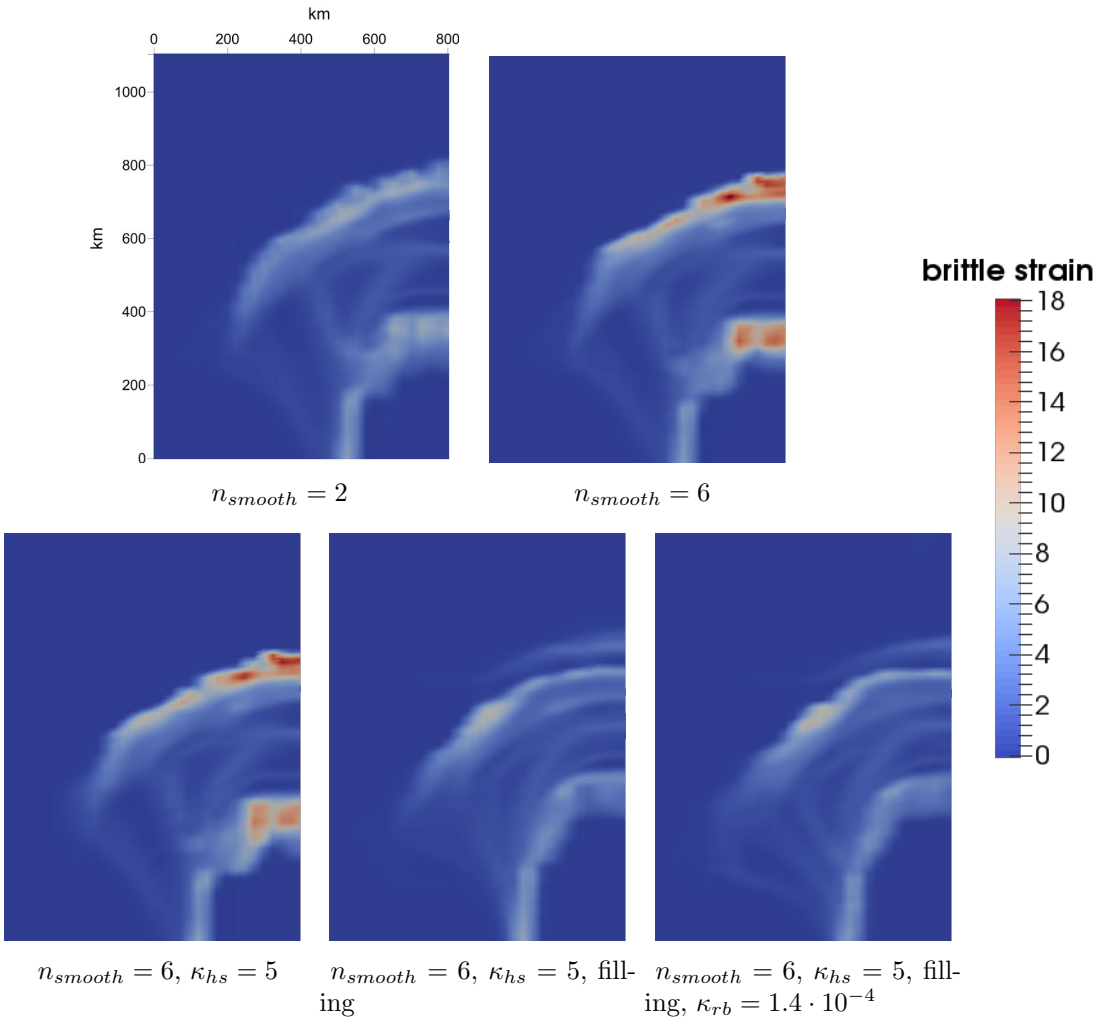

Figure 4.42: *Surface strain at* $20\,My$*. Comparison with different settings. The top left model is smoothed with a window size* $n_{smooth} = 2$*, all other models have a smoothing window size* $n_{smooth} = 6$*. The left bottom model includes hillslope diffusion and the centred one adds filling of depressions. The model at the bottom, right additionally involves riverbed incision.*

To summarise, the models indicate that sedimentation widens the basin in between the developing northern and southern orogens (formerly demonstrated e. g. by Fillon et al., 2013). Similar to the numerical 3D study of Thieulot et al. (2014), fluvial incision increases the elevation difference between hilltops and valleys that much that the absolute peak elevation is bigger than it would be without erosion. Their suggestion that an orogen narrows due to erosion, is partly confirmed by the presented models: While the most narrow part of the orogen further narrows because of surface processes, filling widens and extends the southern end. The reason for the contradicting results may be the neglected isostasy in their crustal model.

The models show minor influence of surface processes on the lithosphere's deformation. Filling on the southern plate slightly decreases the bending because of the added crustal load. Nevertheless, the modelled brittle strain is clearly lowered by this process.

4.3.4 Evolution of the river network

Sec. 4.2 explains the influence of a parallel dip-slip fault system to the development of river networks. This section uses the indenter model to get further insights to developing river networks under the influence of intracontinental collision.

Fig. 4.43 shows the model's evolution (see Sec. 4.3.3) with smoothing, hillslope diffusion, riverbed incision and sedimentation. In order to avoid straight rivers, the presented development includes the addition of white noise to the topography every $10\,ky$. This white noise simulates stochastic processes (e.g. landslides) that roughen the topography. It has to be emphasized once more that this model neglects channel initiation. A model with slightly higher resolution can include channel initiation and lateral incision. Thus, modelling of hillslope processes at the water divide will be enabled and may lead to different results.

The model may reflect the formation of the Pamir's south-westward oriented river network. It shows a reorganizing river network with little capturing events. The rivers get pushed northward within the forming orogen. Because of the northward moving indenter, they get directed to south-west. Within the model, capturings from north to south happen just at the northern orogen's border. More pronounced are captures within the orogen from west to east. The model do not show any north-south captures that build such a sudden turn as the Panj river shows.

It is worth mentioning, that the west-southward direction of many Pamir's rivers may directly result from the tectonic movement, not from capturing events along the faults, as expected. Even though the model shows some pronounced observations from within the Pamir orogen, it may not reflect the entire tectonic evolution.

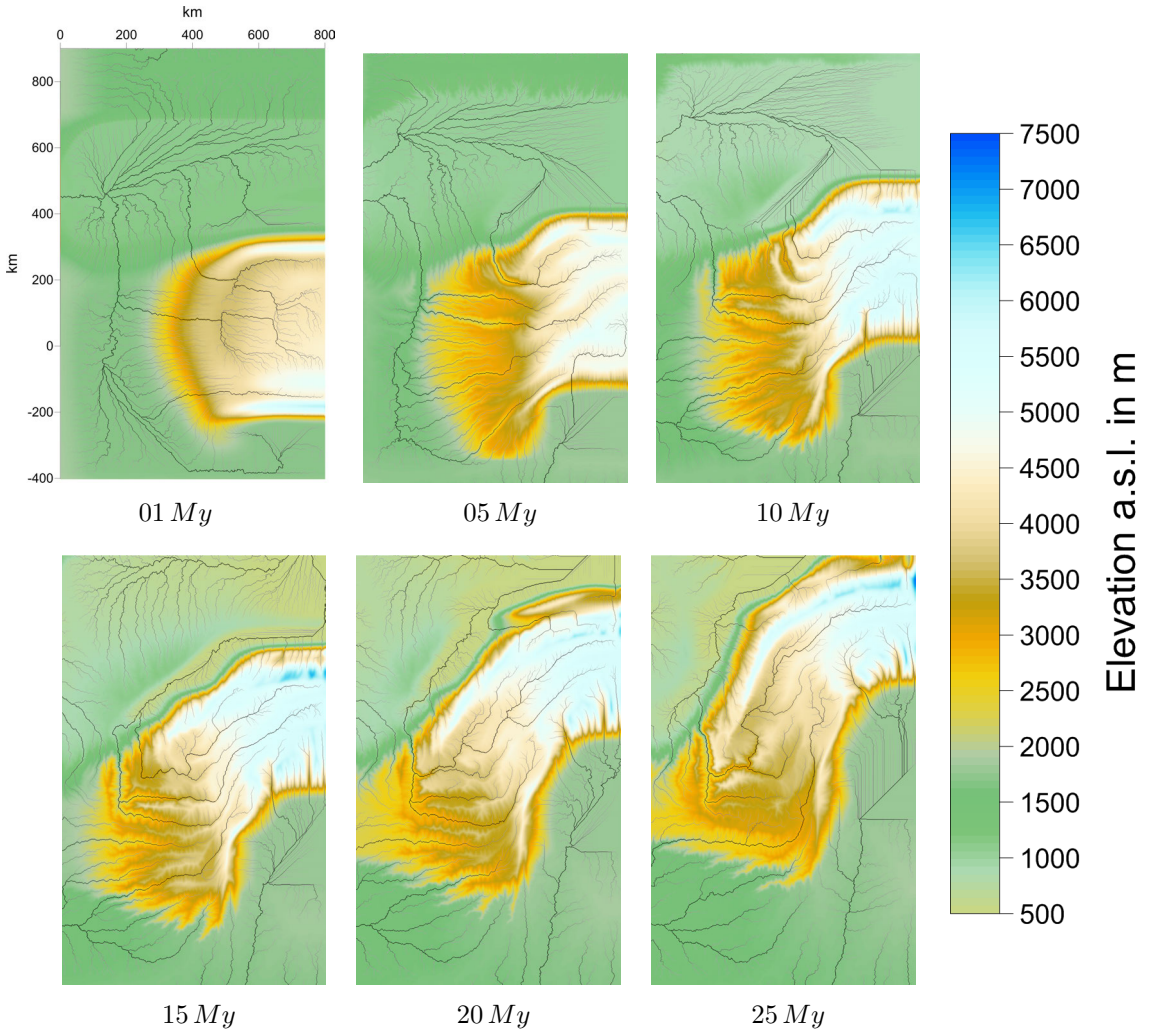

Figure 4.43: *Evolution of the model's topography. The river network is drawn in dark grey.*

Despite all the agreements between model and observations, the suggestion that the Panj's pathway is a result of river capturing events can not be confirmed.

These models underline the versatility of the developed code. Even though the model cannot reflect the Pamir – Tien-Shan's evolution, some features of intra-continental collision, which are similar to the observable ones in the study area,

are shown by the coupled 3D model: The orogen splits into two parts, a narrow mountain chain in the north (Tien-Shan) and a bigger orogen in the south (Pamir), which is penetrated by sub-parallel faults. A sediment basin (Alai Valley) forms in between the two orogens. Several mountain chains build in east-west direction, reaching more than $6000\,m$. The simplified model even suggests an explanation for the Pamir's south-westward directed river network.

In contrast, the surface does not show any southward directed river capturings that build such a strongly bending river as the Panj river is. One obvious capture within the model that has a deflection angle of 90° was induced from west to east. This result does not support the suggestion the Panj might have evolved recently because of river capturings (compare Sec. 4.2).

The models suggest that sedimentation widens the south-western part of the southern orogen and the basin in between the two developing orogens. They show minor influence of surface processes on the lithosphere's deformation. Filling on the southern plate slightly decreases the plate's bending because of the added crustal load. The model's brittle strain is clearly lowered by sedimentation.

Chapter 5

Summary and Outlook

5.1 Summary

This study presents the development of new 1D and 2D Surface Evolution Codes (SECs) and their coupling to lithospheric-scale (thermo-)mechanical models with surface nodes that are arranged as a quadrilateral, structured mesh. The coupling includes an interpolation between different spatial and temporal resolutions as well as a smoothing routine to avoid numerical instabilities at the (thermo-)mechanical free surface. The (thermo-)mechanical movements are transmitted to the SECs by (bi-)linearly interpolating the surface displacement vectors, considering vertical as well as horizontal movements. The evolved topography is handed back to the (thermo-)mechanical model by average-interpolation of the elevations. The SECs have the ability to take over locally varying material properties of the (thermo-) mechanical model and effective precipitation rates of a climate model.

Both surface evolution codes approach hillslope processes with the diffusion equation and fluvial incision with the stream power law. Moreover, they include sedimentation. The 1D computation of water discharges involves the assumption of rectangular drainage basins and Hack's Law. The water is assumed to leave the model in orthogonal direction at every local minimum, while sediments get deposited there. This guarantees mass conservation between every two water divides. The 2D code DANSER uses the D8 algorithm and a modified version of O'Callaghan and Mark's (1984) drainage accumulation routine for computation of the water discharge. A fast filling routine seals local depressions. It includes additionally nonlinear diffusion. The diffused material within a river is removed immediately to guarantee a fully supply-limited system.

Additionally, DANSER includes lateral incision, which is enabled by a new spreading algorithm that distributes the computed water discharge over the entire channel

width. This spreading is based on empirical equations. It allows to apply DANSER to high resolution Digital Elevation Models (DEMs) as initial topography, preserving the channel width. Furthermore, the routine enhances river capture modelling.

This study discusses a fine-tuned calibration of DANSER to geomorphological data and a DEM of the Pamir orogen: Noise and artefacts in DEMs build a major challenge in applying SECs to DEMs as initial topography. A DEM processing procedure can enhance the calibration result. Stream profile analysis of the DEM-extracted profiles allows multiple different interpretations of the river network's evolution. It does not lead to a unifying concavity index for the entire Pamir. However, lateral incision brings significant advances in order to run SECs on DEMs as initial topography. Nevertheless, hillslope processes present further calibration challenges that need to be solved in a more steady state-like landscape. Sparse data about the Pamir's erosion and sediment fluxes do not allow to validate or reject one of the hillslope diffusion models.

Two applications of different resolution and different time-scale are shown. The first application makes use of DANSER's lateral incision to model river capturing events in a dip-slip fault system. The models show significant dependence of the river network's evolution on the angle between faults and channels. The maximum uplift rate also has a strong effect on the resulting topography, whereas a fault's erodibility has minor influence on the probability of capturing events, but increases the capturing velocity within it.

The second application presents models of the thermo-mechanical code SLIM 3D, coupled to DANSER. The indenter models reflect significant observations from within the Pamir – Tien Shan region such as the formation of a big southern (Pamir) and a narrow northern orogen (Tien-Shan) that are separated by a sedimentary basin (Alai Valley). Similar to observations, the surface strain indicates multiple faults sub-parallel to the northern orogen's border. The models suggest minor influence of surface processes to the lithosphere's deformation, but strong effect on brittle surface deformations. The modelled sedimentation significantly changes the brittle surface strain. Instead, the model's influence of fluvial incision is rather small. However, the models indicate that fluvial incision increases the highest mountain's peaks and sedimentation widens the basin in between the orogens. The orogen's part in the south of the collision zone may be extended to the east, west and south.

Fuchs et al. (2013) suggest that the current pathway of the Panj river evolved because of several river capturing events. The here presented river capturing models cannot confirm their suggestion. Fault-bounded block rotation models indicate a low probability of river capturing events with large deflection angles as assumed for the Panj river. Beyond that, the model's uplift rate directly controls the number

of capturing rivers. The erodibility of the material inside of a fault is suggested to influence the capturing velocity of a already capturing stream but seem to have rather small influence if the stream gets captured. If the northward flowing Panj would flow along a fault, this fault would rather be a strike-slip fault than a dip-slip fault. Because the uplift rate mainly affects the probability of capturings, such a strike-slip fault may have small influence on the evolution of the river network. Beside that, the surface evolution of the indenter model reflects the structure of the observed river network. The indenter moves the eastern channels to north aligning them with the orogen's northern border. Nonetheless, the model show no river capturing from north to south that build such a strong bending river pathway.

5.2 Outlook

The coupling method of DANSER leaves the surface area fixed during the computation. For a fast moving (thermo-)mechanical model, the surface model has to be chosen very large in order to cover the entire surface of the (thermo-)mechanical model in every time step. To reduce the computation loops and the memory footprint, the surface model should adapt in every time step to the (thermo-) mechanical model's size. Such a method was implemented in the 1D SEC and can be adapted to DANSER. The movement of the regular, equidistant surface grid can be guaranteed by adapting the stored coordinates x_0 and y_0 of the first cell. Since the coordinates of the other cells are not stored, but defined as $x_k = x_0 + k \cdot \Delta x$ and $y_k = y_0 + k \cdot \Delta x$, this will induce a movement of the grid. The interpolation of the deformed surface grid back to the fixed grid (described in Sec. 3.3.2) may be substituted by the interpolation to the shifted grid. This does not reduce the computation's accuracy. If the (thermo)-mechanical model expanded or shortened, the memory adaptation for the surface grid could be easily enabled by using the predefined C++ class "vector".

A more complex possibility to speed up the computation of DANSER is to parallelise it. A parallelisation with CUDA or another programming language for graphics processing unit (GPU) is not recommended, because to my knowledge no GPU-parallelised (thermo-)mechanical codes exist. Furthermore, the parallelisation with CUDA should be adapted to the GPU architecture. Because the GPU's development is very fast, a CUDA-parallelized Code must be adapted to every machine's hardware. A better choice is the parallelisation with Open MP or MPI, depending on the desired efficiency and the available time to implement it. DANSER was created in order to parallelise the software subsequently. Thus, the flow direction's, the diffusion's, the incision's, and the lateral incision's computation is highly parallelisable. Only the accumulation of water discharge's and the

filling routine's parallelisation is challenging. The filling routine is the most time consuming algorithm. Thus, its parallelisation is most important. A parallelised form of the filling algorithm of Martz and de Jong (1988) might be more efficient than a parallelised version of the algorithm of Planchon and Darboux (2001).

Regions of a (thermo-)mechanical model with high displacement rate's gradients (strain, e. g. in faults) need to be well resolved for the coupling with a SEM. Self-adaptive mesh refinement in the (thermo-)mechanical code ensures a high resolution in those regions, but avoids huge computation times. Thus, a highly advanced coupled code should localize surface elements with high strain rate and refine the (thermo-)mechanical mesh in those elements.

Up to now, the sediment's material properties are neglected in the (thermo-) mechanics of the coupled model. Nodes that are changed by the SEC are elevated or lowered without adapting the material properties of the node or the markers nearby. This is a good approach for erosion and incision, but for deposition the sediment's material properties get changed to that of the material underneath. A more sophisticated solution is that the coupling method influences the (thermo-)mechanical node's height as well as a cloud of markers that is included in the (thermo-)mechanical model. In the volume, which evolves via the rise in the node's elevation, new markers with sediment properties are defined. If this led to too many markers within an element, these markers would be deleted within the next remeshing.

The model in Sec. 4.3.4 has a resolution of $1\,km$. Slightly higher resolution would allow to use channel initiation and lateral incision. Additionally, a more observation-like parameter calibration could be performed. The difference in the results of such a model and the presented model may give further conclusions about the process of river capturing.

In order to model the Pamir's development better, more reliable geomorphological data on different time scales are required. More detailed knowledge about the regions and periods of glacial influence could be used to apply a glacial model and a model for riverbed incision in turns. Better knowledge about the sediment transport behaviour of rivers could reveal that a combination of a transport- and supply-limited approach (e. g. Davy and Lague, 2009) strongly enhances the modelling of the Pamir orogen.

To study the probability of river capturing events in the Pamir, Sec. 4.2 presents models of capturings along dip-slip faults. As the dominant fault mechanism in the Pamir orogen is oblique-slip, a complete study should also contain the influence of strike-slip faults to a river networks' evolution.

The Karakul line splits the Pamir in two parts: The eastern part is higher than the western part, holds more glacial remnants and shows much less seismicity.

Although the western Pamir is influenced by the Westerlies (Fuchs et al., 2013), the monsoon-influenced climate eastward of Karakul is very dry (Owen et al., 2008). Moreover, Schoenbohm et al. (2014) observe an asymmetry in ELA in the Chinese Pamir that they interpret as the result of a climatic variability. The coupled model in Sec. 4.3 neglects this spatial climate variability. As observations show a high influence of precipitation rates on erosion (e. g. observed in the eastern Himalaya / in the Andes by Bookhagen and Strecker, 2012; Grujic et al., 2006), further studies should take into account the influence of different precipitation rates in the eastern and western part on the model's evolution.

Finally, DANSER and the related code developed for this study, improved and enhanced as sketched out here, could be used to model other oregons.

Appendix A

Description of further 2D tools

For DEM preparation and result analysis, I implement important tools. These tools are described in the following.

Reduce resolution

The tool *reduce_resolution* finds the lowest elevation of the DEM within a given radius around each cell of a new, coarser grid. It stores this value as elevation in the new grid, preserving the channel depth, but underestimating hilltops.

Smooth riverbed

The tool *smooth_riverbed* identifies a stream from a given starting point via flow directions. It filters outliers above the standard deviation in a moving window of a given number of cells along the stream profile. In addition, it corrects elevation values of the chosen river profile that are higher than the elevation of the water-providing cell. To guarantee a downward directed riverbed without any sinks or steps, these values are interpolated linearly in water flow direction. Afterwards, the tool smooths the transformed, monotonic decreasing profile over another number of cells. To avoid that the river changes its original flow direction, cells around the riverbed are elevated infinitesimal above the channel level.

Computation of surface evolution data for mapping

Saving data like elevation, incision and diffusion rates in all cells consumes a lot of time. Hence, a reduction of the number of saving processes speeds up the surface evolution algorithm. Therefore, I avoid saving erosion values, rather saving the

elevation data in selected time steps. All the other data has to be recalculated, if needed. This is of major importance for visualization.

The *mapping* tool computes and stores specific erosion data with the aid of the surface evolution routines (Sec. 3.2.2 to 3.2.6). For that purpose it evaluates the water flow direction and the topographic slope in that direction, the common water discharge and the spread discharge for lateral incision, as well as the incision and diffusion rates. The data are stored in the form of matrices that contain information for every cell of the cellular automaton grid. The tool provides these data as binary *grd*-files, created to read with Surfer 9 of Golden Software (Surfer, 2009).

Analysing tool for longitudinal river profiles

Based on the theory in Sec. 2.2.1, I developed a tool for *stream_profile_analysis* that also extracts erosion specific data along a channel.

The tool computes water flow directions, slopes from donor to receiver cell, common water discharges and spread water discharges, incision rates, diffusion rates and sediment discharges using the routines of DANSER (described in Sec. 3.2). For a given start cell, the cell coordinates, the elevation, the channel length and all cell dependent informations are extracted in flow direction. This gives the river track, the longitudinal river elevation profile and other useful data along the stream.

If possible, single cells that split two concave river profile parts are corrected. This means, that the elevation of these cells is set to the highest value that fulfils the concavity condition, a positive second derivative. The resulting first derivative is smoothed with a median filter over 50 cells. Afterwards, a mean filter smooths with the same window size. The smoothed derivatives serve for identification of the concave channel segments. Furthermore, the logarithms of slope and water discharge are computed for every cell within the river profile. These data are prepared for a log-log plot. Additionally, the tool evaluates the best fit straight line in every concave channel segment via least squares. The derivative of the best fit is according to stream profile analysis (Sec. 2.2.1) the required concavity index θ.

Finally, all data along the river profile, the borders of the concave channel segments, the best fit straight lines, and the concavity indices are stored for plotting. The tool provides all profiles along the river as Surfer 9 ascii *bln*-files. Sec. 4.1.5 shows the resulting river profiles and log-log plots for the main rivers in the Pamir orogen.

Time development of a river profile

The development of river profiles in time is essential to study the influence of the SEC on surfaces. The *river_profile_analysis* tool (Sec. A) extracts a river profile of a chosen time step. Since the river may change its bed, the distances might be variable in time. Hence, this tool might be not sufficient to compare a profile at different time steps.

The tool *comp_profiles* is built to study the development of river profiles in time and avoids inconsistent comparisons. It extracts the river trace along the initial topography. After surface evolution, it follows this trace. In a window around each cell along the trace, the lowest value defines the local elevation of the adapted river profile. The routine stores the profile as Surfer 9 ascii *bln*-file.

Appendix B

Nonlinear lateral incision

Some of the presented models include linear lateral incision. Jens Turowski suggested in a personal communication at 9-22-2014 to orient the incision radius and the lateral incision height on the nonlinear empirical equations for channel width w and depth d, firstly introduced in (Leopold and Maddock, 1953):

$$w = a \cdot Q^b$$

$$d = c \cdot Q^f$$

Leopold and Maddock evaluate empirical average exponents $b = 0.5$ and $f = 0.4$.

Fig. B.1 compares the same model with different nonlinear lateral incision parameters to a model with linear lateral incision. The figure shows that similar drainage network behaviour as for linear lateral incision can be achieved with adapted factors b and f for the suggested nonlinear lateral incision exponents. Thus, the numerical code does not profit from the nonlinearity. In contrast, two more variables have to be calibrated. Furthermore, the suggested values are not measured in the Pamir orogen, which suffers from sparse geomorphological data.

Moreover, it has to be mentioned that a numerical model cannot reflect the complex physical erosion mechanisms. This numerical code aims to reflect the results of erosion that we observe.

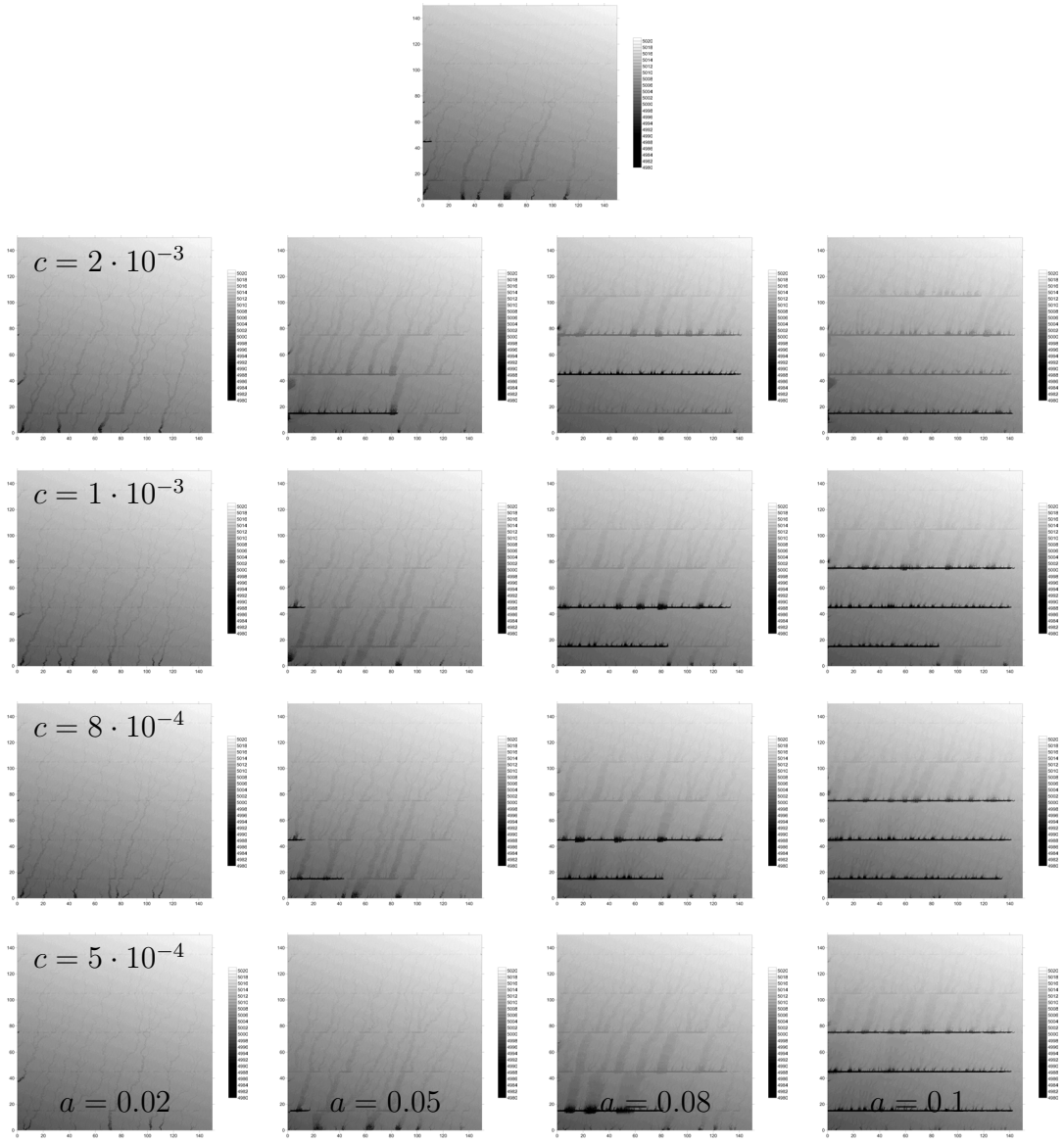

Figure B.1: *Inclined plane with five fault-bounded block rotations after* $4\,ky$ *of surface evolution. The angle between faults and riverbeds is* $70°$*. The incision parameter is set to* 0.005 *and the diffusion parameter to* 0.5*. The uplift reaches up to* $1\,mm/y$ *and the erodibility inside of the faults is increased by a factor of* 100*. The upper figure shows a model with linear lateral incision and lateral incision constants* $c_{\Delta h} = 10^{-6}$ *and* $c_{rad} = 10^{-4}$*, as chosen in Sec. 4.2. The models underneath include nonlinear lateral incision with exponents* $b = 0.5$ *and* $f = 0.4$*. The factors* a *and* c *increase from left to right and from bottom to top.*

List of Figures

Bibliography

Abramowski, U., Bergau, A., Seebach, D., Zech, R., Glaser, B., Sosin, P., Kubik, P. W., and Zech, W. (2006). Pleistocene glaciations of Central Asia: results from 10 Be surface exposure ages of erratic boulders from the Pamir (Tajikistan), and the Alay–Turkestan range (Kyrgyzstan). *Quaternary Science Reviews*, 25(9):1080–1096.

Adams, J. (1980). Contemporary uplift and erosion of the Southern Alps, New Zealand. *Geological Society of America Bulletin*, 91(1 Part II):1–114.

Babeyko, A. and Sobolev, S. (2008). High-resolution numerical modeling of stress distribution in visco-elasto-plastic subducting slabs. *Lithos*, 103:205–216.

Bagnold, R. A. (1966). An Approach to the Sediment Transport Problem From General Physics. *General Physics Geological Survey, Prof. paper*, 422-1:I5 pp.

Beaumont, C., Fullsack, P., and Hamilton, J. (1992). *Erosional control of active compressional orogens*. Springer.

Beaumont, C., Fullsack, P., and Hamilton, J. (1994). Styles of crustal deformation in compressional orogens caused by subduction of the underlying lithosphere. *Tectonophysics*, 232(1):119–132.

Begin, Z. B. (1988). Application of a diffusion-erosion model to alluvial channels which degrade due to base-level lowering. *Earth Surface Processes and Landforms*, 13(6):487–500.

Belousov, T. P. (1976). *Tectonic movements of Pamir during Pleistocene-Holocene and the seismicity*. Nauka, Moskau.

Bookhagen, B. and Strecker, M. R. (2008). Orographic barriers, high-resolution TRMM rainfall, and relief variations along the eastern Andes. *Geophysical Research Letters*, 35(6):L06403.

Bookhagen, B. and Strecker, M. R. (2012). Spatiotemporal trends in erosion rates across a pronounced rainfall gradient: Examples from the southern Central Andes. *Earth and Planetary Science Letters*, 327:97–110.

Braun, J. and Sambridge, M. (1997). Modelling landscape evolution on geological time scales: a new method based on irregular spatial discretization. *Basin Research*, 9:27–52.

Braun, J. and Shaw, R. (2001). A thin-plate model of Palaeozoic deformation of the Australian lithosphere: implications for understanding the dynamics of intracratonic deformation. *Geological Society, London, Special Publications*, 184(1):165–193.

Braun, J., Thieulot, C., Fullsack, P., DeKool, M., Beaumont, C., and Huismans, R. (2008). DOUAR: A new three-dimensional creeping flow numerical model for the solution of geological problems. *Physics of the Earth and Planetary Interiors*, 171(1):76–91.

Braun, J. and Yamato, P. (2010). Structural evolution of a three-dimensional, finite-width crustal wedge. *Tectonophysics*, 484(1):181–192.

Burov, E. and Toussaint, G. (2007). Surface processes and tectonics: forcing of continental subduction and deep processes. *Global and Planetary Change*, 58(1):141–164.

Burov, E. B., Watts, A. B., et al. (2006). The long-term strength of continental lithosphere: "jelly sandwich" or "crème brûlée"? *GSA today*, 16(1).

Chase, C. G. (1992). Fluvial landsculpting and the fractal dimension of topography. *Geomorphology*, 5(1):39–57.

Collignon, M., Kaus, B., May, D., and Fernandez, N. (2014). Influences of surface processes on fold growth during 3-D detachment folding. *Geochemistry, Geophysics, Geosystems*, 15(8):3281–3303.

Cook, K. L., Turowski, J., and Hovius, N. (2014). River gorge eradication by downstream sweep erosion. *Nature Geosciences*, 7:682–686.

Coulthard, T. and Van De Wiel, M. J. (2006). The Cellular Automaton Evolutionary Slope And River Model (CAESAR).

Dabrowski, M., Krotkiewski, M., and Schmid, D. (2008). MILAMIN: MATLAB-based finite element method solver for large problems. *Geochemistry, Geophysics, Geosystems*, 9(4):Q04030.

Davy, P. and Lague, D. (2009). Fluvial erosion/transport equation of landscape evolution models revisited. *Journal of Geophysical Research: Earth Surface (2003–2012)*, 114(F3).

DeLong, S. B., Pelletier, J. D., and Arnold, L. (2007). Bedrock landscape development modeling: Calibration using field study, geochronology, and digital elevation model analysis. *Geological Society of America Bulletin*, 119(1-2):157–173.

Densmore, A. L., Ellis, M. A., and Anderson, R. S. (1998). Landsliding and the evolution of normal-fault-bounded mountains. *Journal of geophysical research: solid earth.*, 103(B7):15203–15219.

Egholm, D. L., Knudsen, M. F., Clark, C. D., and Lesemann, J. E. (2011). Modeling the flow of glaciers in steep terrains: The integrated second-order shallow ice approximation (iSOSIA). *Journal of Geophysical Research: Earth Surface (2003-2012)*, 116(F2):F02012.

Fairfield, J. and Leymarie, P. (1991). Drainage Networks From Grid Digital Elevation Models. *Water Resources Research*, 27(5):709–717.

Fillon, C., Huismans, R. S., and van der Beek, P. (2013). Syntectonic sedimentation effects on the growth of fold-and-thrust belts. *Geology*, 41(1):83–86.

Finnegan, N. J., Roe, G., Mongomery, D. M., and Hallet, B. (2005). Controls on the channel width of river: Implications for modeling fluvial incision of bedrock. *Geological Society of America*, 33(3):229–232.

Freeman, T. G. (1991). Calculating catchment area with divergent flow based on a regular grid. *Computers & Geosciences*, 17(3):413–422.

Fuchs, M., Gloaguen, R., Merchel, S., Pohl, E., Sulaymonova, V., Andermann, C., and Rugel, G. (2015). Millennial erosion rates across the Pamir based on 10 Be concentrations in fluvial sediments: dominance of topographic over climatic factors. *Earth Surface Dynamics Discussions*, 3(1):83–128.

Fuchs, M. C., Gloaguen, R., Krbetschek, M., and Szulc, A. (2014). Rates of river incision across the main tectonic units of the Pamir identified using optically stimulated luminescence dating of fluvial terraces. *Geomorphology*, 216:79–92.

Fuchs, M. C., Gloaguen, R., and Pohl, E. (2013). Tectonic and climatic forcing on the Panj river system during the Quaternary. *Int J Earth Sci (Geol Rundsch)*, 102:1985–2003.

Fuller, C., Willett, S., Fisher, D., and Lu, C. (2006). A thermomechanical wedge model of Taiwan constrained by fission-track thermochronometry. *Tectonophysics*, 425:1–24.

Fullsack, P. (1995). An arbitrary Lagrangian-Eulerian formulation for creeping flows and its application in tectonic models. *Geophysical Journal International*, 120(1):1–23.

Galy, A. and France-Lanord, C. (2001). Higher erosion rates in the Himalaya: Geochemical constraints on riverine fluxes. *Geology*, 29(1):23–26.

Garcia-Castellanos, D. (2002). Interplay between lithospheric flexure and river transport in foreland basins. *Basin Research*, 14(2):89–104.

Gerya, T. V. and Yuen, D. A. (2003). Characteristics-based marker-in-cell method with conservative finite-differences schemes for modeling geological flows with strongly variable transport properties. *Physics of the Earth and Planetary Interiors*, 140(4):293–318.

Gilbert, G. K. (1877). *Report on the Geology of the Henry Mountains*. US Government Printing Office.

Gloaguen, R., Fuchs, M., Pohl, E., Sulaymonova, V., and Andreani, L. (2014). Climatic vs tectonic forcing: the case of Pamir. In *EGU General Assembly Conference Abstracts*, volume 16 of *EGU General Assembly Conference Abstracts*, page 11045.

Godard, V., Burbank, D., Bourlès, D., Bookhagen, B., Braucher, R., and Fisher, G. (2012). Impact of glacial erosion on 10Be concentrations in fluvial sediments of the Marsyandi catchment, central Nepal. *Journal of Geophysical Research: Earth Surface (2003–2012)*, 117(F3).

Godard, V., Lavé, J., and Cattin, R. (2006). Numerical modelling of erosion processes in the Himalayas of Nepal: effects of spatial variations of rock strength and precipitation. *Geological Society, London, Special Publications*, 253(1):341–358.

Goren, L., Willett, S. D., Herman, F., and Braun, J. (2014). Coupled numerical–analytical approach to landscape evolution modeling. *Earth Surface Processes and Landforms*, 39(4):522–545.

Grotzinger, J., Jordan, T., Press, F., and Siever, R. (2007). *Understanding Earth 5th Ed.* Susan Finnemore Brennan.

Grujic, D., Coutand, I., Bookhagen, B., Bonnet, S., Blythe, A., and Duncan, C. (2006). Climatic forcing of erosion, landscape, and tectonics in the Bhutan Himalayas. *Geology*, 34(10):801–804.

GTOPO30 (1996). *Global Digital Elevation Model (GTOPO30)*. U.S. Geological Survey, EROS Data Center Distributed Active Archive Center (EDC DAAC), Redlands, California, USA.

Hack, J. T. (1957). Studies of Longitudinal Stream Profiles in Virginia and Maryland. Technical report, Geological Survey Professional Paper.

Hansen, D. L. (2003). A meshless formulation for geodynamic modeling. *Journal of Geophysical Research: Solid Earth (1978-2012)*, 108(B11).

Howard, A. D. (1994). A detachment-limited model of drainage basin evolution. *Water resources research*, 30(7):2261–2285.

Howard, A. D. and Kerby, G. (1983). Channel changes in badlands. *Geological Society of America Bulletin*, 94:739–752.

Huismans, R. S. (2014). Linking lithosphere deformation and sedimentary basin formation over multiple scales. In *EGU General Assembly Conference Abstracts*, volume 16 of *EGU General Assembly Conference Abstracts*, page 14200.

Hurst, M. D., Mudd, S. M., Walcott, R., Attal, M., and Yoo, K. (2012). Using hilltop curvature to derive the spatial distribution of erosion rates. *Journal of Geophysical Research: Earth Surface (2003–2012)*, 117(F2):F02017.

Jenson, S. and Domingue, J. (1988). Extracting topographic structure from digital elevation data for geographic information system analysis. *Photogrammetric engineering and remote sensing*, 54(11):1593–1600.

Kaus, B. J. P., Mühlhaus, H., and May, D. A. (2010). A stabilization algorithm for geodynamic numerical simulations with a free surface. *Physics of the Earth and Planetary Interiors*, 181(1):12–20.

Kirby, E. and Whipple, K. (2001). Quantifying differential rock-uplift rates via stream profile analysis. *Geology*, 29(5):415–418.

Kirkby, M. J. (1971). Hillslope process-response models based on the continuity equation. *Inst. Br. Geogr. Spec. Publ*, 3:15–30.

Kooi, H. and Beaumont, C. (1996). Large-scale geomorphology: Classical concepts reconciled and integrated with contemporary ideas via a surface processes model. *Journal of Geophysical Research*, 101(B2):3361–3386.

Koons, P. O. (1989). The topographic evolution of collisional mountain belts; a numerical look at the Southern Alps, New Zealand. *American journal of Science*, 289(9):1041–1069.

Koppes, M. N. and Montgomery, D. R. (2009). The relative efficacy of fluvial and glacial erosion over modern to orogenic timescales. *Nature Geoscience*, 2(9):644–647.

Kurfess, D. and Heidbach, O. (2009). CASQUS: A new simulation tool for coupled 3D finite element modeling of tectonic and surface processes based on ABAQUS and CASCADE. *Computers & Geosciences*, 35:1959–1967.

Lague, D. (2014). The stream power river incision model: evidence, theory and beyond. *Earth Surf. Process. Landforms*, 39:38–61.

Lague, D., Hovius, N., and Davy, P. (2005). Discharge, discharge variability, and the bedrock channel profile. *Journal of Geophysical Research: Earth Surface*, 110(F4).

Larsen, I. J. and Montgomery, D. R. (2012). Landslide erosion coupled to tectonics and river incision. *Nature Geoscience*, 5(7):468–473.

Lechmann, S. M., Schmalholz, S. M., Hetenyi, G., May, D. A., and Kaus, B. J. P. (2014). Quantifying the impact of mechanical layering and underthrusting on the dynamics of the modern India-Asia collisional system with 3-D numerical models. *Journal of Geophysical Research: Solid Earth*, 119(1):616–644.

Leopold, L. B. and Maddock, T. (1953). The hydraulic geometry of stream channels and some physiographic implications. *Geological Survey professional paper*, 252(252):1–57.

Lin, W.-T., Chou, W.-C., Lin, C.-Y., Huang, P.-H., and Tsai, J.-S. (2008). WinBasin: Using improved algorithms and the GIS technique for automated watershed modelling analysis from digital elevation models. *International Journal of Geographical Information Science*, 22(1):47–69.

Martz, L. W. and de Jong, E. (1988). CATCH: A Fortran Program For Measuring Catchment Area From Digital Elevation Models. *Computers & Geosciences*, 14(5):627–640.

Martz, L. W. and Garbrecht, J. (1992). Numerical definition of drainage network and subcatchment areas from digital elevation models. *Computers and Geosciences*, 18(6):747–761.

Molnar, P. and England, P. (1990). Late Cenozoic uplift of mountain ranges and global climate change: chicken or egg? *Nature*, 346:29–34.

Montgomery, D. R. and Dietrich, W. E. (1994). A physically based model for the topographic control on shallow landsliding. *Water Resources Research*, 30(4):1153–1171.

Montgomery, D. R. and Foufoula-Georgiou, E. (1993). Channel network source representation using digital elevation models. *Water Resources Research*, 29(12):3925–3934.

Moresi, L., Dufour, F., and Mühlhaus, H.-B. (2003). A Lagrangian integration point finite element method for large deformation modeling of viscoelastic geomaterials. *Journal of Computational Physics*, 184(2):476–497.

Norton, K. P., Abbühl, L. M., and Schlunegger, F. (2010). Glacial conditioning as an erosional driving force in the Central Alps. *Geology*, 38(7):655–658.

O'Callaghan, J. F. and Mark, D. M. (1984). The extraction of drainage networks from digital elevation data. *Computer vision, graphics, and image processing*, 28(3):323–344.

Owen, L. A., Caffee, M. W., Finkel, R. C., and Seong, Y. B. (2008). Quaternary glaciation of the Himalayan-Tibetan orogen. *Journal of Quaternary Science*, 23(6-7):513–531.

Pedersen, V. K., Huismans, R. S., Herman, F., and Egholm, D. L. (2014). Controls of initial topography on temporal and spatial patterns of glacial erosion. *Geomorphology*, 223:96–116.

Pelletier, J. D. (2004). Persistent drainage migration in a numerical landscape evolution model. *Geophysical Research Letters*, 31(L20501).

Pelletier, J. D. (2007). Numerical modeling of the Cenozoic geomorphic evolution of the southern Sierra Nevada, California. *Earth and Planetary Science Letters*, 259(1):85–96.

Pelletier, J. D. (2010). Numerical modeling of the late Cenozoic geomorphic evolution of Grand Canyon, Arizona. *Geological Society of America Bulletin*, 122(3-4):595–608.

Planchon, O. and Darboux, F. (2001). A fast, simple and versatile algorithm to fill the depressions of digital elevation models. *Catena*, 46:159–176.

Pohl, E. and Gloaguen, R. (2012). Suspended sediment flux characteristics in the central Pamirs. In Abbasi, A. and Giesen, N., editors, *EGU General Assembly Conference Abstracts*, volume 14 of *EGU General Assembly Conference Abstracts*, page 10528.

Pohl, E., Gloaguen, R., Andermann, C., and Schön, A. (2013). Suspended sediment load, climate and relief in the central Pamirs. In *EGU General Assembly Conference Abstracts*, volume 15 of *EGU General Assembly Conference Abstracts*, page 12979.

Pohl, E., Gloaguen, R., and Andermann, C. i. p. (2015a). Suspended sediment transport characteristics in the Pamirs, Tajikistan.

Pohl, E., Knoche, M., Gloaguen, R., Andermann, C., and Krause, P. (2015b). Sensitivity analysis and implications for surface processes from a hydrological modelling approach in the Gunt catchment, high Pamir Mountains. *Earth Surface Dynamics*, pages 333–362.

Poliakov, A. N. B., Cundall, P. A., Podladchikov, Y. Y., and Lyakhovsky, V. A. (1993). An explicit inertial method for the simulation of viscoelastic flow: an evaluation of elastic effects on diapiric flow in two-and three-layers models. In *Flow and Creep in the Solar System: observations, modeling and Theory*, pages 175–195. Springer.

Popov, A. and Kaus, B. (2013). LaMEM (Lithosphere and Mantle Evolution Model): advancing a staggered-grid finite difference version of the code. In *EGU General Assembly Conference Abstracts*, volume 15, page 7761.

Popov, A. and Sobolev, S. (2008). SLIM3D: A tool for three-dimensional thermomechanical modeling of lithospheric deformation with elasto-visco-plastic rheology. *Physics of the Earth and Planetary Interiors*, 171(1):55–75.

Pratson, L. F. and Coakley, B. J. (1996). A model for the headward erosion of submarine canyons induced by downslope-eroding sediment flows. *Geological Society of America Bulletin*, 108(2):225–234.

Pusok, A. E. and Kaus, B. J. P. (2015). Development of topography in 3-D continental-collision models. *Geochemistry, Geophysics, Geosystems*, 16:1378–1400.

Roberts, G. G. and White, N. (2010). Estimating uplift rate histories from river profiles using African examples. *Journal of Geophysical Research*, 115(B02406).

Rodriguez, E., Morris, C. S., and Belz, J. E. (2006). A global assessment of the SRTM performance. *Photogrammetric Engineering & Remote Sensing*, 72(3):249–260.

Roering, J. J., Kirchner, J. W., and Dietrich, W. E. (1999). Evidence for nonlinear, diffusive sediment transport on hillslopes and implications for landscape morphology. *Water Resources Research*, 35(3):853–870.

Roering, J. J., Kirchner, J. W., and Dietrich, W. E. (2001). Hillslope evolution by nonlinear, slope-dependent transport: Steady state morphology and equilibrium adjustment timescales. *Journal of Geophysical Research: Solid Earth (1978–2012)*, 106(B8):16499–16513.

Schmeling, H., Babeyko, A. Y., Enns, A., Faccenna, C., Funiciello, F., Gerya, T., Golabek, G. J., Grigull, S., Kaus, B. J. P., Morra, G., et al. (2008). A benchmark comparison of spontaneous subduction models–towards a free surface. *Physics of the Earth and Planetary Interiors*, 171(1):198–223.

Schoenbohm, L. M., Chen, J., Stutz, J., Sobel, E. R., Thiede, R. C., Kirby, B., and Strecker, M. R. (2014). Glacial morphology in the Chinese Pamir: Connections among climate, erosion, topography, lithology and exhumation. *Geomorphology*, 221:1–17.

Schuster, R. L. and Alford, D. (2004). Usoi Landslide Dam and Lake Sarez, Pamir Mountains, Tajikistan. *Environmental & Engineering Geoscience*, 10(2):151–168.

Seidl, M. A. and Dietrich, W. E. (1992). The problem of channel erosion into bedrock. *Functional geomorphology*, 23:101–124.

Simpson, G. and Schlunegger, F. (2003). Topographic evolution and morphology of surfaces evolving in response to coupled fluvial and hillslope sediment transport. *Journal of Geophysical Research: Solid Earth (1978–2012)*, 108(B6):ETG 7–1 – 7–16.

Sinclair, H. D., Coakley, B. J., Allen, P. A., and Watts, A. B. (1991). Simulation of foreland basin stratigraphy using a diffusion model of mountain belt uplift and erosion: an example from the central Alps, Switzerland. *Tectonics*, 10(3):599–620.

Sippl, C., Schurr, B., Yuan, X., Mechie, J., Schneider, F., Gadoev, M., Orunbaev, S., Oimahmadov, I., Haberland, C., Abdybachaev, U., et al. (2013). Geometry of the Pamir-Hindu Kush intermediate-depth earthquake zone from local seismic data. *Journal of Geophysical Research: Solid Earth*, 118(4):1438–1457.

Sklar, L. S. and Dietrich, W. E. (2001). Sediment and rock strength controls on river incision into bedrock. *Geology*, 29(12):1087–1090.

Snyder, N. P., Whipple, K. X., Tucker, G. E., and Merritts, D. J. (2000). Landscape response to tectonic forcing: Digital elevation model analysis of stream profiles in the Mendocino triple junction region, northern California. *Geological Society of America Bulletin*, 112(8):1250–1263.

Stephenson, R. and Lambeck, K. (1985). Erosion-isostatic rebound models for uplift: an application to south-eastern Australia. *Geophysical Journal International*, 82(1):31–55.

Stock, J. D. and Montgomery, D. R. (1999). Geologic constraints on bedrock river incision using the stream power law. *Journal of Geophysical Research: Solid Earth (1978–2012)*, 104(B3):4983–4993.

Stübner, K., Ratschbacher, L., Rutte, D., Stanek, K., Minaev, V., Wiesinger, M., and Gloaguen, R. (2013a). The giant Shakhdara migmatitic gneiss dome, Pamir, India-Asia collision zone: 1. Geometry and kinematics. *Tectonics*, 32(4):948–979.

Stübner, K., Ratschbacher, L., Weise, C., Chow, J., Hofmann, J., Khan, J., Rutte, D., Sperner, B., Pfänder, J. A., Hacker, B. R., et al. (2013b). The giant Shakhdara migmatitic gneiss dome, Pamir, India-Asia collision zone: 2. Timing of dome formation. *Tectonics*, 32(5):1404–1431.

Suppe, J. (1981). Mechanics of mountain building and metamorphism in Taiwan. *Memoir of the geological socienty of China*, (4):67–89.

Surfer (2009). *Surfer Getting Started Guide: Contouring and 3D Surface Mapping for Scientists and Engineers*. Golden Software, Inc., 809 14th Street, Golden, Colorado 80401-1866, U.S.A.

Tachikawa, T., Hato, M., Kaku, M., and Iwasaki, A. (2011). CHARACTERISTICS OF ASTER GDEM VERSION 2. *IEEE*, pages 3657–3660.

Tarboton, D. G. (1997). A new method for the determination of flow directions and upslope areas in grid digital elevation models. *Water resources research*, 33(2):309–319.

Thieulot, C., Steer, P., and Huismans, R. S. (2014). Three-dimensional numerical simulations of crustal systems undergoing orogeny and subjected to surface processes. *Geochemistry, Geophysics, Geosystems*, 15(12):4936–4957.

Tucker, G. E. (2010). CHILD Users Guide for version R9. 4.1. *Cooperative Institute for Research in Environmental Sciences (CIRES) and Department of Geological Sciences, University of Colorado, Boulder, USA*.

Tucker, G. E. and Bras, R. L. (1998). Hillslope processes, drainage density, and landscape morphology. *Water Resources Research*, 34(10):2751–2764.

Tucker, G. E. and Bras, R. L. (2000). A stochastic approach to modeling the role of rainfall variability in drainage basin evolution. *Water Resources Research*, 36(7):1953–1964.

Turcotte, D. L. and Schubert, G. (2014). *Geodynamics*. Cambridge University Press.

Tympel, J. G. (2014). *Numerical modeling of the Cenozoic Pamir-Tien Shan orogeny*. PhD thesis, University of Potsdam.

van der Beek, P. and Braun, J. (1998). Numerical modelling of landscape evolution on geological time-scales: a parameter analysis and comparison with the south-eastern highlands of Australia. *Basin Research*, 10:49–68.

Wang, P., Scherler, D., Liu-Zeng, J., Mey, J., Avouac, J.-P., Zhang, Y., and Shi, D. (2014). Tectonic control of Yarlung Tsangpo Gorge revealed by a buried canyon in Southern Tibet. *Science*, 346(6212):978–981.

Whipple, K. X. (2014). Can erosion drive tectonics? *Science*, 346(6212):918–919.

Whipple, K. X. and Tucker, G. E. (1999). Dynamics of the stream-power river incision model: Implications for height limits of mountain ranges, landscape response timescales, and research needs. *Journal of Geophysical Research: Solid Earth (1978–2012)*, 104(B8):17661–17674.

Willett, S. D. (1999). Orogeny and orography: The effects of erosion on a structure of mountain belts. *Journal of Geophysical Research*, 104(B12):28957–28981.

Willett, S. D. (2010). Erosion on a line. *Tectonophysics*, 484(1):168–180.

Willgoose, G. R. (1989). *A physical based channel network and catchment evolution model*. PhD thesis, Massachusetts Institute of Technology.

Willgoose, G. R., Bras, R. L., and Rodriguez-Iturbe, I. (1991). A coupled channel network growth and hillslope evolution model: 1. Theory. *Water Resources Research*, 27(7):1671–1684.

Yang, R., Willett, S. D., and Goren, L. (2015). In situ low-relief landscape formation as a result of river network disruption. *Nature*, 520(7548):526–529.

Acknowledgements

This work would not have been possible without the help and support of a lot of different people.

First of all, I thank Andrey Babeyko, my kind supervisor and member of the Geodynamic Modelling section at GFZ Potsdam. The door to his office was always open for me to come and ask any question. I am grateful for the opportunity to join so many conferences.

Richard Gloaguen and his team at TU Freiberg gave me precious knowledge about the Pamir orogen: Richard provided me his impressive knowledge in Geomorphology and many other areas. Spending endless hours on the phone, he converted me into a geophysicist. Without his constant encouragement, this study would never have been completed. He allowed me to visit the Pamir orogen and the powerful Panj river, the most impressive journey in my whole live. Richard Gloaguen, Adam Szulc, Margret Fuchs and the members of the Tajik University guided me through a magnificent landscape and a foreign culture.

Lothar Ratschbacher and Konstanze Stübner patiently shared and explained their observations in the Pamir. Lothar: Your geological map is still attached to my office wall, providing information about the Pamirs fault system. Matthias Schlett at TU Freiberg and Uwe Lemgo at GFZ Potsdam provided support running and finishing seemingly endless cluster computations.

Niels Hovious provided valuable input in long discussions about modelling surface processes. Bodo Bookhagen posed some important questions guiding me – virtually – through my final steps in the Pamir orogen's understanding. Javier Quinteros gave many hints that improved my code. Eric Pohl explained the Pamir's sediment transport. Paul Sass, Felix Schneider, Jens Tympel and Christian Sippl shared the burden of beeing a TIPAGE Ph. D. student. Oliver Ritter pushed me to my first talk in English – in front of 50 people.

The University of Potsdam taught me how wonderful Geology is. Manfred Strecker and Frank Krüger introduced me to Geology and Geophysics with their vivid classes. Michael Weber, head of Geophysical Deep Sounding Section, agreed to

supervise my thesis. Ritske Huismans and Boris Kaus agreed to be official examiners of my thesis, and Bodo Bookhagen, Niels Hovius and Manfred Strecker to be part of the committee.

Juliane Dannberg, Margret C. Fuchs, Elvira Mulyukova, Rene Gassmöller and Michael Krax provided innumerable ideas on how to improve my thesis. My roommates Anthony Osei Tutu, Marius Walter and Kenji Chan encouraged me. I enjoyed and appreciated the endless discussions about science with everyone of section 2.5 at GFZ Potsdam.

Thanks to all of you!

Finally, I would like to thank my entire family and dear friends for encouraging me in hard times. Thousand kisses to my beloved boyfriend, you gave me everything I needed to finish this work!

Erklärung

Hiermit erkläre ich an Eides Statt, dass die vorliegende Dissertation ohne unzulässige Hilfe Dritter und ohne Benutzung anderer als der angegebenen Literatur angefertigt wurde. Die Stellen der Arbeit, die anderen Werken wörtlich oder inhaltlich entnommen sind, wurden durch Quellenangaben kenntlich gemacht. Diese Arbeit hat in gleicher oder ähnlicher Form noch keiner Prüfungsbehörde vorgelegen.

Potsdam, den 02.09.2015